

CARMA Memorandum Series #60

CARMA Summer School 2012

Melvyn Wright, Marc Pound, Dick Plambeck, John Carpenter, Nikolaus Volgenau, Doug Friedel, Carmen Rodriguez Gonzalez, Erin Grand, Che-Yu Chen, Dyas Utomo, Mai Truong, Isaac Shivvers, Dominique Segura-Cox, Yiran Wang, Ashley Lindley, Aaron Juarez, Xing Lu, Chihomi Hara, Maria Jose Maureira, Matthew Rickert, Kyle Westfall, Jorge Gonzalez, Pedro Salas

August 15, 2012

ABSTRACT

The 6th CARMA Summer School was held at the observatory on Cedar Flat 2012 June 17-23 with 17 students from Berkeley, Caltech, Illinois, Maryland, U. Chicago, U. Alabama in Huntsville, Vanderbilt-Fisk, Tokyo U., Harvard, Northwestern, Kapteyn Instituut, and Pontificia Universidad Catolica de Chile. During the school, students formed small teams and designed and obtained their own observations, in consultation with the instructors. Using both science subarrays as well as CARMA-23, students observed star-forming regions, YSOs, a protostellar magnetic field, an AGB star, nearby galaxies, a high- z galaxy, and galaxy clusters. At the end of the week, the students gave short presentations on their results. In this memo we collect together some of the results from the student projects.

1. Introduction

The 6th CARMA Summer School was held at the observatory on Cedar Flat 2012 June 17-23 with 17 students from Berkeley, Caltech, Illinois, Maryland, U. Chicago, U. Alabama in Huntsville, Vanderbilt-Fisk, Tokyo U., Harvard, Northwestern, Kapteyn Instituut, and Pontificia Universidad Catolica de Chile. As in previous years, the school had the use of the telescope for the week. The array was in the compact D-configuration. During the school the students had their own observing projects which they worked on during the week as well as attending lectures and demonstrations. Each of the student projects had 5-6 hours of telescope time and the students controlled the telescope for their own projects. The students took the observations, reduced and analyzed the data, and presented the results.

On the first day the students learned how to select suitable observing projects for the CARMA telescope. The introductory lectures covered the characteristics of the telescope, instrumentation, and observing techniques which taught the students to:

- select suitable astronomical sources for observing.
- select the observing frequency, spectral lines to be observed.
- evaluate angular resolution, velocity resolution and sensitivity needed.
- select the correlator setup and calibrations needed.
- prepare an observing script to define the observing procedure at the telescope.
- make the observations

During the rest of the week, the lectures and demonstrations covered the theory and techniques used for millimeter wavelength aperture synthesis and for the CARMA array, and more detailed lectures on the hardware and software. As they worked on their projects the students learned how to:

- schedule the telescope effectively.
- calibrate the data.
- make images.
- identify and fix problems that set off the alarm.
- analyze and present the results.

On Friday the students made 10-15 minute presentations and we discussed the results. In all, a very satisfying week seeing all the enthusiasm and so many exciting projects from initial planning and observations, to analysis and results.

2. The CARMA Telescope

The CARMA telescope is an aperture synthesis array, typically operating as two independent subarrays of 15 and 8 antennas, respectively. In the CARMA-15 subarray, there are two receiver bands, 3 mm and 1 mm, and the spectral line correlator. A basic aperture synthesis observation makes an image the size of the primary beam ($\lambda/D \sim 1'$ at 100 GHz; $0.5'$ at 230 GHz) with a resolution corresponding to the maximum separations of the antennas. During the Summer School, CARMA-15 was in the D configuration, with an angular resolution $\sim 6''$ at 100 GHz, and $\sim 3''$ at 230 GHz. The CARMA-8 subarray of eight 3.5m antennas was in the SH configuration for continuum-only projects at 30 GHz (primary beam $\sim 11'$; resolution $\sim 2'$) and 90 GHz (primary beam $\sim 3.6'$; resolution $\sim 40''$). The CARMA-8 correlator produces 7 GHz of continuum data. All antennas can be combined into a single 23-element array, CARMA-23, with 4 GHz of correlator bandwidth. One student project made use of this mode.

It's best to observe a strong enough source that one can make an image during the school, rather than a detection project, then the effects of different imaging techniques can be explored. The most convenient source size is one which is smaller than the size of the primary beam when only one pointing is needed. Larger sources can be imaged by time-sharing the pointing of the antennas (mosaicing), at the cost of lowered sensitivity.

The sensitivity is determined by the system noise (receivers plus atmosphere), the bandwidth (or velocity resolution), and the observing time. The atmosphere is usually not so good for 1 mm observations in the summer (although a few 1 mm projects were selected this year), for sources which are at low declinations that must be observed through more of the atmosphere, so select a bright source which is high in the sky and can be observed at 3 mm or 1 cm is preferred. Not all the projects that the students wanted to do did not satisfy these these conditions, so a final list of projects from those proposed was selected on the first day of the school. Students grouped themselves into small teams to work on the selected projects.

2.1. Logistics

Because this is a hands-on school, all lectures and demonstrations were held in the control building and at the telescopes at Cedar Flat. Mel, Marc, Dick, Doug, and several of the students stayed in the "Ferguson" group campground, about 1.5 miles from the control room, and near the antenna pads for the A-configuration. Those who camped avoided the hassle of driving up and down the mountain each day and had a wonderful opportunity to fall asleep under a star-filled sky each night.

The other students stayed in the dorm and cottage at OVRO. Delicious breakfasts, lunches, and dinners were provided at the observatory, prepared by Terry Sepsey and Cecil Patrick. Mary Daniel adroitly handled all the accommodations, making sure every one had a place to rest their weary heads at the end of the long days. We organized a hike to Second Lake and beyond on Saturday June 23rd; 23 people went on the hike to Second Lake, and 8 continued on to higher elevations.

3. L1157: Mapping the Bipolar Outflow and Continuum Polarization

Aaron Juarez, Che-Yu Shen, Isaac Shivvers

3.1. Introduction & Motivation

We observed the ^{12}CO and ^{13}CO components of the bipolar outflow in L1157 as well as all four Stokes polarization parameters of the central continuum emission. L1157 is a protostar found in Cepheus (IRAS 20386+6751) (Looney et al. 2007), located at a distance between 250 pc and 440 pc (Lefloch et al. 2010). Thanks to astronomical surveys on low-mass young stellar objects, we empirically classify L1157 as a Class 0 protostar; it is enshrouded by a circumstellar envelope and has a highly collimated bipolar outflow with an opening angle of 35° (Arce & Sargent 2006). It is important to note that the material surrounding L1157 is not a circumstellar disk, as the envelope does not display Keplerian rotation (Chiang et al. 2010). L1157 has been studied extensively by others, but the magnetic field of the outflow is, as yet, only partially understood. We use our polarimetric observations to infer the projected orientation of the magnetic field and our results agree well with previous CARMA studies. Our results show an hour-glass shaped magnetic field coincident with the central source, oriented along the outflow direction. See Figures 1 and 2.

3.2. Observations & Data Reduction

We observed L1157 with CARMA-15 in the D array configuration, with the correlators operating at 1 mm in FULL-POL mode. We observed both ^{12}CO (2-1) and ^{13}CO (2-1) spectral lines in a 31 MHz window (USB and LSB, respectively), leaving us with 6 windows for 500 MHz continuum observations which we placed contiguously on either side of the spectral line windows avoiding other major transition lines. We observed the source for 3.0 hours during a 5.0 hour track on June 19th, 2012, PST. The weather during our run was very good, with opacity τ_{225} hovering between 0.20 and 0.25, and phase RMS pathlength between 100 and 250 μm .

We used 3C84 as a bandpass calibrator, Neptune as a flux calibrator, and 1927+739 as a phase calibrator. Our observing run went well, with no serious complications, and we found that we did not need to flag any of our data. We followed data reduction scripts written by John Carpenter, Dick Plambeck, and Chat Hull. We used the *CARMA 2012* distribution of *MIRIAD* to reduce our data, including two non-standard techniques needed to properly calibrate the full polarization observations: the new *MIRIAD* task *XYAUTO* to determine the phase difference accumulated along the signal path between the RR and LL polarizations, and the task *GPCAL* to fit for the leakages of each antenna (determining the cross-coupling between R and L receivers). We used *MOSMEM* and *CLEAN* to build maps of the extended spectral-line emission and the centralized continuum emission, respectively. Finally, we used the observed Stokes vectors to calculate the projected magnetic field lines, assuming the polarization vectors trace the electric field lines and are orthogonal to the magnetic field lines.

3.3. Analysis

Figures 1 and 2 reveal the bipolar outflow in $^{12}\text{CO}(2-1)$ and $^{13}\text{CO}(2-1)$, which agrees with previous observations. Note that the outflow in ^{13}CO is significantly less extended than in ^{12}CO . In agreement with Arce & Sargent (2006), this implies that the high-density, low-velocity gas observable in ^{13}CO has been entrained by the high-velocity outflow observable in ^{12}CO . We also detected a clear polarization signal in the continuum near the protostar, and we overlay the direction of the projected magnetic field on the maps below.

We want to point out that, in addition to the hourglass-shape magnetic field parallel to the outflow direction, we also detected a highly twisted region of the magnetic field (almost perpendicular to the main direction) located $\sim 5''$ away from the protostar. This scale roughly agrees with the flattened dust envelope detected by Looney et al. (2007), which has a slow rotational motion (Chiang et al. 2010). We therefore conclude that the twisted magnetic field is a feature of an axisymmetrically-collapsed and rotating envelope.

We also detected some blue-shifted material in the northern part of the outflow. This means that the outflow is almost parallel to the plane of sky, with a small part of the northern outflow aimed towards us. Note that the same behavior is detected in both ^{12}CO and ^{13}CO channels. Assuming a cone opening angle of $\sim 35^\circ$ (Looney et al. 2007), this implies that the outflow is within $\sim 10^\circ$ of the plane of the sky.

3.4. A 3D Visualizer in Python

During the course of our data reduction we built a 3D visualizer for CARMA datasets in Python using the FITS file format (created with the *MIRIAD* command *FITS*) and the Python package MayaVi2. Using this, we can easily display data cubes as 3D contour surfaces in an easy-to-manipulate and highly customizable interface. Figure 3 shows a snapshot of the outflow of L1157, as created by this visualizer. Feel free to contact Isaac¹ if you'd like a copy or if you'd like to learn more.

¹ishivvers@berkeley.edu

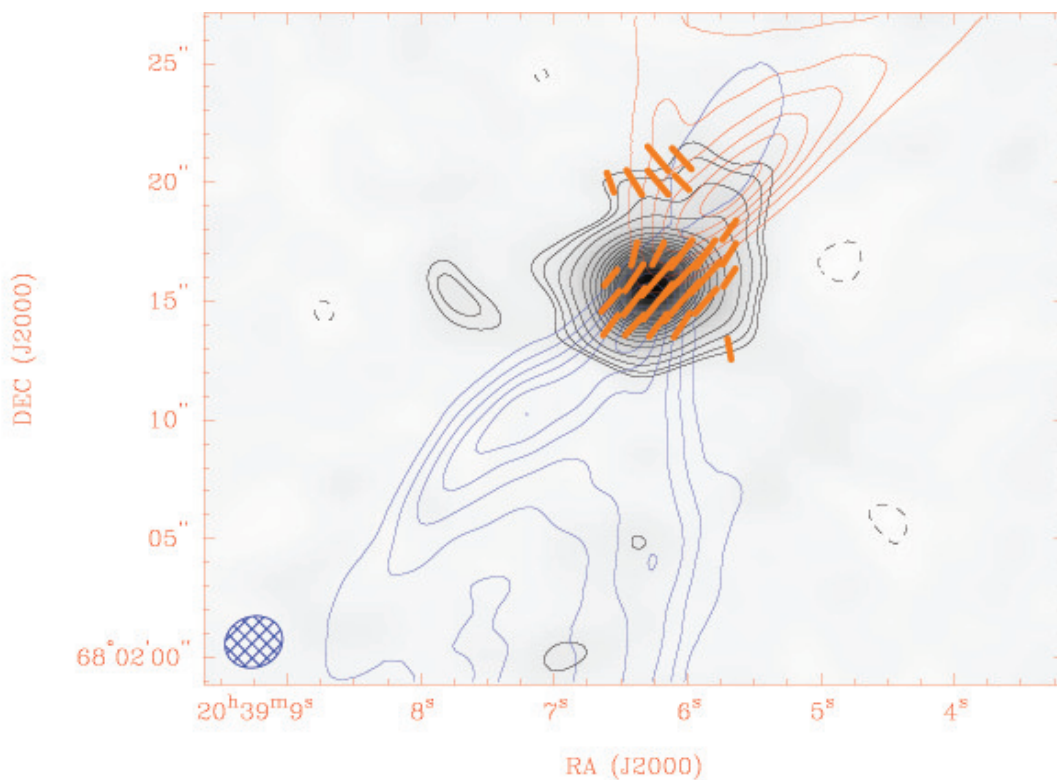


Fig. 1.— CARMA observations of L1157. The red/blue contours correspond to redshifted/blueshifted ¹²CO outflow, respectively, while the black contours and the grey map in the background show the continuum intensity. The orange lines indicate the direction of the magnetic field, projected on the sky.

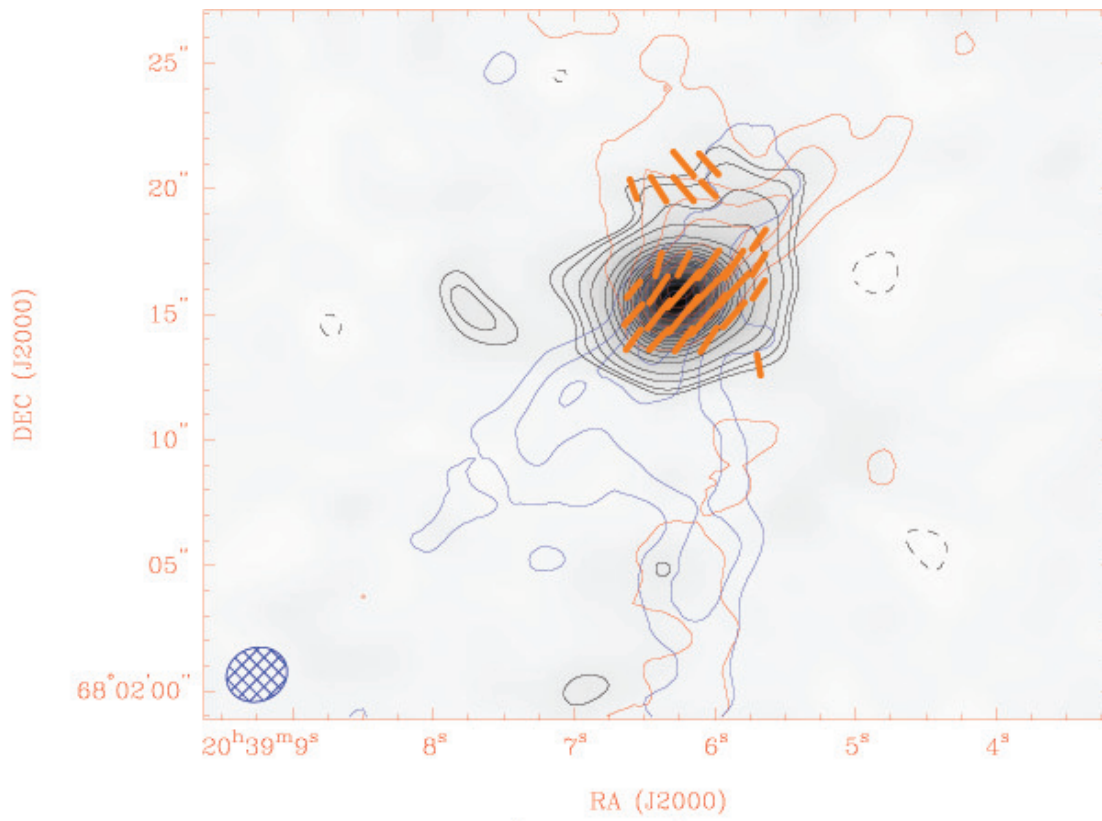


Fig. 2.— Same as Fig. 1, for the $^{13}\text{CO}(2-1)$ transition.

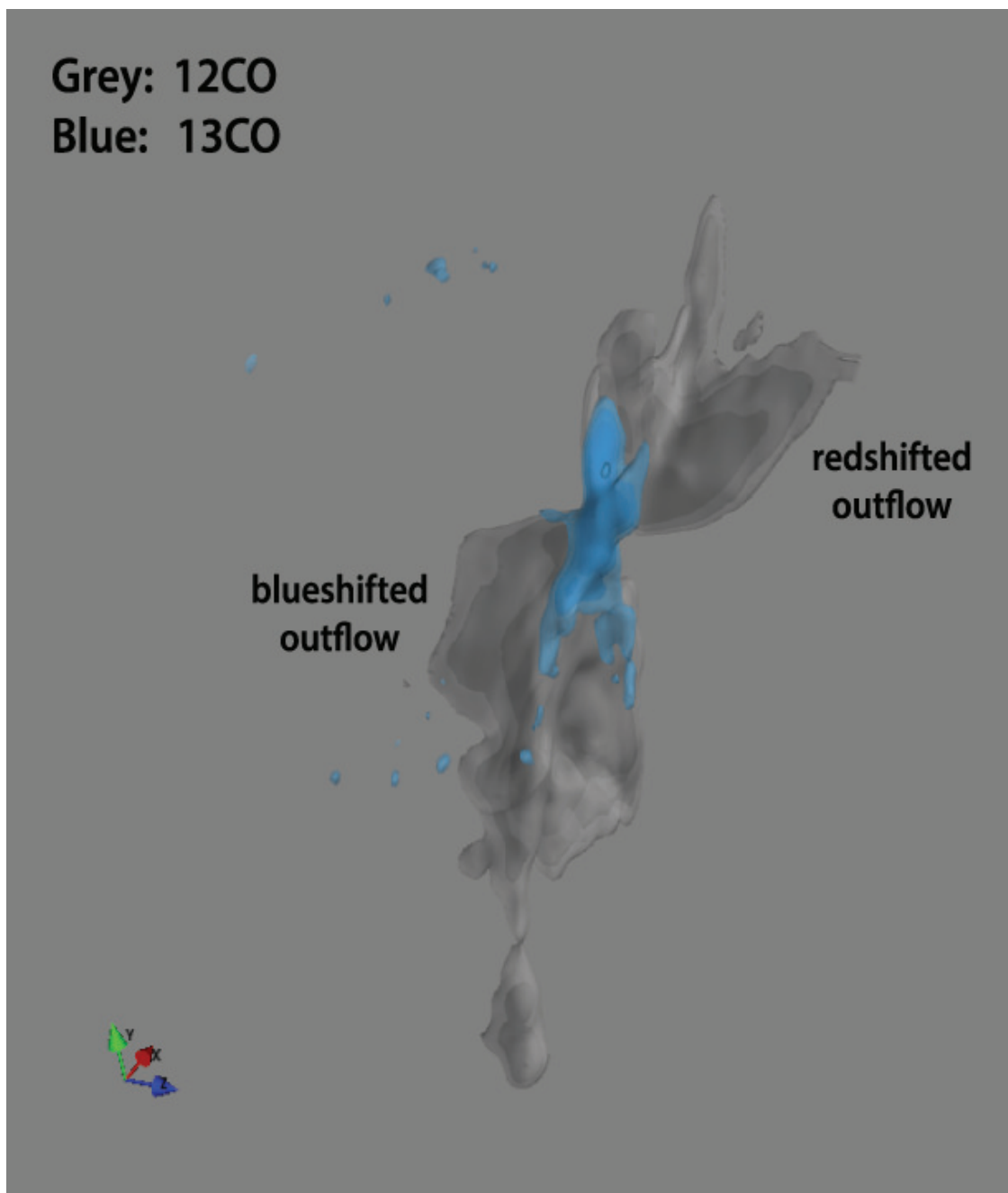


Fig. 3.— 3D contours of the L1157 bipolar outflow. ^{12}CO is in grey, and ^{13}CO in blue. The Z axis shows velocity relative to LSR, and the X,Y axes show RA and DEC, respectively. Be aware that this does not show the true shape of the outflow, of course, as the velocity dimension does not map to any spatial dimension.

4. CARMA observation of massive star forming region IRAS 19035+0641 Xing Lu (CfA)

4.1. Introduction

Massive star formation in our galaxy is still not fully understood, for reasons such as they are usually far away ($\gtrsim 1$ kpc), have a short time-scale of evolution ($\lesssim 10^4$ yrs), and are often imbedded in dense gas and dust where they are born, all of which make them difficult to observe directly in optical bands. But with millimeter, especially mm interferometric observations we are able to penetrate the annoying medium and see the innermost region of these massive gas bumps. With more observations we could detail our model of massive star formation and perhaps reveal this mytery one day.

Our target, IRAS 19035+0641, is a typical massive star forming region. Based on the MAMBO 1.2 mm continuum its mass is estimated as several hundred solar masses (Beuther et al. 2002), within an area of $\sim 1' \times 1'$, which corresponds to 0.66 pc across at a kinematic distance of 2.2 kpc. Note that the formula used in their paper to calculate mass has been correted in their erratum (Beuther et al. 2005). It is also lucky for us that its kinematic distance ambiguity is resolved, as in Sridharan et al. (2002).

We retrieve the infrared data from SPITZER archive and find maser detections in literature. There is a significant infrared point source in all four IRAC bands in this field, as shown in Figure 4 (we have put the 3 mm continuum contours for analysis below), and it coincides with water, Class II methanol and hydroxyl masers well. Among them the Class II methanol maser is a reliable massive star forming hallmark. Therefore, we are confident that there is active star formation happening.

With CARMA 3 mm band in D configuration, we have spatial resolution of about 6 arcsec, corresponding to 0.06 pc in IRAS 19035+0641. We expect to resolve substructures such as separated dust continuum cores, and use spectral lines like $^{12}\text{CO}(1-0)$ to show possible outflows.

4.2. Observation

The observation was done during the night of June 18th and morning of June 19th in single pointing mode, with 15 antennas in CARMA array. The coordinates of pointing is ($\alpha=19:06:01.5$, $\delta=06:46:35.7$), and velocity is set at 32.4 km/s. We use quasar 1830+063 as gain calibrator, which is close to our target. The bandpass and flux calibrators are BL Lac and Neptune, respectively. We use two narrow bands of 31 MHz to include $^{12}\text{CO}(1-0)$ and $^{13}\text{CO}(1-0)$ lines, and the rest are wide bands of 500 MHz for continuum. The rest frequency is 115.271 GHz. The entire track lasts for 3.52 hours and 2.5 hours are on source. The system temperature is quite stable at around 200 K during the track. The weather is also good, with total opacity equals 0.33. Since the data quality is good, we did not do flagging and made images directly from uv data.

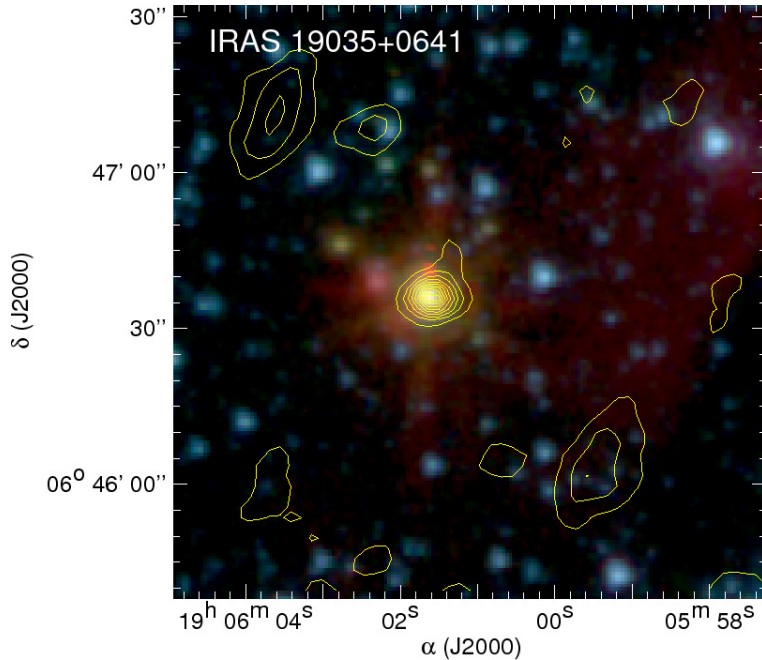


Fig. 4.— The IRAC bands 3.6, 4.5 and 8.0 μm are shown in blue, green and red colors. The 3mm continuum contours starts from 10% of peak intensity and increase in step of 10%.

4.3. Results

4.3.1. Spectral lines

The channel maps of both CO species are shown in Figure 5 and Figure 6. The ^{12}CO clearly shows a systematic motion, moving from southeast to northwest through channels, while ^{13}CO is more localized and concentrated. We also present the renzogram of ^{12}CO , in Figure 7, which is more obviously showing the blue- and red-shifted componets.

As we have found evidence of outflows in ^{12}CO spectra, we also want to compare it with ^{13}CO , which is optically thin and tracing denser gas. We select two square areas on either side of the continuum peak and get the averaged spectra. The result is shown in Figure 8. The ^{13}CO is at the same velocity in these two regions, which is consistent with the fact that it traces dense gas thus is not sensitive to outflows. On the other hand, ^{12}CO spectra show two components in these area, while the ‘dips’ between them lie at approximately the velocity of ^{13}CO ’s peak. These spectra resemble what is called ‘blue asymmetry’ profile (cf. Smith et al. (2012)), which indicates infalling motions of an optically thick gas sphere. However we should be careful before moving to the conclusion that we also see infalls here. First, although ^{12}CO is often optically thick, it stays in outward gases such as envelope most of time, and can be depleted near the center. Therefore the spectra profile we see might be due to real ^{12}CO distribution, instead of any systematic infalls. Another possibility is that the ‘dips’ are self-absorptions actually, by some cold gas near the center,

IRAS 19035+0641 $^{12}\text{CO}(1-0)$

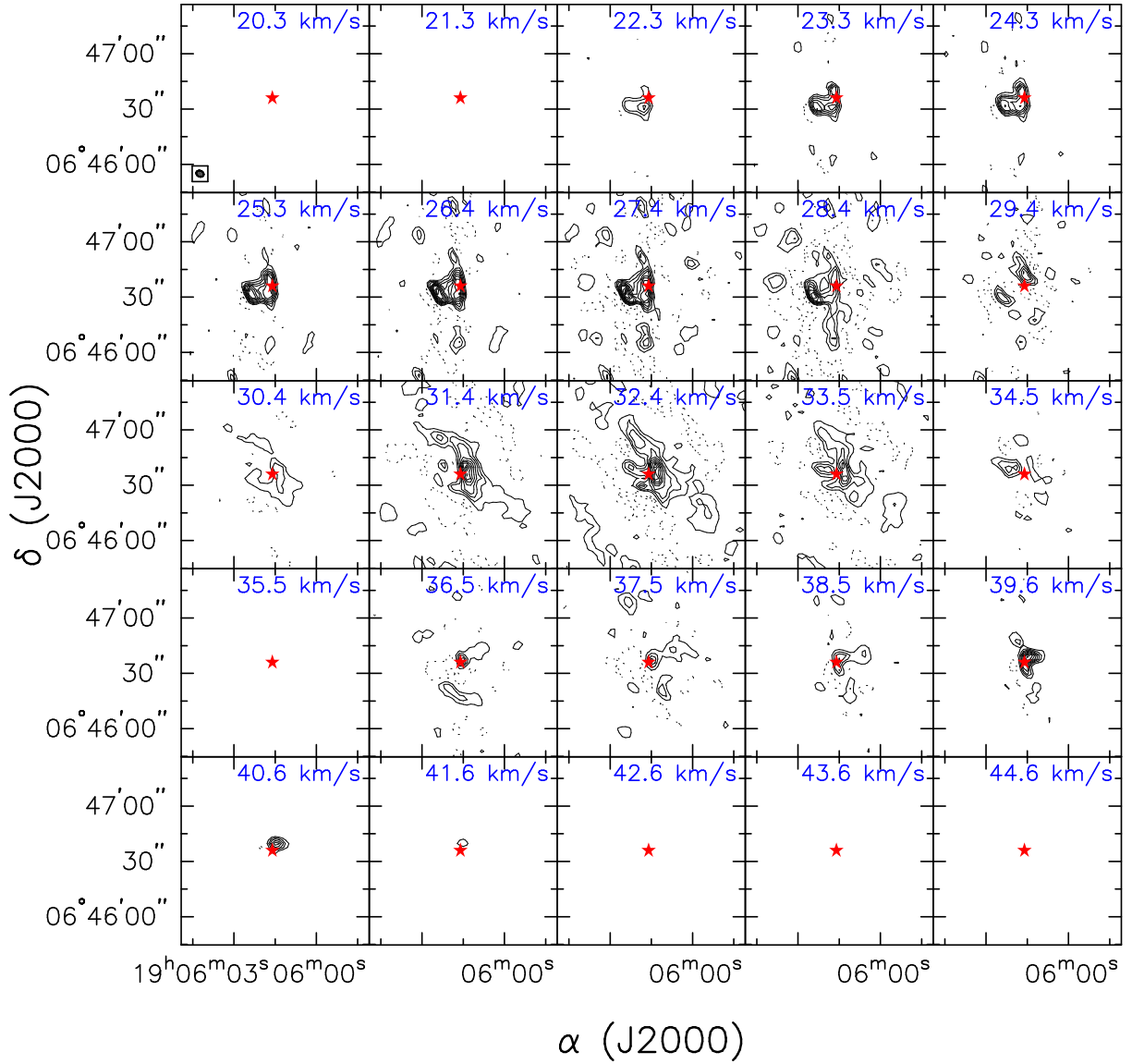


Fig. 5.— Channel maps of $^{12}\text{CO}(1-0)$. The red star symbol in the center of each panel marks the position of masers and IRAC point source.

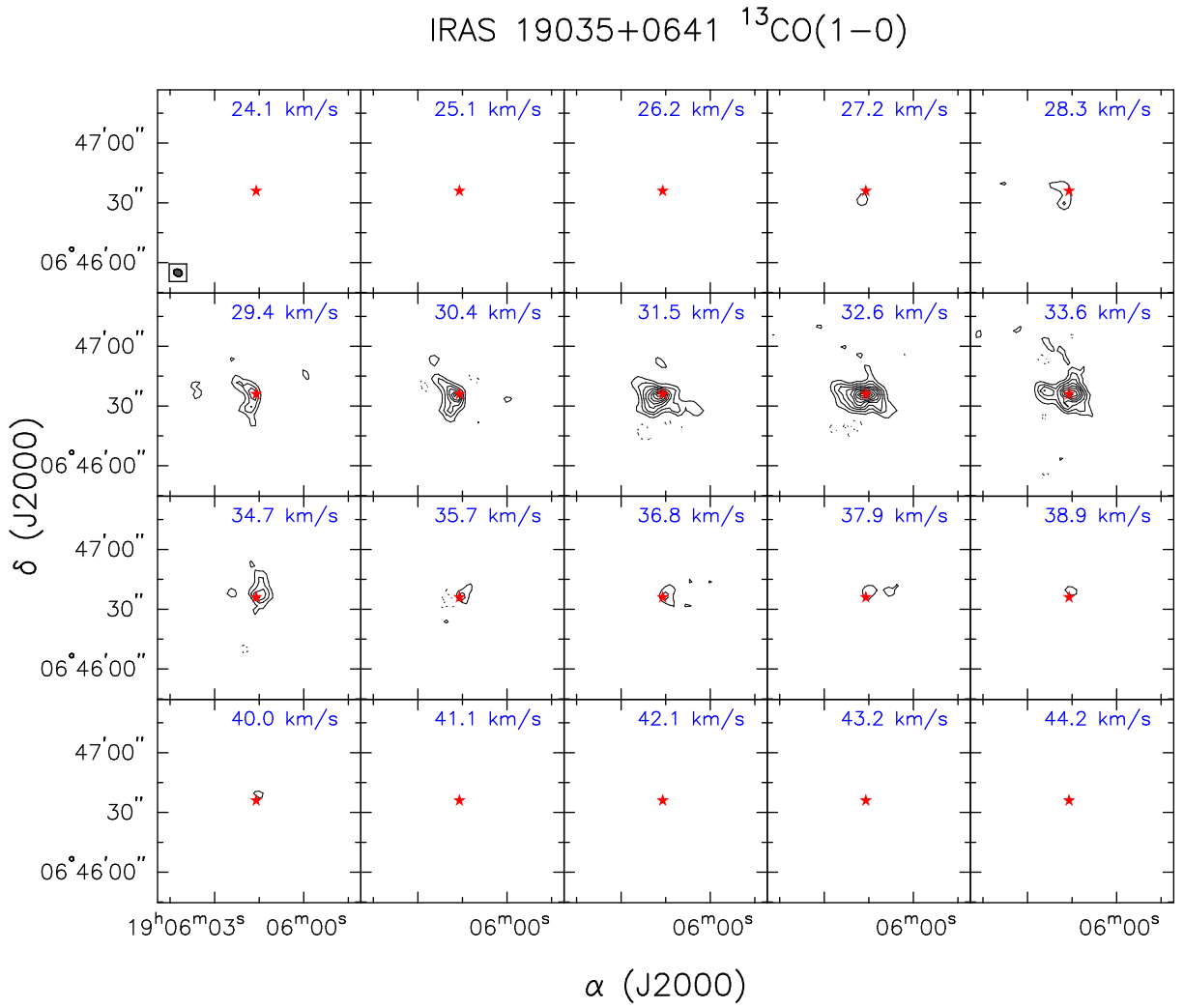


Fig. 6.— Channel maps of $^{13}\text{CO}(1-0)$. The red star symbol in the center of each panel marks the position of masers and IRAC point source.

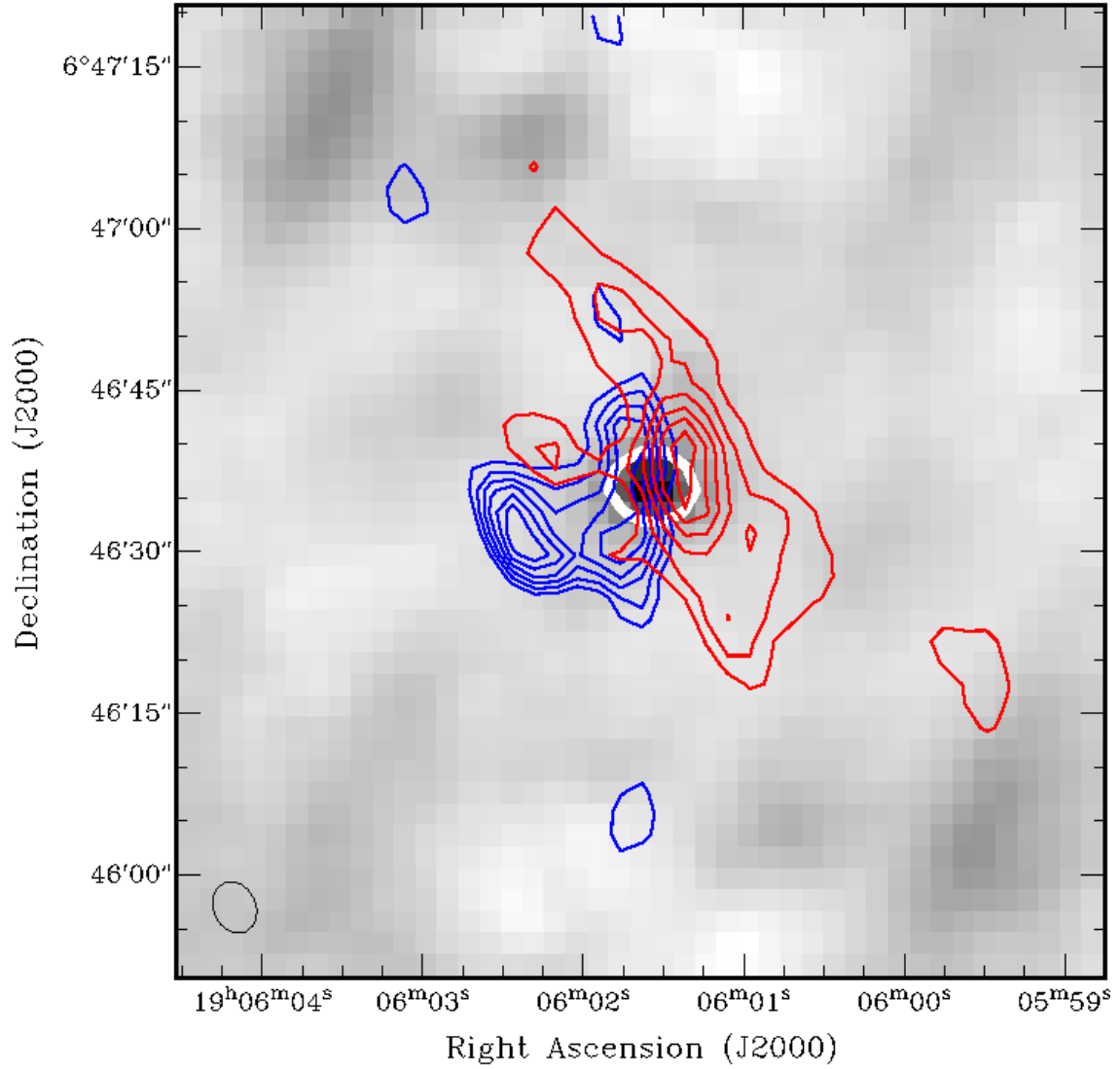


Fig. 7.— Renzogram of ^{12}CO . The blue contours are integrated intensity from 19 to 29 km/s, and the red ones from 31 to 38 km/s. The white circle shows the half-maximum of 3 mm continuum peak.

and the two components are outflows with uneven densities which lead to their asymmetry. In short we need more evidence to clearly understand what is happening here.

4.3.2. Continuum

The continuum intensity contours can be seen in Figure 4 and Figure 8. It is interesting that although it has almost a round shape, it extends into northwest and southeast, in which direction the outflows are seen in ^{12}CO .

We use the formula in Beuther et al. (2005) to calculate the total gas mass in this dust core. Note that we use $\beta = 1.5$ therein, and adapt the temperature from ammonia inversion lines observation, $T_{\text{dust}} \sim T_{\text{rotation}} \approx 25\text{K}$. The result is $\sim 100M_{\odot}$, a typical one for a massive star formation region.

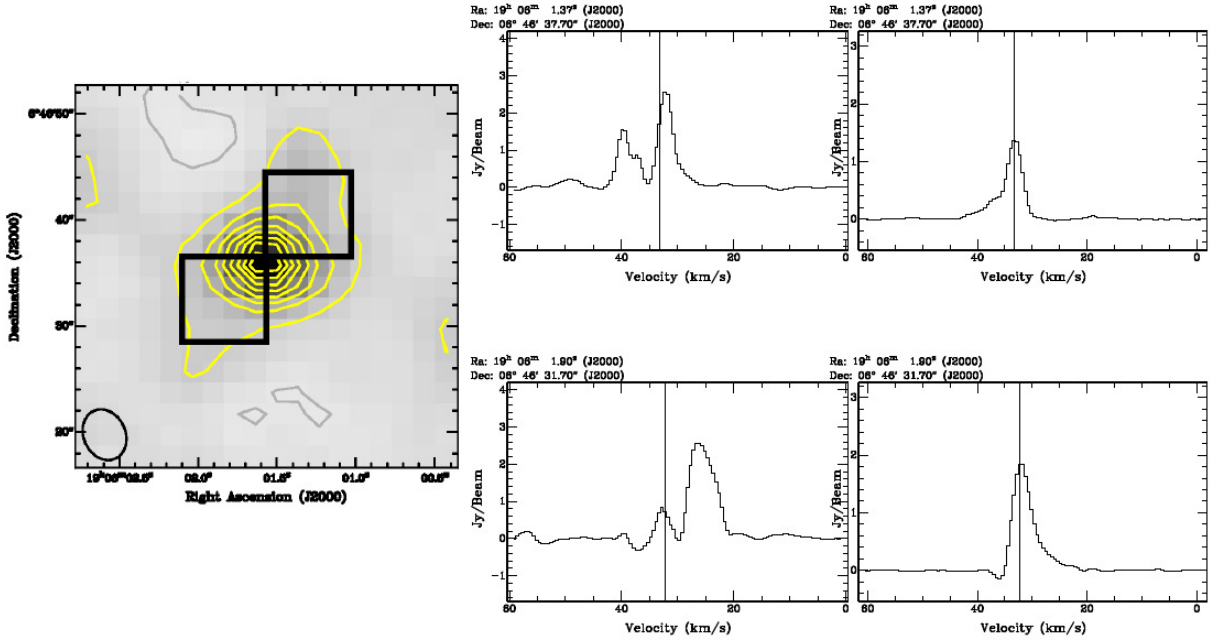


Fig. 8.— The yellow contours show continuum, and the two black squares are the area we select. The averaged spectra are shown in the right, the top two panels for northwest area, and lower ones for southeast area.

Acknowledgements

Thank all instructors and organizers of the school, thank all fellow students. Good luck and clear skies!

5. HCN and HCO⁺ in NGC 3368

Dyas Utomo

In this project, we looked for line emissions from HCN (1-0) and HCO⁺ (1-0) in NGC 3368 using the Combined Array for Research in Millimeter-wave Astronomy (CARMA). We select NGC 3368 because this galaxy has been observed during BIMA SONG Survey and has the strongest integrated intensity in CO, that is 12.80 ± 0.32 K km/s integrated over velocity from 670 to 1200 km/s (Helfer et al. 2003). With typical angular resolution of 6 arcsec, CO emission seems to be extended (Figure 9). NGC 3368 located at redshift 0.00299 or $V_{\text{LSR}} = 897$ km/s.

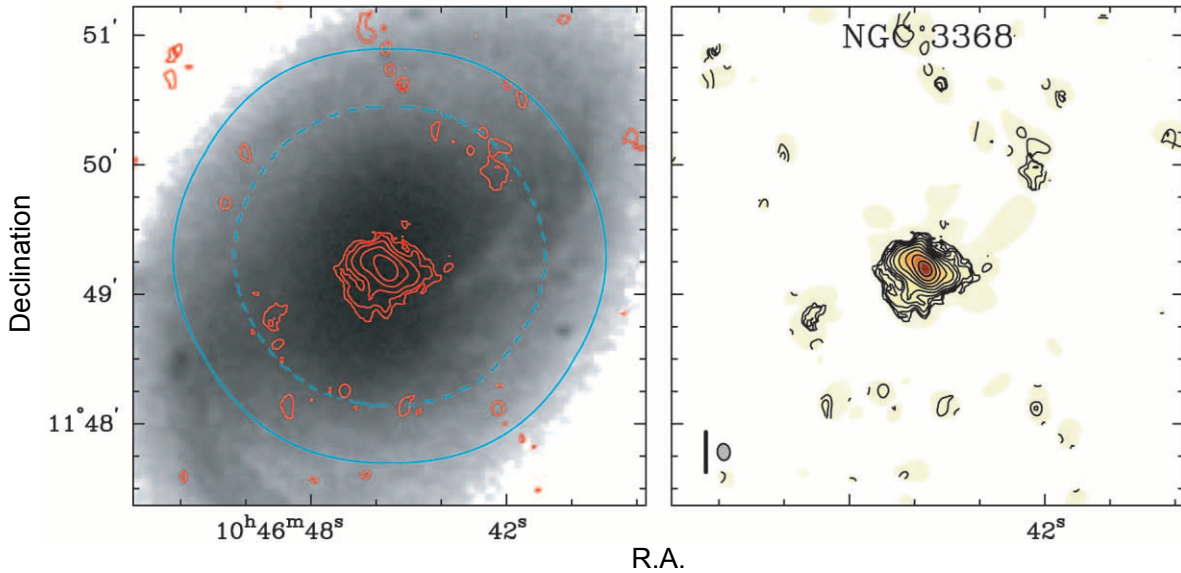


Fig. 9.— CO map from BIMA SONG Survey (Helfer et al. 2003)

The observations were taken on July 20, 2012 using 15 antennas (6×10.4 m and 9×6.1 m in diameter) in D array single polarization configuration. This configuration has baseline from 11 to 150 m, so the synthesized beam is about 6×4 arcsec in 3 mm wavelength. Our bandwidth is 350 km/s with resolution of about 5 km/s to capture possible board wing. The total observing time is about 7 hours.

The data are reduced using a standard MIRIAD script. The first 45 minutes of the data are flagged because the gain solutions are bad at that time. Also, we excluded 2 edge channels of each spectral window.

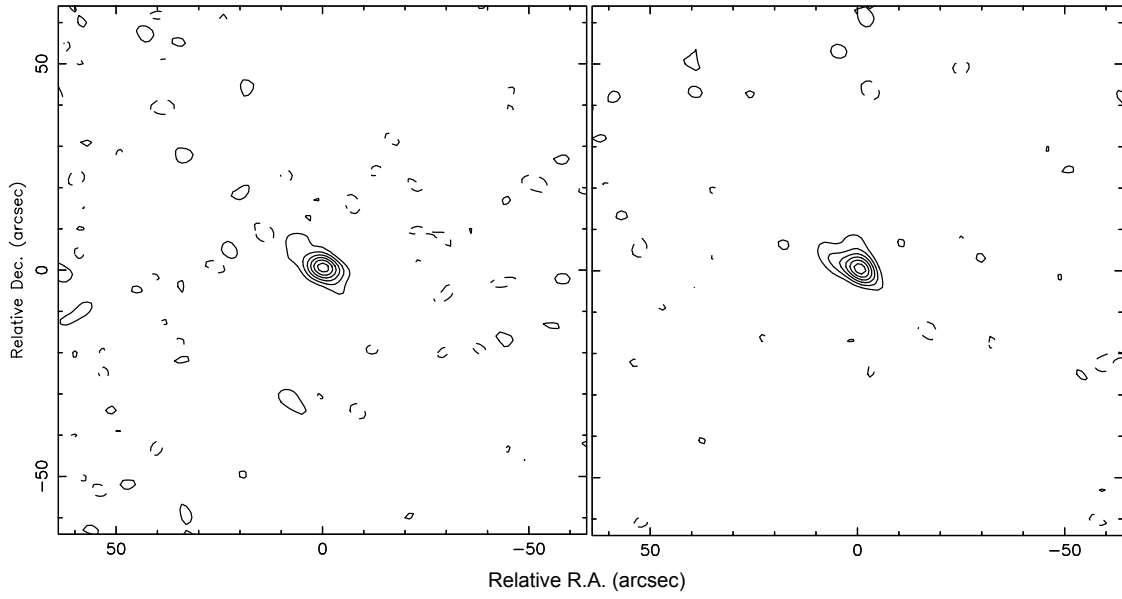


Fig. 10.— HCN (left) and HCO⁺ (right) maps from CARMA observations.

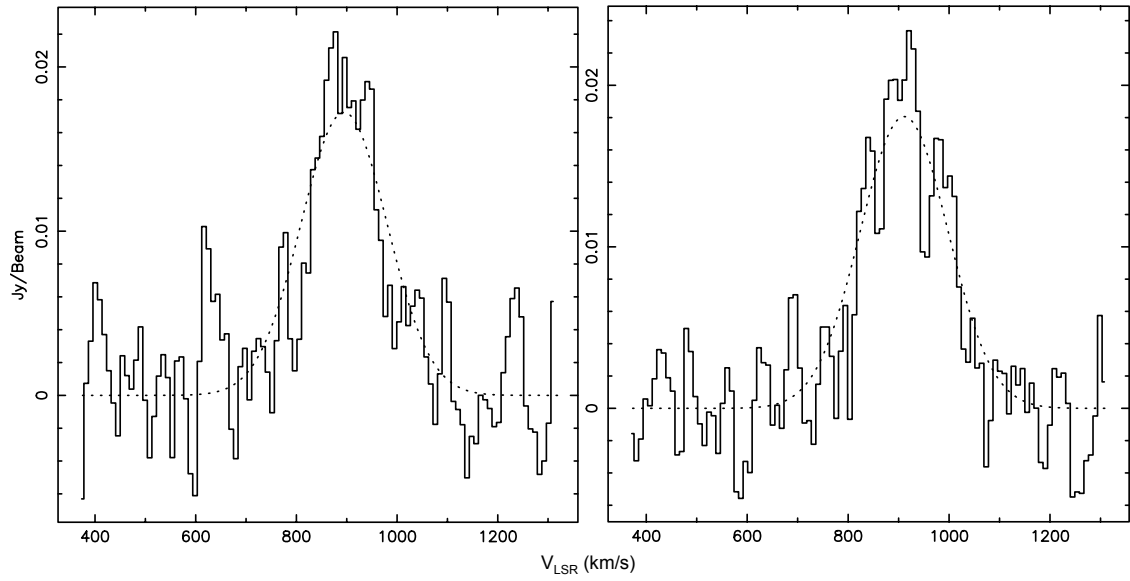


Fig. 11.— HCN (left) and HCO⁺ (right) spectrum with gaussian fits.

The result of our observations are intensity maps of HCN and HCO⁺ and their spectrum. Opposed to CO emission, HCN and HCO⁺ emissions are more concentrated at the center of the galaxy. The central regions of NGC 3368 included at least three distinct components: an outer bar with semi-major axis 61-75 arcsec, an ‘inner disk’ extending to 21-30 arcsec, and an inner bar 3.4-5.0 arcsec (Nowak et al. 2010). Therefore, HCN and HCO⁺ emissions seem to come from central bulge and inner bar with weak extended emissions probably from inner pseudo-bulge (see Figure 1 of Nowak et al. (2010) for clarity).

The spectrum of HCN and HCO⁺ are shown in Figure 11. The properties of those lines are given on Table 1. The spectrum are obtained from central region of the image with 2.5 arcsec wide (square shape) and Hanning smoothed. It seems that HCN spectrum show double horn emissions, sign of galaxy rotation, while HCO⁺ line shows more complicated structure which probably has 3 peaks.

Table 1: Gaussian parameters of line profiles.

Line	Amplitude (Jy/Beam)	Peak Velocity (km/s)	FWHM (km/s)
HCN	0.0172 ± 0.0014	894.6556 ± 8.2156	201.4995 ± 19.3450
HCO ⁺	0.0181 ± 0.0014	911.0255 ± 7.9060	205.1255 ± 18.6159

6. CO Distribution and Kinematics in NGC 7465

Mai Truong, UC Berkeley

6.1. Motivation

Early-type galaxies (ETGs) are galaxies that have lost most of their star-forming material; thus, they are likely to appear in the "red sequence" portion of the color-magnitude diagram (Baldry & et al 2004). Because ETGs have been shown to be deficient in star formation (Visvanathan & Sandage 1977; Bower et al. 1991), they are believed to have low content of molecular and atomic gas (Lees et al. (1991)). However, several recent studies have show that ETGs are not devoid of cold gas, but they contain reservoirs of dust (e.g., Hawarden (1981); Jura (1986); Knapp et al. (1989)), neutral atomic gas (e.g., Knapp et al. (1985); Sage & Welch (2006); Oosterloo (2010)) and molecular gas (e.g., Sage & Wrobel (1989); Welch & Sage (2003); Combes et al. (2007)). Studying the kinematics of the molecular gas distributions is one way to help understanding ETG formation and evolution. In this work, we observe the galaxy NGC 7465 in CO J=1-0 and ^{13}CO J=1-0 to extract information about the formation and evolution of the galaxy.

6.2. Observation and Data Reduction

NGC 7465 is a galaxy in the Pegasus constellation with $(\alpha, \delta) = (23 : 02 : 00.96, +15 : 57 : 53.3)$ (J2000), $v_{LSR} = 1960 \text{ km s}^{-1}$, and the CO emission flux previously recovered by CARMA is $F_{CARMA} = 93.6 \text{ Jy km s}^{-1}$. Using the available D-configuration at CARMA, we observed both the ^{12}CO ($\nu_{rest} = 115.27 \text{ GHz}$) and the ^{13}CO ($\nu_{rest} = 110.20 \text{ GHz}$) lines in the upper sideband with a bandwidth of 250 GHz. The weather was in optimal condition. Because of the large size of the source (over 1 arc minute), we started with a 19-point mosaic observation. However, to increase the sensitivity, we changed to a 7-point mosaic and later single-point observation.

Simple data reduction showed that the CO distribution appears to concentrate in a smaller region than the galaxy; thus the single-point observation sufficed in covering the entire CO emission. Unfortunately, due to the short observing time and the high resolution of the D array configuration, we were unable to retrieve emission data for ^{13}CO in this large scale structure.

6.3. Results and Discussion

The velocity map (Figure 12) displays a smooth transition from blue to red across the galaxy surface, indicating the existence of a rotating CO disk in the plane of the galaxy.

With closer inspection, the contour map (Figure 13) reveals extra features in the otherwise-typical position-velocity (PV) diagrams along the major axis (right panel) and the minor axis (left panel). Both panels show a flat but slightly declining rotation curve; the right panel shows an extra feature

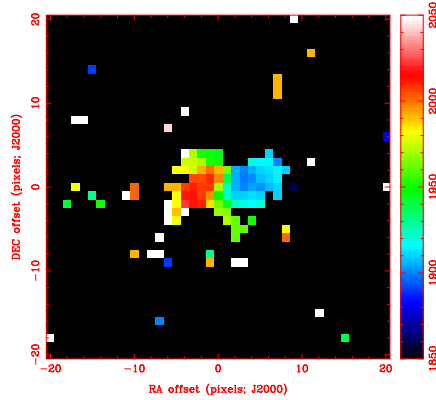
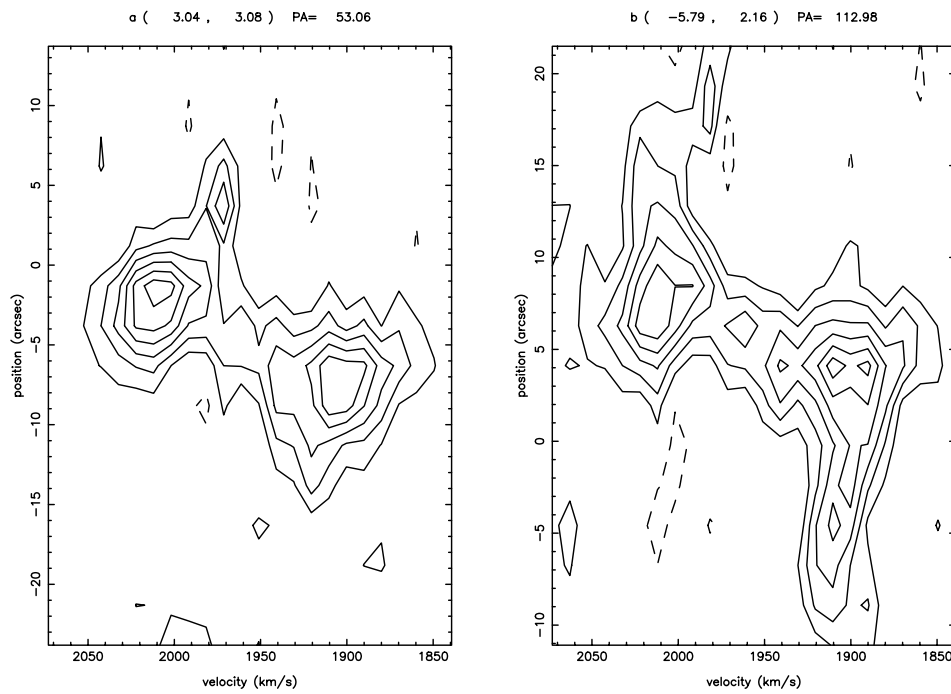


Fig. 12.— Mean CO(1-0) velocity map of NGC 7465

at 20 arcsec and 1980 km s^{-1} and the left one another feature at 4 arcsec and 1980 km s^{-1} , indicating that a spiral arm or a bar structure might be disrupting the CO flow from being circular. Thus, the diagrams give evidence of an elliptical CO ring, which would agree with the classification of NGC 7465 as an ETG, since ETGs are usually more elliptical than late-type galaxies.

Another interesting detail in the PV diagrams is the jump of 100 km s^{-1} within 10 arcsec, suggesting that NGC 7465 might belong to the X1- or X2-orbit family of galaxies (Skokos et al. (2002)), which have rotation curves that rise faster than predicted by the mass distribution. However, this result does not readily explain the formation and the evolution of the galaxy.

The moment-0 contour map (Figure 14) shows that the CO(1-0) distribution is not centered at $(0, 0)$. The small offset (of about 1 arcsec) implies that either the optical center is not well-defined, or the molecular gas is acquired from outside the galaxy instead of being expelled from the stars in the galaxy. Current work by Alatalo (2012) shows an overlay of the moment-0 map with the dust distribution that confirms the offset of the CO distribution. Thus, we have obtained evidence supporting that NGC 7465 was created by the merging of 2 galaxies. Because of the uniform distribution and the rotation curve, it is likely that the merging happened a long time ago. To determine with more confidence, we need to compare the rotation curve of CO with the rotation of the stars, and to map other molecular gases in the galaxy.



msf 21--Jun--2012 20:27

Fig. 13.— Position-velocity diagram of NGC 7465 along the major axis (right panel) and minor axis (left panel).

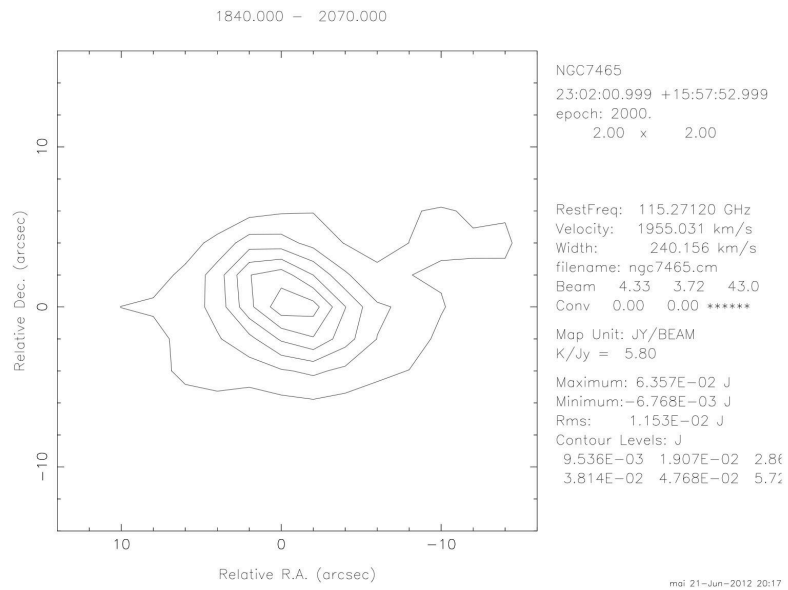


Fig. 14.— Moment-0 contour map of CO(1-0) distribution in NGC 7465.

7. Mapping the CO emission from IRAS 19312+1950

Pedro Salas

7.1. Motivation

IRAS 19312+1950 is a SiO maser source discovered by Nakashima & Deguchi (2000). This source presents the characteristics of both an asymptotic giant branch star and a young stellar object. To the day of this writing no definite evidence in support of any of these two scenarios has been found, but in any of the two cases this source presents some remarkable properties that make it interesting. If it is an asymptotic giant branch star, then it might lie in a dark cloud (Deguchi et al. 2004), making it an exotic object. Or if it is a young stellar object, then it would be one of the few that has a SiO maser.

7.2. Observations and Data Reduction

We observed the source IRAS 19312+1950 during the night of June 20 2012. The phase center of our maps was $\alpha = 19^{\text{h}}33^{\text{m}}24.3^{\text{s}}$ $\delta = +19^{\circ}56'55''$ (J2000). The source was observed for 5 hours, alternating each 20 minutes with the gain calibrator 2025+337. To calibrate the absolute flux scale we used Mars. We used the 15 antennas array in its D configuration during the observations.

We configured the correlator with 2×500 MHz spectral windows to observe the continuum. The remaining 6 windows were used to observe ^{12}CO ($J = 1 - 0$), ^{13}CO ($J = 1 - 0$), C^{18}O ($J = 1 - 0$), SO_2 ($J_k = 16_3 - 15_2$) and try to detect other molecular species. The details of the spectral lines observed are listed in Table 2.

Table 2: List of lines observed

Line	Rest Frequency (GHz)	Transition	rms (Jy beam ⁻¹)	Bandwidth (MHz)
^{12}CO	115.271	$J = 1 - 0$	0.4	31
^{13}CO	110.201	$J = 1 - 0$	0.23	31
C^{18}O	109.782	$J = 1 - 0$	0.16	31
SO_2	104.033	$J_k = 16_3 - 15_2$	0.02	125
Others	102.632	--	0.02	125
	101.951	--	0.01	250

To reduce the data we used John Carpenter’s data reduction script, provided during the summer school. Basically this script performs all the necessary reduction steps allowing the user to input the necessary flagging commands. After data reduction we inverted the uv data to generate images of the different spectral lines and continuum.

Initial inspection of the produced images revealed what could have been mistaken for large scale

structure. By comparison of our dirty beam with our dirty image we determined that large part of the structure resembled our dirty beam. Based on this, and the emission in our dirty maps, we conclude that in the field there is only a point source.

To determine the uncertainty in our flux density measurements we considered the rms noise at the source location and added a 20% flux uncertainty to account for inaccuracies in the absolute flux scale set.

7.3. Results

We detect the source in our 107 GHz continuum image, with an flux density of 13 ± 2 mJy. This result indicates that the continuum emission varies with time. Nakashima & Deguchi (2005) report a non-detection of the continuum emission at 107 GHz. With a 3σ upper limit of 3.3 mJy on January 2004, this implies a 75% flux density variation during this period. The source is unresolved by our $7'' \times 7''$ synthesized beam. The continuum emission map is shown in Figure 15.

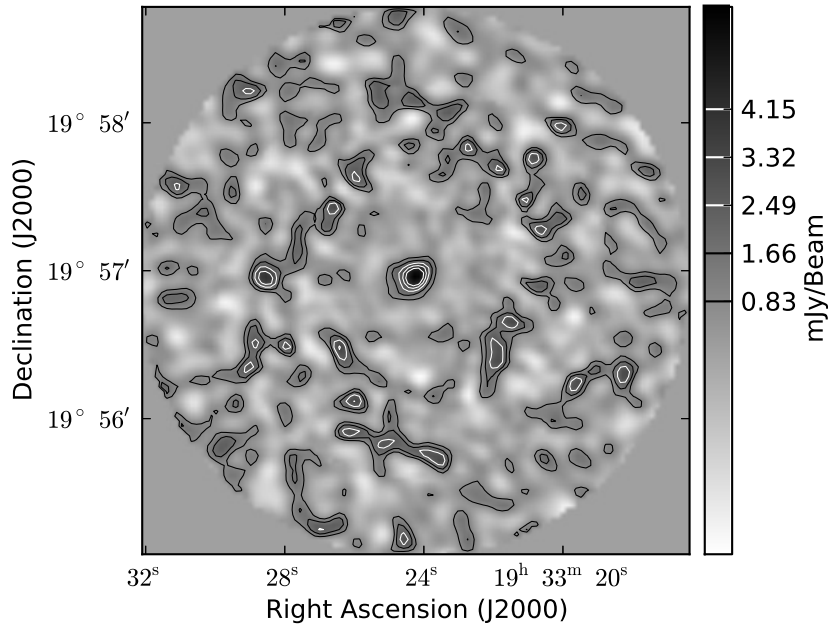


Fig. 15.— 107 GHz continuum map of the source IRAS 19312. The contours start at 1σ and increase every 1σ . The 1σ level is 0.8 mJy.

We do not detect any emission in our 102.632 and 101.951 GHz windows.

The ^{12}CO , ^{13}CO , C^{18}O and SO_2 line profiles at the image center are shown in Figure 16. In these we have separated the emission in three regions, a blue-shifted broad component, a narrow component

and a red-shifted broad component. The emission from the ^{13}CO and C^{18}O lines peaks at $v_{\text{lsr}} = 36$ km s^{-1} . The spectral resolution used here is better than that of Nakashima & Deguchi (2005). That is probably why we observe different peak velocities. This is clear when we look at the ^{13}CO line. There we see double peaked emission where using a lower spectral resolution would result in a shift of the peak velocity. This double peaked narrow line could mean that part of the outflow is interacting with the ambient gas. In the case of the ^{12}CO line the emission appears to peak at $v_{\text{lsr}} \sim 39$ km s^{-1} because of the presence of absorption features, probably due to foreground gas.

The SO_2 emission corresponds to background emission as it peaks at ~ 50 km s^{-1} .

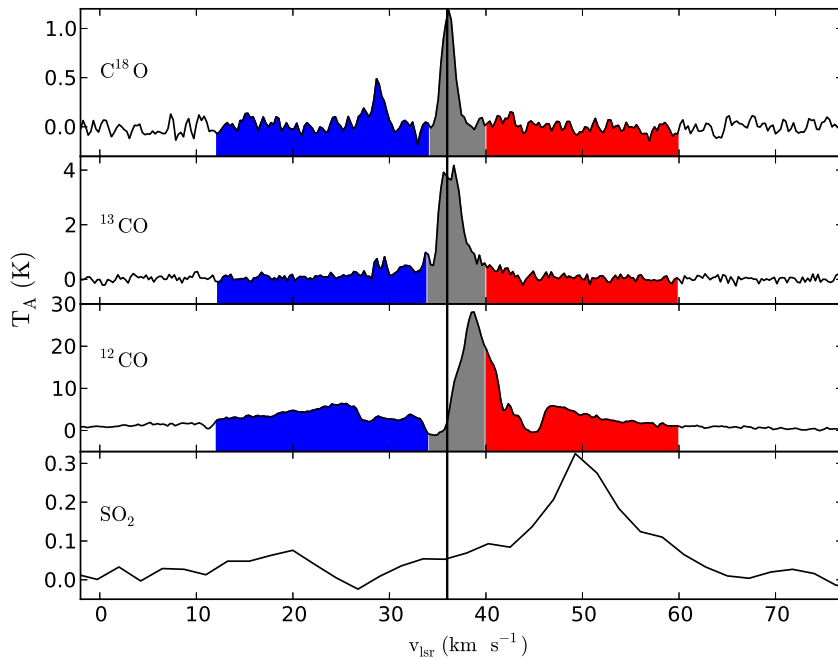


Fig. 16.— Spectra of the source on the ^{12}CO , ^{13}CO , C^{18}O and SO_2 lines. The colored regions correspond to the blue-shifted broad emission (blue), narrow emission (gray) and red-shifted broad emission (red). The SO_2 spectrum is not color coded. The dark line marks the peak of the ^{18}CO line at 36 km s^{-1} .

Velocity integrated maps of the narrow emission are shown in Figures 17, 18 and 19. In these we observe that the narrow emission originates from an extended source, and the peak is slightly displaced from the map center. Comparing our maps with those from Nakashima & Deguchi (2005), we observe that their maps reveal the structure of the source with more detail. This because our synthesized beam is larger, and we achieved less sensitivity than them. Also we defined the narrow emission to arise from a wider velocity range. We defined the narrow emission as originating from the velocity range $34 - 40$ km s^{-1} , while Nakashima & Deguchi (2005) uses $35 - 38$ km s^{-1} . But the overall shape of the narrow emission in our maps matches the previously observed ones.

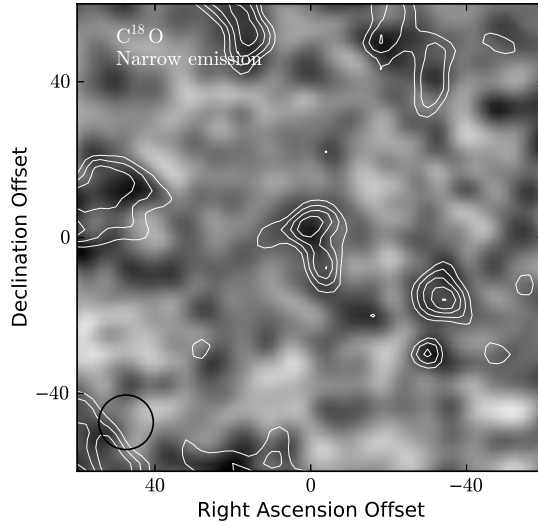


Fig. 17.— Velocity integrated emission from the $C^{18}O$ line spectrum. The spectrum was integrated over the velocity range $34 - 40 \text{ km s}^{-1}$ (contours). Contours start at 5σ and increment each 2σ . The 1σ level is $0.16 \text{ Jy beam}^{-1}$. The gray scale represents the total integrated flux over the spectral window. The synthesized beam is shown in the lower left corner.

In Figure 20 we present the velocity integrated emission from the ^{12}CO broad emission. We observe how the two components are shifted from each other, following the direction of the outflow. This provides evidence for the presence of a outflow in the vicinity of IRAS 19312+1950.

7.4. Future Work

Based on the observed spectral properties of IRAS 19312+1950 it would be interesting to perform the same observations with a higher spectral resolution. This could be accomplished given the large signal-to-noise of the emission lines using a 8 MHz window. With this we would be able to differentiate the different line components in the narrow emission. Other interesting experiment would be to map the source using the A configuration of the array to understand the spatial properties of the source.

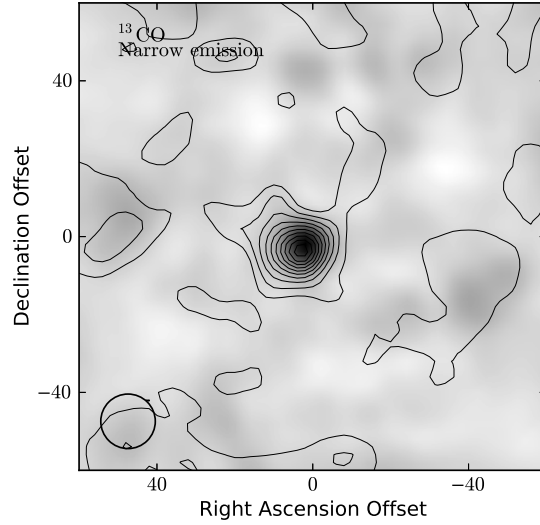


Fig. 18.— Velocity integrated emission from the ^{13}CO line spectrum. The spectrum was integrated over the velocity range 34 – 40 km s⁻¹ (contours). Contours start at 10 σ and increment each 20 σ . The 1 σ level is 0.23 Jy beam⁻¹. The gray scale represents the total integrated flux over the spectral window. The synthesized beam is shown in the lower left corner.

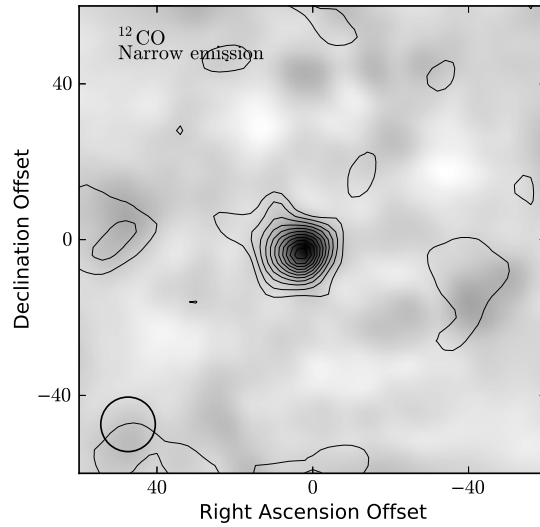


Fig. 19.— Velocity integrated emission from the ^{12}CO line spectrum. The spectrum was integrated over the velocity range 34 – 40 km s⁻¹ (contours). Contours start at 10 σ and increment each 10 σ . The 1 σ level is 0.4 Jy beam⁻¹. The gray scale represents the total integrated flux over the spectral window. The synthesized beam is shown in the lower left corner.

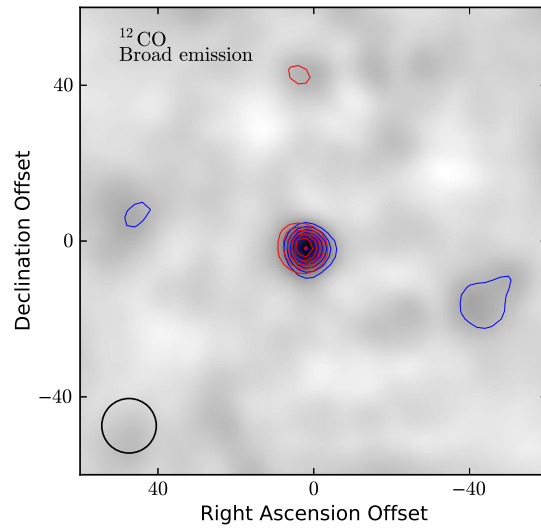


Fig. 20.— Velocity integrated emission from the ^{12}CO line spectrum. The spectrum was integrated over the broad emission, $12 - 34 \text{ km s}^{-1}$ blue-shifted emission (blue) and $40 - 60 \text{ km s}^{-1}$ red-shifted emission (red). Contours start at 40σ and increment each 20σ . The 1σ level is 0.4 Jy beam^{-1} . The gray scale represents the total integrated flux over the spectral window. The synthesized beam is shown in the lower left corner.

8. Observations toward Class-0/I protostar, [BHB2007]#11

Chihomi Hara

I present the preliminary results of the observations toward Class-0/I protostar, [BHB2007]#11 in the Pipe Nebula. The purpose of these observations is to reveal the detailed kinematics of the disk and the envelope.

8.1. Introduction

Stars are formed through the gravitational collapse of rotating molecular cloud cores, during which the collapsing system undergoes an increasing in density of 20 orders of magnitude. Eventually, Keplerian disks are formed and grow in the course of main accretion phase of the central stars. Recent observations have revealed the Keplerian disks with a size of a few hundreds to a few thousands AU. The Keplerian rotations (i.e., $v \propto r^{-1/2}$) are shown in their observations. Although, there are few protostars confirmed the rotation of the disk. Moreover, the differences of the density profiles and the temperature profiles between envelopes and disks associated with protostars in main accretion phases (Class-0 to I protostars) have not been revealed.

Fundamental questions about the disks associated with protostars in main accretion phases are:

1. Do the size and the mass of disks change with the evolution of central stars?
2. Rotating gas disks around early protostars result in the T-Tauri disks?

To reveal these questions, we should observe various rotating disks associated with early type protostars in some molecular lines.

The target of this observation is [BHB2007]#11 (hereafter, B59#11) at the star forming region, Barnard 59 (B59) in the Pipe nebula ($d=130$ pc; Lombardi et al. (2006)). It is suggested that B59#11 is in the transition phase from Class-0 to I, since the bolometric temperature is 70 K (Brooke et al. 2007). The rotating disk is suggested from observations in $C^{18}O$ emission. The outflow is ejected toward the plane of the sky direction, suggesting that B59#11 has the almost edge-on disk. The edge-on disks are suitable targets to investigate the detailed kinematics of the disk.

8.2. Observations and data reduction

We observed B59#11 ($(\alpha_{J2000}, \delta_{J2000})=(17^{\text{h}}11^{\text{m}}23^{\text{s}}, -27^{\circ}24'32''.9)$) using CARMA D configuration in single-pointing mode. The observations were carried out on June 21 to 22 for 5.5 hours. The total of on source time was 3.5 hours. The weather conditions were very good with a $\tau \simeq 0.4 - 0.2$

at 230 GHz during the whole track. The correlator setup included six 8 MHz narrow bands for several molecular lines ($\text{HCO}^+(1-0)$, $\text{H}^{13}\text{CO}^+(1-0)$, $\text{HCN}(1-0)$, $\text{N}_2\text{H}^+(1-0)$, $\text{SiO}(2-1)$, and $\text{CS}(2-1)$), providing the spectral resolution of 0.1 km/s, and two 500 MHz wide bands for continuum detection. We used MWC 349, the brightest radio continuum star as our flux calibrator, 3c279 as our passband calibrator, and 1733-130 as our complex gain calibrator. The images were obtained using the Maximum Entropy Method (MEM) and the beam size of $12'' \times 5''$ is provided for final deconvolved maps.

8.3. Results

Figure 21 shows the velocity channel maps in $\text{HCO}^+(1-0)$ emission. Each two channels are binned up. Blue shifted components exist on the northwest side of B59#11 and redshifted components exist on the southeast side. This direction is perpendicular to the outflow direction, suggesting the existence of the rotation of the dense gas envelope. Other blue- and red-shifted components exist on the southwest side of the protostar. This direction is consistent with the outflow direction and may indicate that the dense gas of the envelope is entrained by the molecular outflow. Two peaks exist at 4.1-4.2 km s⁻¹ velocity channels, implying the existence of the binary companion.

The results of observations in other molecular lines, $\text{H}^{13}\text{CO}^+(1-0)$ and $\text{CS}(2-1)$, are shown in Figures 23 and 24. The distribution of the H^{13}CO^+ emission is elongated toward NW-SE direction, perpendicular direction to the outflow. On the other hand, that of CS emission is elongated toward the direction of the outflow. These lines are considered to trace the rotating envelope and the outflow, respectively. Compact blue- and red-shifted components in CS emission, however, exist on the source position, and the direction of the velocity gradient is consistent with those of HCO^+ and H^{13}CO^+ emissions. This component seems to trace the envelope.

The velocity gradients on the source position in each line are compared in Figure 25. HCO^+ ($E_u=4.28$ K, $n_{\text{cr}}=1.7 \times 10^6$ cm⁻³) and CS ($E_u=7.05$ K, $n_{\text{cr}} = 6.0 \times 10^5$ cm⁻³) emissions trace the same region each other. On the other hand, H^{13}CO^+ ($E_u=4.16$ K, $n_{\text{cr}} = 2.7 \times 10^8$ cm⁻³) emission traces the outer region that has lower velocity. In Figure 25, the Keplerian rotation curve and the rotation curve of the envelope model are shown. It seems that the Keplerian rotation curve is better fitted than the black line. The blue-shifted emission in the HCO^+ line, however, is not fitted by two rotation curves, and it is bluer than other two lines. This may be because the outflow entrains the dense gas envelope. The distribution of H^{13}CO^+ line shows the “hole” at the source position. If the radial velocity profile shows the power-law ($v \propto r^{-\alpha}$), the high velocity component exists in the small region than low velocity component. Thus, the beam dilution affects the high velocity component. This is the reason for the “hole” structure and more high spatial resolution is needed to reveal the kinematics of the inner region.

8.4. Summary

1. All dense gas tracers show the velocity gradient toward the perpendicular direction to the outflow.
2. The results of observations in HCO^+ emission shows the Keplerian rotation, suggesting the existence of the 1000 AU scale disk.

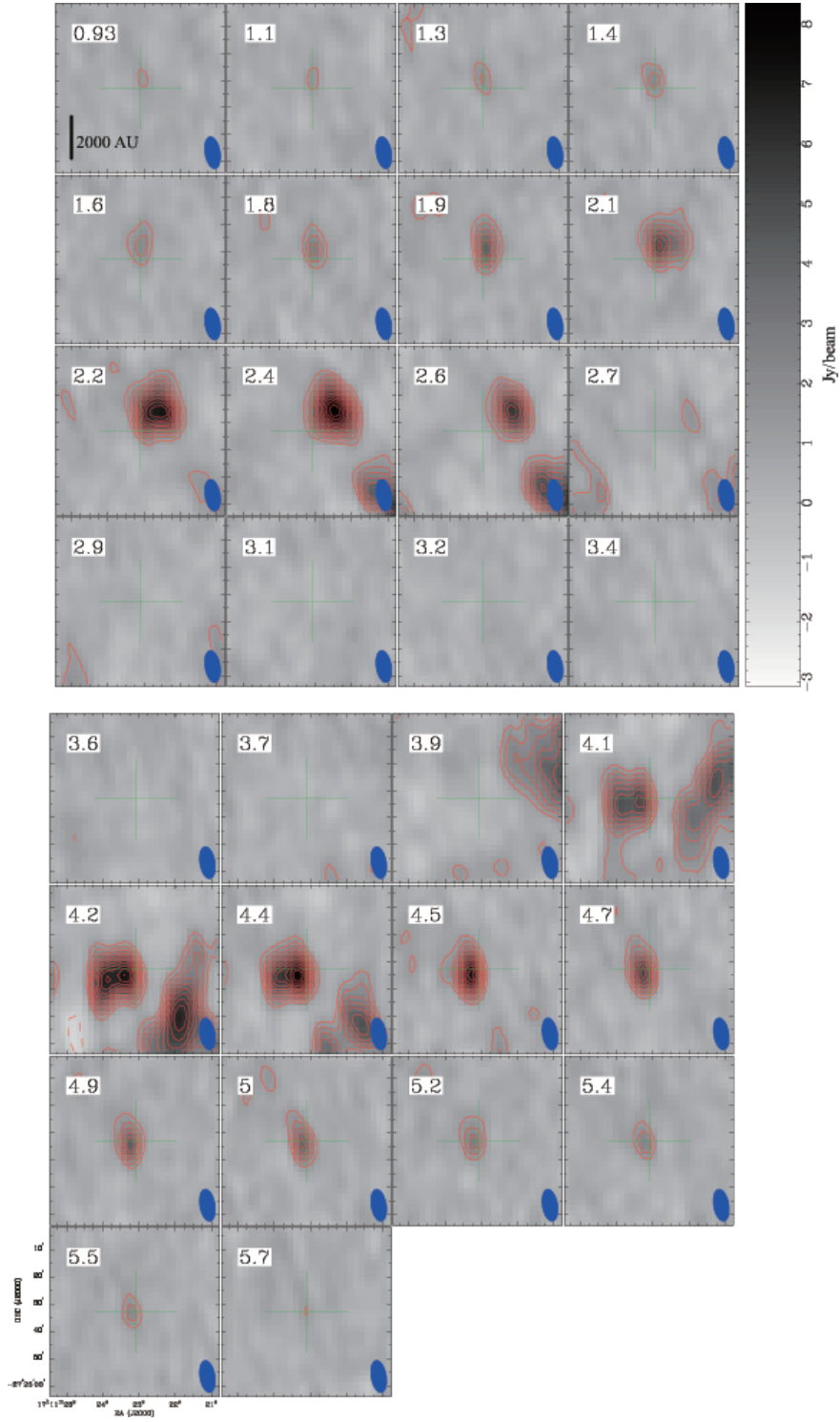


Fig. 21.— Velocity channel maps in $\text{HCO}^+(1-0)$ emission. Contour levels are $3, 4, 5, 6, \dots \times \sigma$ ($1\sigma = 0.4$ Jy/beam). Crosses show the position of the protostar. The blue ellipses at the bottom right side show the beam size of the map.

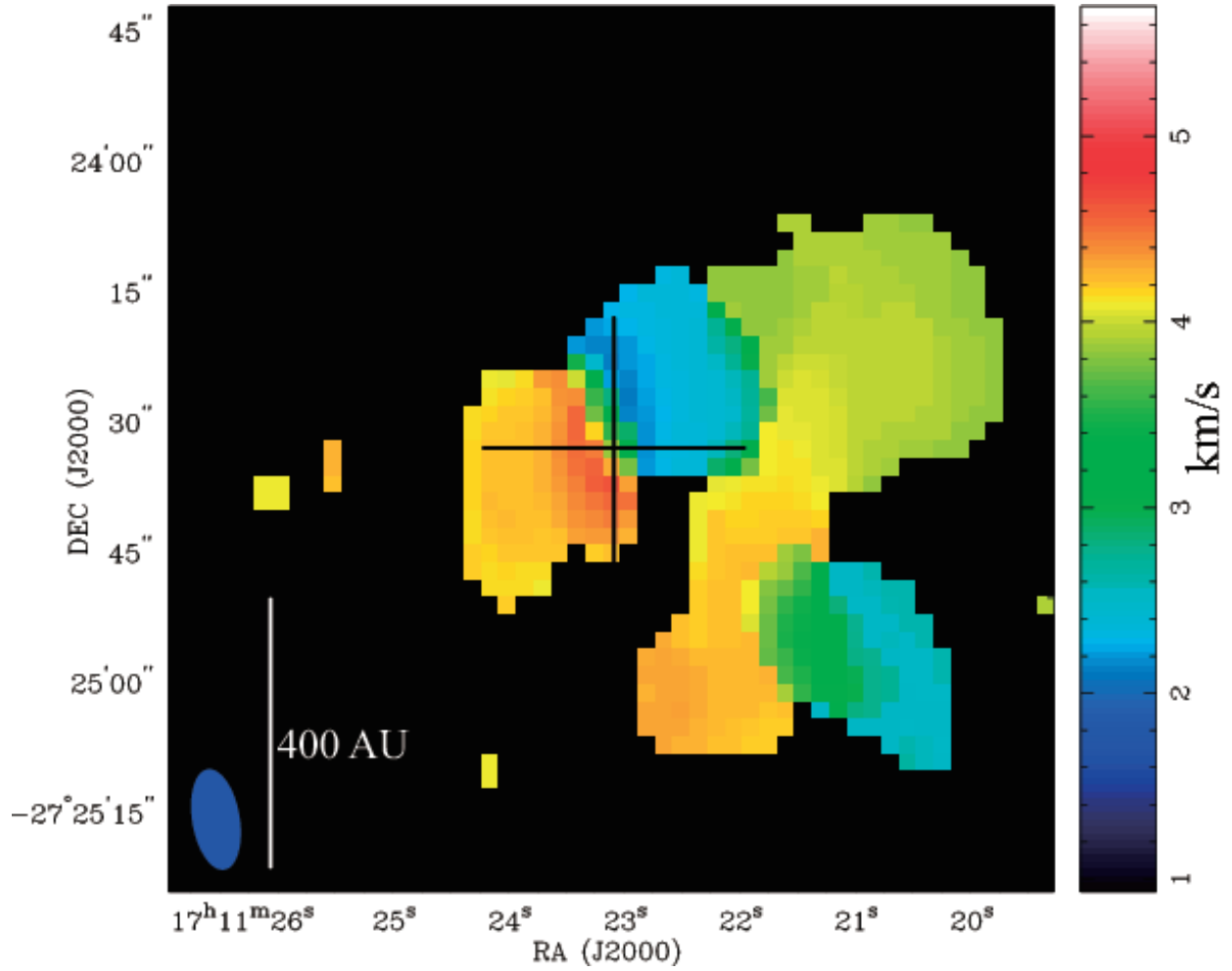


Fig. 22.— The first moment map in HCO⁺(1-0) emission. Symbols are the same as Figure 21.

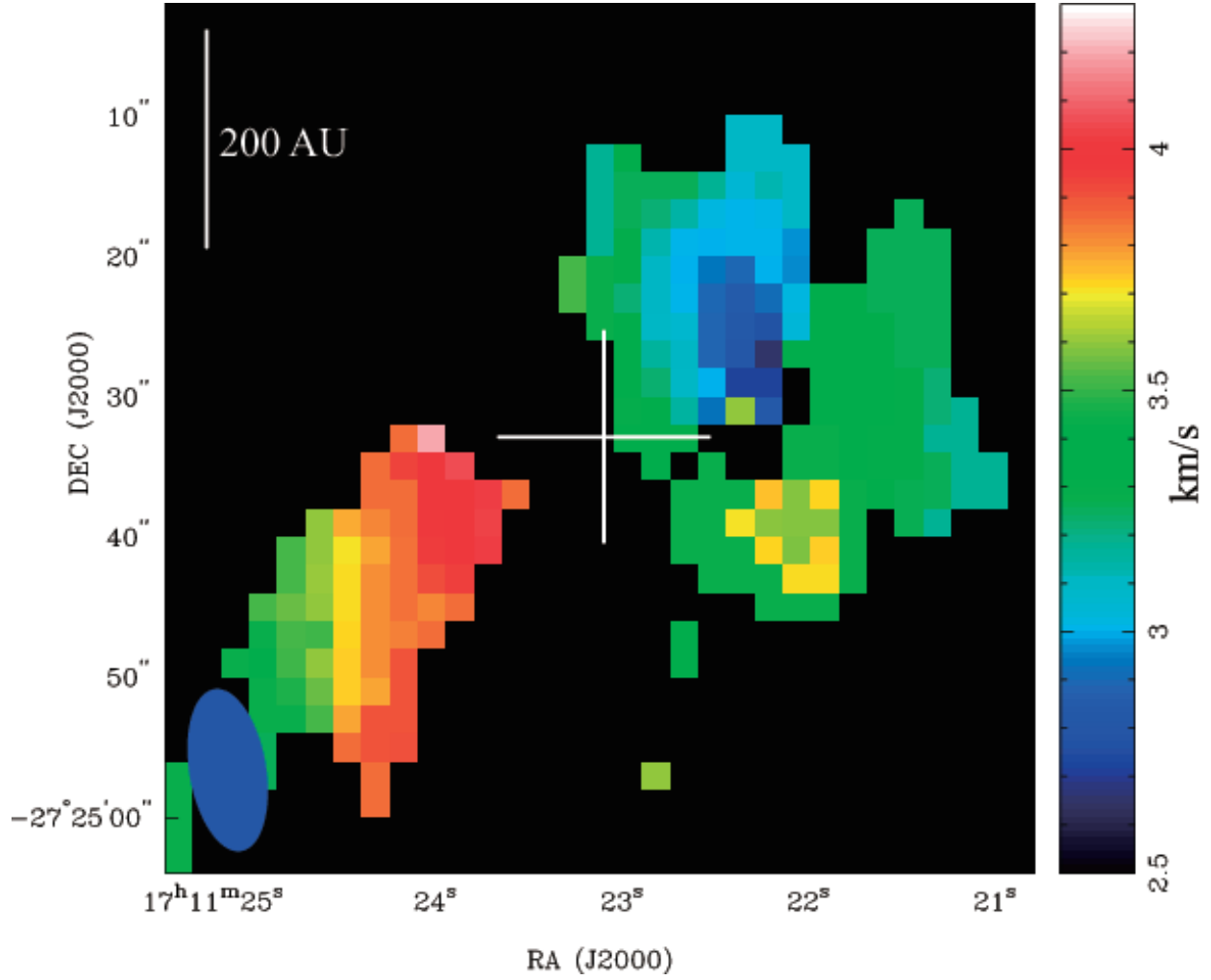


Fig. 23.— The first moment map in $\text{H}^{13}\text{CO}^+(1-0)$ emission. Symbols are the same as Figure 21.

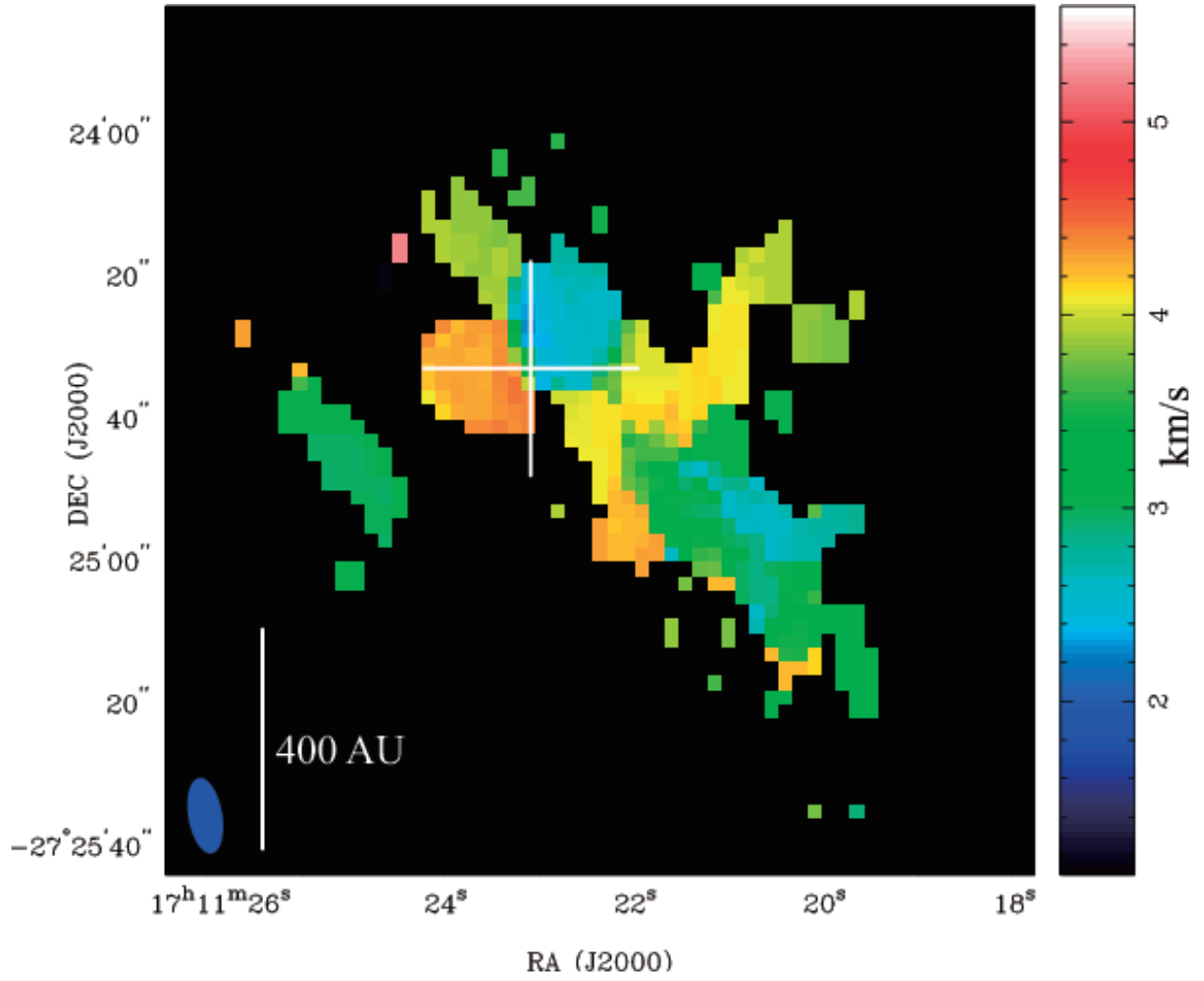


Fig. 24.— The first moment map in CS(2-1) emission. Symbols are the same as Figure 21

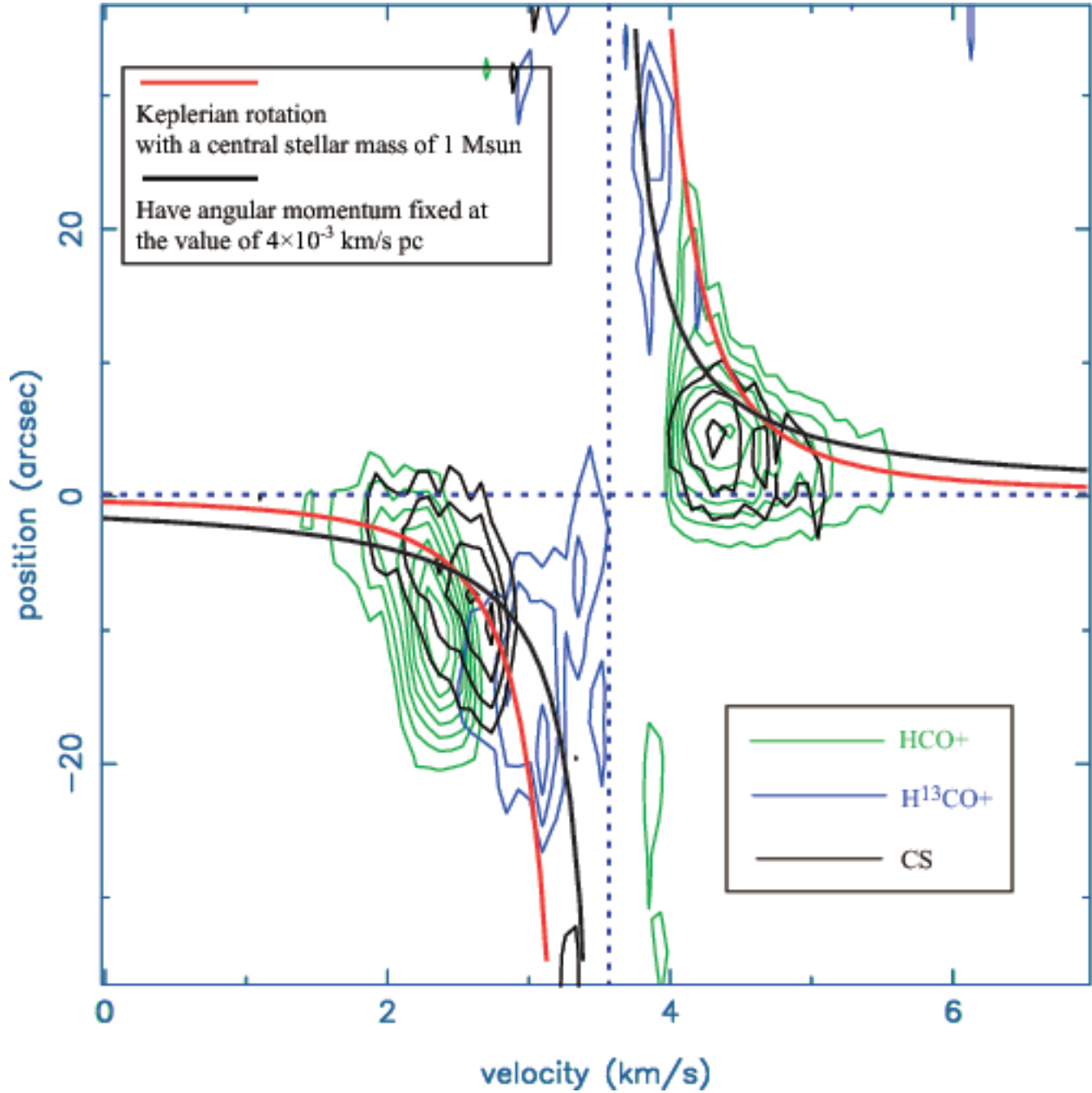


Fig. 25.— Position-Velocity diagram in HCO⁺, H¹³CO⁺, and CS emissions (Green, blue, and black contours, respectively). Contour levels are 3,4.5,6,... $\times\sigma$ ($1\sigma=0.6$ Jy/beam in HCO⁺ and CS, 0.4 Jy/beam in H¹³CO⁺). The red curve shows Keplerian rotation and the black curves show the angular momentum conservations law.

9. The Velocity Gradient of L1527

Dominique Segura-Cox (UIUC)

9.1. Background and Motivation

L1527 is a Class 0 protostar (Chen et al. 1995) located in the Taurus star-forming region, one of the closest star-forming regions at 140pc. This makes L1527 a convenient Class 0 protostar to study. L1527 has an envelope with a radius of 15,000AU (Tobin et al. 2008). L1527 has been found to have a disk, detected in scattered light, which measures 200AU (Tobin et al. 2010). It is unusual for a Class 0 star to have a disk detected. L1527 is also remarkable for its envelope velocity gradient.

L1527 has been observed by CARMA before in E-array configuration with the 10.4 and 6.1m dishes with CARMA-15 mode (Tobin et al. 2011). The N_2H^+ first moment map (Figure 26) reveals what appears to be a non-linear velocity gradient along the north-south axis of the image. The velocities go from redshift to blueshift, back to redshift, and finally are blueshifted again. This redshift, blueshift, redshift, blueshift morphology cannot be explained by simple rotation since simple rotation would yield a linear gradient going strictly from redshift to blueshift. We decided to use CARMA 2012 summer school observation time on L1527 because it is well-studied, has been observed by CARMA before and will thus guarantee a detection, and to further probe this redshift, blueshift, redshift, blueshift morphology in more detail. L1527 is an opportunity to use CARMA 2012 summer school observations to not only learn some science, but to do some science as well.

9.2. Observations and Data Reduction

The CARMA-23 observing mode is a heterogeneous array of all 10.4, 6.1 and 3.5 m antennas. This observing mode is ideal for imaging a range of spatial scales. The different diameter antennas allow interferometry observations to sample a larger range of spatial sizes than a homogeneous array. Because we wish to examine the velocity change on large and small scales in L1527, observing in CARMA-23 mode is ideal for the task.

One disadvantage to using CARMA-23 is that there are only four tunable windows in the upper side band (USB). We must choose our molecular lines carefully. Since N_2H^+ at 93.17 GHz appeared to trace the velocity reversal well in the previous CARMA-15 observations discussed above, we have selected this as a molecular line to target. We have also selected $H^{13}CO^+$ at 86.75 GHz and HCO^+ at 89.19 GHz for observation. We reserved one window for continuum observations. Taking these molecular line selections into account, we tuned the correlator to about 84 GHz so that the USB encompassed all three molecular lines we selected for observation. We used 8MHz bands for the molecular lines. For the continuum we used a 500MHz band centered on 92.75 GHz, which avoids all but the very faintest of emission lines. This correlator set-up results in a velocity resolution of

0.15km/s. The observations were carried out on June 19, 2012 while CARMA was in the D-array configuration. The weather conditions were extremely good, with $\tau < .3$ during the entire 5 hour track. This observation needed to be a mosaic so that we could examine the large-scale structure as well as the small-scale structure. We created a mosaic of seven pointings centered on L1527’s central source at RA(J2000.0)=04:39:53.89 and DEC(J2000.0)=26:03:09.6. We used Uranus as the flux calibrator, 0510+180 as the phase calibrator, and 3c84 as the passband calibrator

Data reduction was carried out using John Carpenter’s reduction script. C11 would not lock at 84GHz, so we flagged these data. The script first applies a baseline solution to the data. It then plots various types of track information such as system temperatures, amplitudes, phases, and spectra before calibration occurs. The data is then split into wide-band and narrow-band files and calibrations are applied. Spectra, phases, and amplitudes are again plotted for comparison to before calibration. Finally, this script then produces dirty images. The dirty images are processed using mospsf and mossdi so that a clean map is produced. Zeroth and first moment maps are produced. We are interested in the first moment map, which is essentially a map of the velocity gradient.

9.3. Results and Future Work

Data reduction resulted in the first moment velocity maps of H^{13}CO^+ , HCO^+ , and N_2H^+ (Figures 27, 28, and 29). In all three figures, north is up and the L1527 protostar is centered in the image. In the first moment velocity map of H^{13}CO^+ (Figure 27), going from the south-east to north-west of the image, we see redshift, blueshift, hints of redshift, and blueshift again. This is the same morphology seen in Tobin et al. (2011).

The first moment velocity map of HCO^+ (Figure 28) displays a different morphology than what is seen in H^{13}CO^+ . The outflows are well traced and for the most part, blueshifted. On the north-eastern area of the outflow there appears to be some redshift, which may be a result of the large opening angle of the outflow cones.

Obtaining the first moment velocity map of N_2H^+ (Figure 29) was more difficult than the other two emission lines. Signal-to-noise was much worse for this line compared to the others, and a taper was applied to the data in an effort to make the features stand out more clearly. Still, going from south-east to north-west, there is a hint of the redshift, blueshift, redshift, blueshift morphology present.

A possible explanation for the redshift, blueshift, redshift, blueshift morphology is a projection effect caused by a non-spherical, cigar-shaped envelope (Figure 30). The oval in the figure represents a cigar-shaped envelope about 25,000 AU across. If the envelope is slightly angled towards us and the material in the envelope is in-falling onto a rotating disk around the protostar, then the observed morphology is reproduced. As discussed above, L1527 has a disk detected in scattered light, which fits with this explanation of the non-linear morphology of the velocity gradient.

Future work will involve a more detailed analysis of the data presented here. In addition, there was another 5 hour observation of L1527 in CARMA-23 mode. We also selected L1521F as a second source and observed it for 5 hours in CARMA-15 mode and 5 hours in CARMA-23 mode. L1521F displays similar large-scale morphology to L1527, but does not have previous data resolved on small scales. These additional observations have not yet been processed.

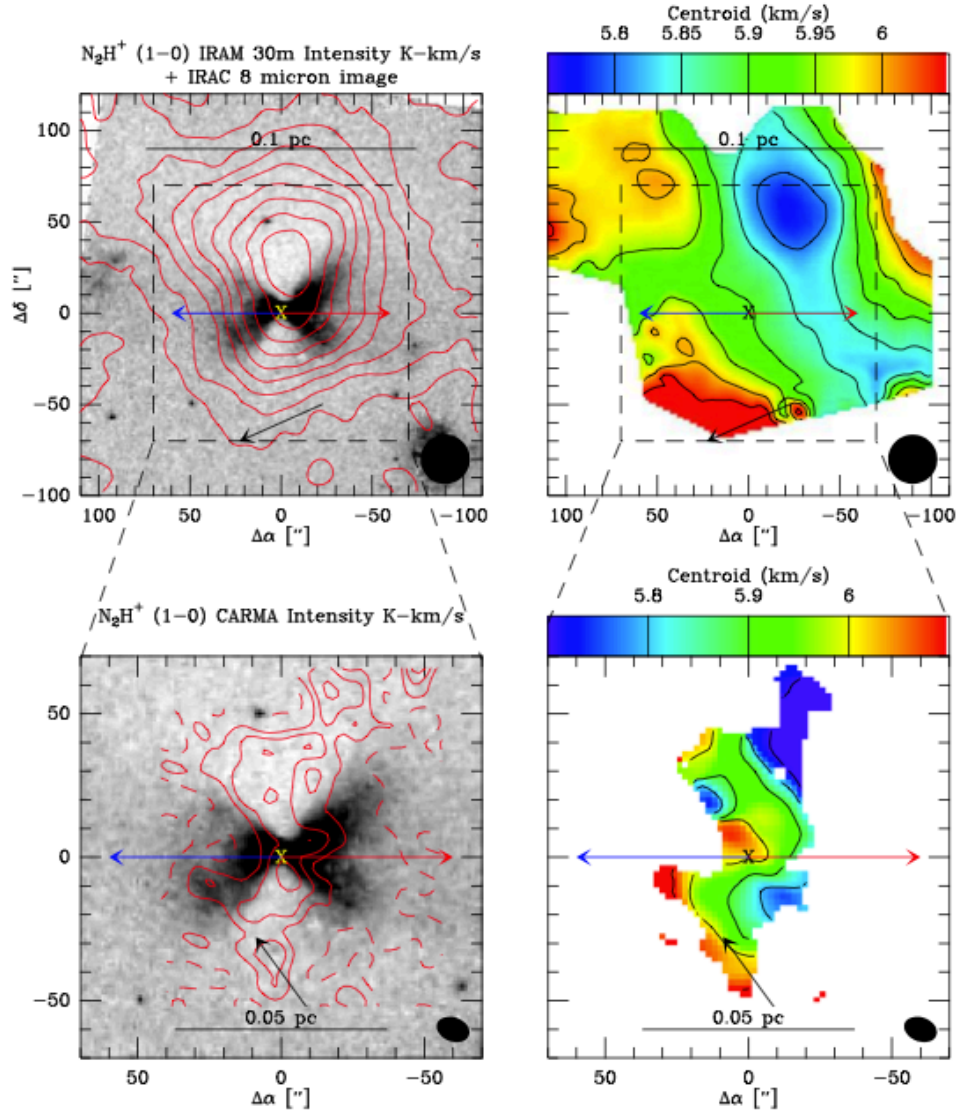


Fig. 26.— N_2H^+ data from Tobin et al. 2011. The bottom row are previous observations in CARMA-15 mode. Going from south-east to north-west in the lower-right image, we see a redshift, blueshift, redshift, blueshift morphology.

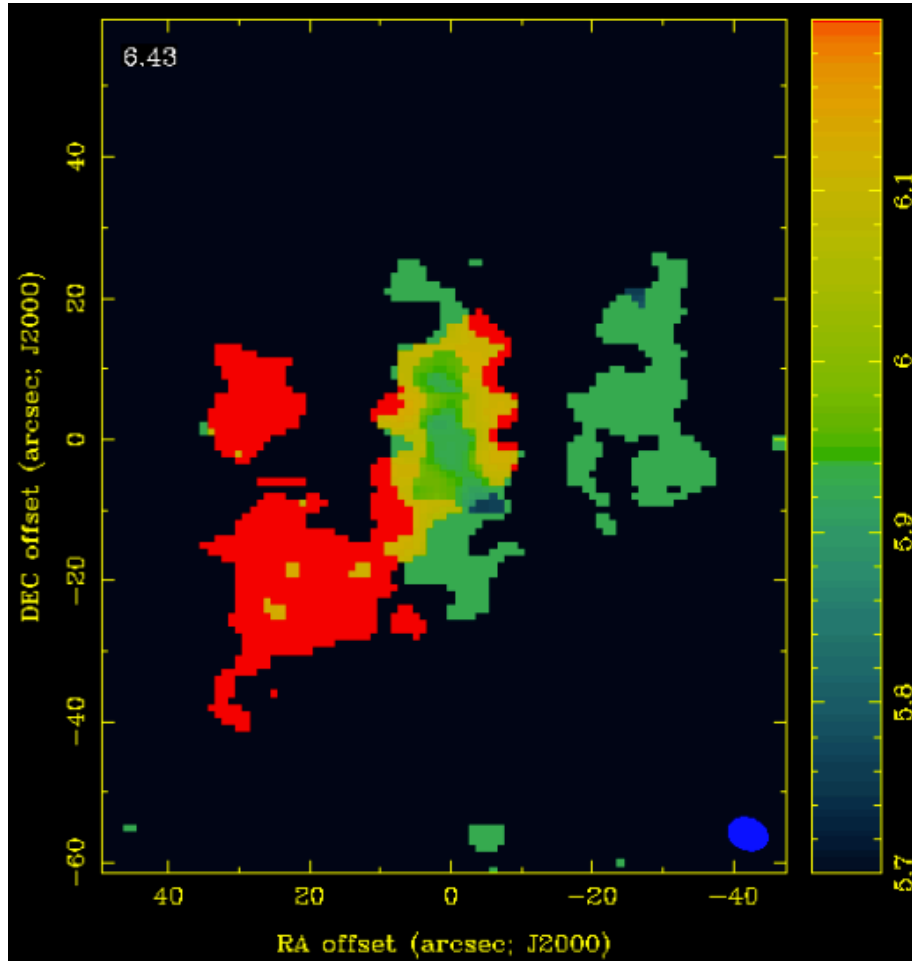


Fig. 27.— First moment velocity map of H^{13}CO^+ . North is up. The protostar is centered in the image. Going from the south-east to north-west of the image, we see redshift, blueshift, hints of redshift, and blueshift again.

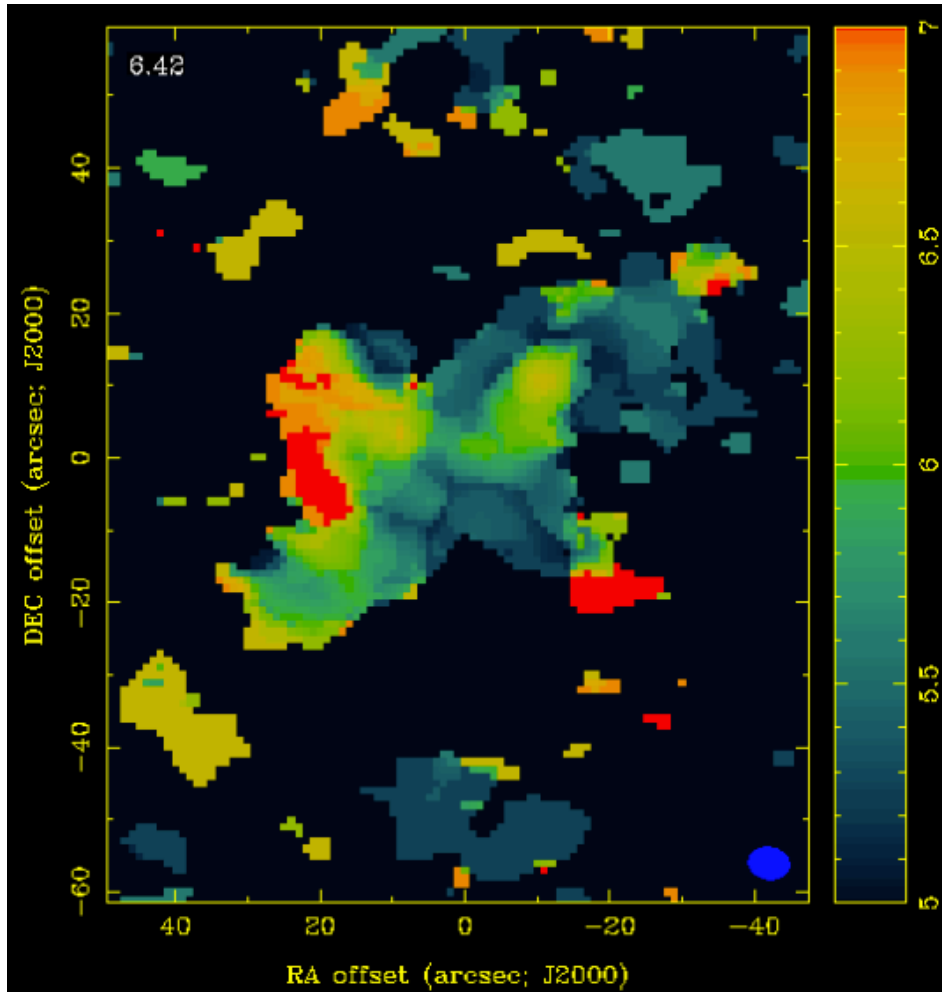


Fig. 28.— First moment velocity map of HCO⁺. The outflows are well traced and for the most part, blueshifted. On the north-eastern area of the outflow there appears to be some redshift, which may be a result of the large opening angle of the outflow cones.

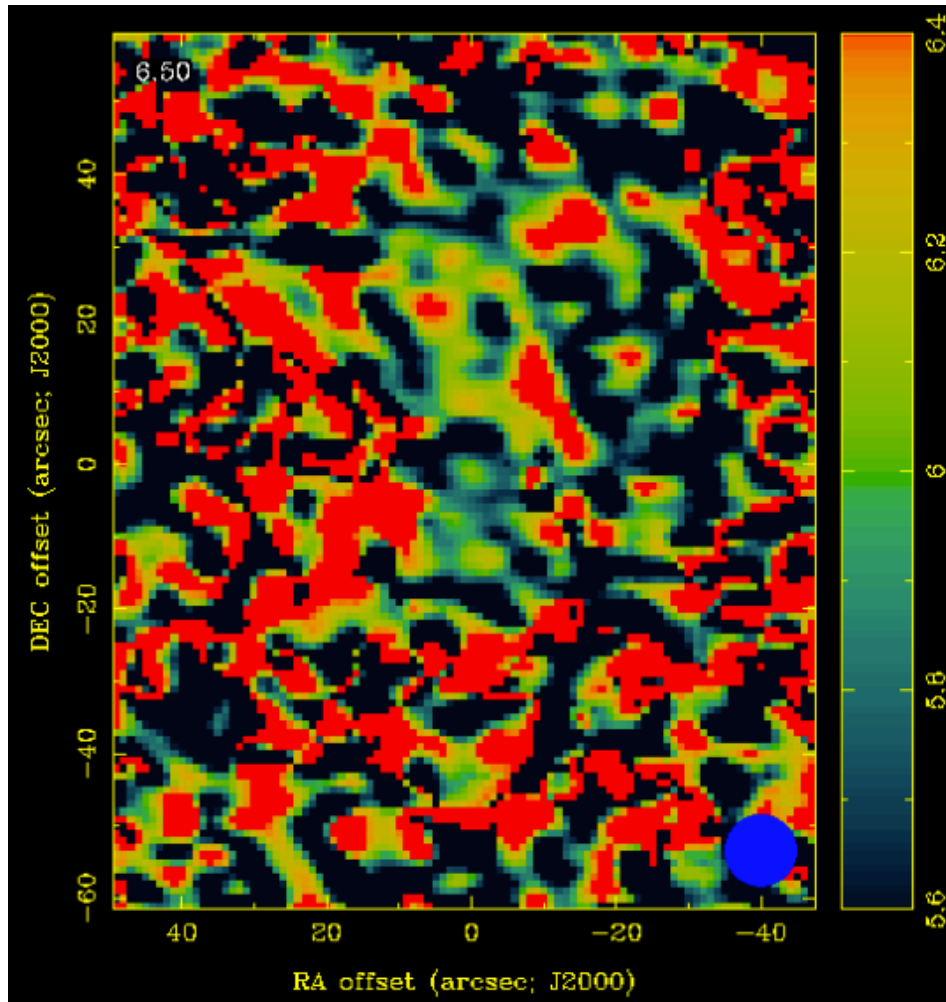


Fig. 29.— First moment velocity map of N_2H^+ . Signal-to-noise was much worse for this line compared to the others. Still, going from south-east to north-west, there is a hint of the redshift, blueshift, redshift, blueshift morphology present.

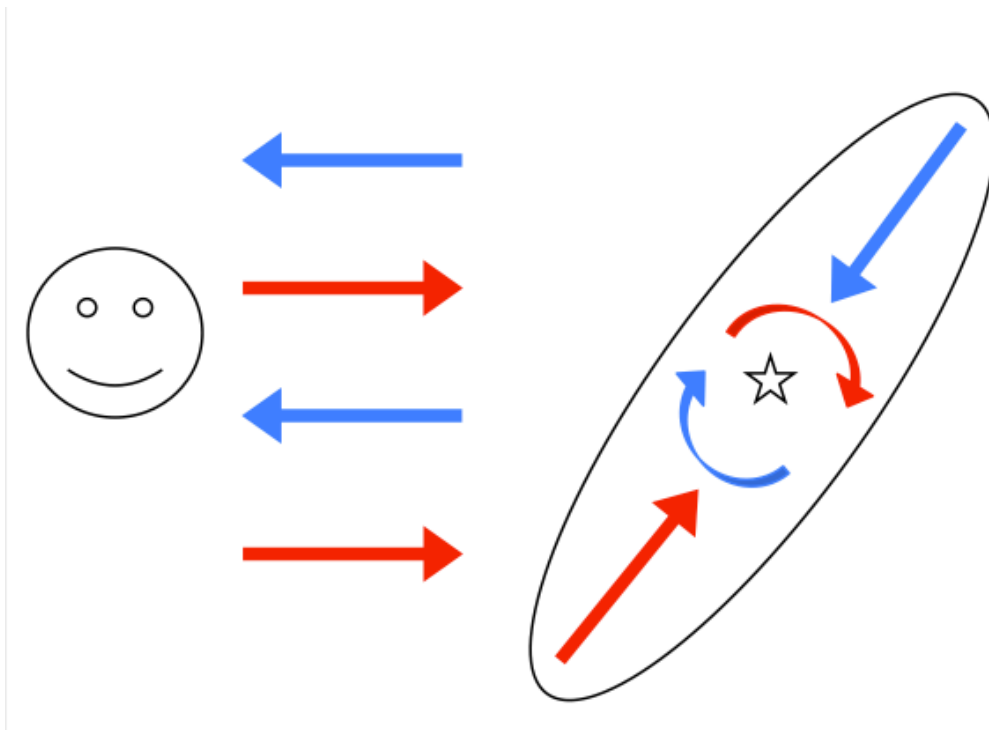


Fig. 30.— A schematic drawing of a possible explanation for redshift, blueshift, redshift, blueshift morphology. The oval represents a cigar-shaped envelope about 25,000 AU across. If the envelope is slightly angled towards us and the material in the envelope is in-falling onto a rotating disk around the protostar, then the observed morphology is reproduced.

10. A Study of Gas Surrounding a Young Stellar Object

Maria-Jose Maureia and Erin Grand

10.1. Introduction and Motivation

Young stellar objects (YSO's) are among the brightest stars in the night sky. The highly energetic formation of these systems creates a diverse environment worth investigating. These objects interact with the environment mainly through three components: an envelope, a circumstellar disk and a bipolar outflow/jet. Gas and dust inflow towards the protostar from the envelope and the circumstellar disk and, through the bipolar outflow, angular momentum is carried out from the protostar. Using radio interferometers is possible to study the physical properties of these three components.

Depending on the level of evolution of the protostar the YSO's can be classified from Class 0 to III. Class 0 corresponds to a deeply embedded recently formed protostar. Class III corresponds to a protostar in the contraction towards the main sequence, with little gas and dust left in the disk.

For this project we observed the YSO L1689S located in the star forming region ρ -Ophiuchus ($d \sim 100$ pc, $LSR \sim 5$ km/s). The object was previously classified as Class I by Bontemps et al. (1996). This class corresponds to a protostar surrounded by both a disk and a residual envelope of substellar mass.

The circumstellar disk was previously observed in $HCO+(1-0)$. Figure 31(a) shows the integrated intensity maps in 3mm and $HCO+(1-0)$. The continuum shows the position of the source. The molecule appears to be tracing the disk. Figure 31(b) shows a p-v cut through the disk. The kinematics is consistent with being Keplerian.

Also, an extended bipolar outflow was previously detected in Bontemps et al. (1996) using $CO(J=2-1)$. Figure 32 shows the location and direction of the outflow.

Our goal for this project was to map the circumstellar disk in ^{12}CO , ^{13}CO and $C^{18}O$. Based on this information, we can obtain the kinematic of the disk and, as a future work, we can infer the dynamical mass of the object.

10.2. Observations and Data Analysis

We set out to observe ^{12}CO , ^{13}CO and $C^{18}O$ in the YSO. We centered the 8 Mhz windows on the rest frequency of these lines and placed 500 MHz bands elsewhere for a continuum analysis. We tried not to place the 500 Mhz windows over any strong lines to avoid any contamination to the continuum. We chose to observe 1625-254 as a phase-calibrator, 3C279 as a passband calibrator, and Mars as a flux calibrator.

We observed one 5 hour track on our source. The weather was good for a 3mm observation and

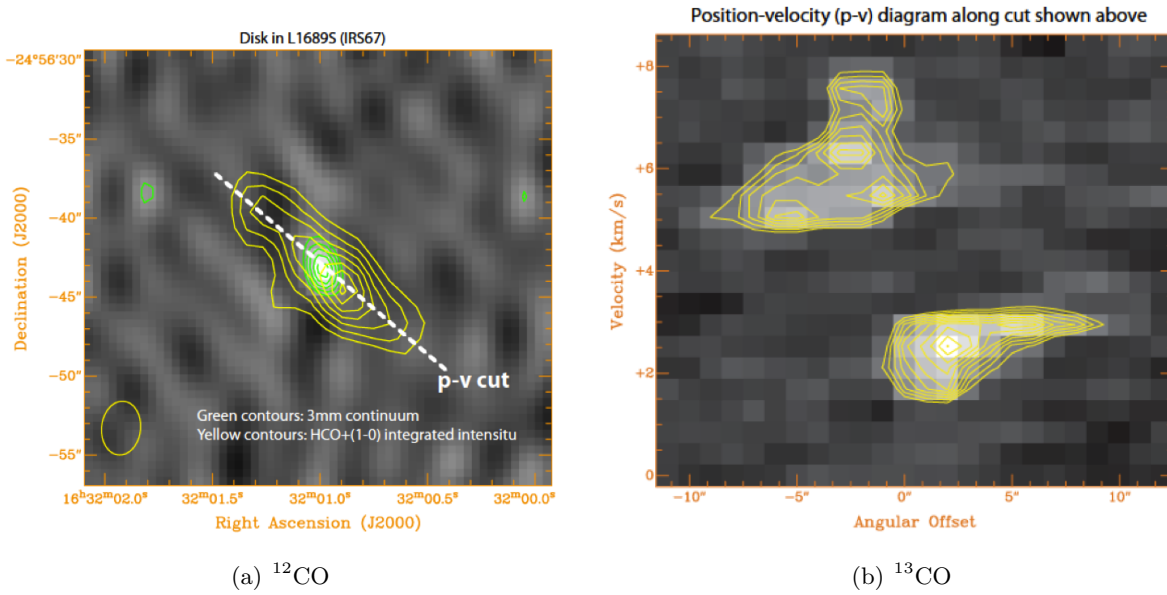


Fig. 31.— Integrated intensity map in 3mm and HCO+(1 – 0). Also is shown a p-v cut where it can be inferred a Keplerian kinematic.

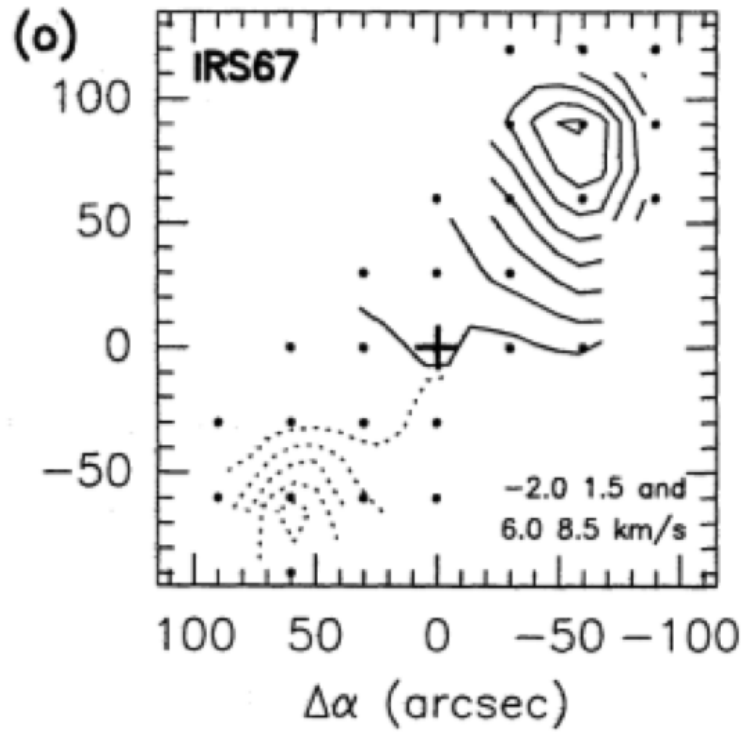


Fig. 32.— Outflow traced in CO($J = 2 - 1$). Figure from Bontemps et al. (1996)

the array did not have any major problems. Due to our source having a low declination, at various points along the track some antennas were shadowed. These data was flagged out right away along with some very high system temperatures. We applied phase and flux calibrations to the data and separated out the different lines to make channel and moment maps.

10.3. Analysis

The wings in the ^{12}CO emission maps leads to the possibility that the CO seen may be from along the line of sight and not associated with the source. Figure 33 presents our integrated intensity maps for the three molecules as well as a continuum image. On these integrated intensity maps is not clearly distinguished the circumstellar disk as in Figure 31(a). This is expected since HCO^+ traces a much more dense gas. However, the three maps show a slightly elongated geometry consistent with the orientation of the HCO^+ contours.

Figure 34 shows the spectrum of ^{12}CO and ^{13}CO . The ^{12}CO emission shows a red and a blue emission and no emission at the velocity of the source. The absent of emission at the rest frame velocity could be due to the gas is more optically thick at this velocity. This is consistent with the detection of ^{13}CO at that velocity.

We need to examine the position of the red and blue emission in order to study the possibility that these wings correspond to the base of the outflow and/or the emission from the disk. Figure 35 shows intensity contours in velocity space (i.e. separating the blue and red emission). The contours do not allow a clear identification of the emissions with the base of the outflow or the disk. However, it is important to notice that both are centered in different locations with respect to the continuum position.

The blue emission might be in agreement with the blue part of the disk. Also, if we integrate in the same blue velocity range as in Bontemps et al. (1996), it is consistent with being the base of the outflow. On the other hand, the red emission has a more confusing distribution in space. If we integrate in the same red velocity range as in Bontemps et al. (1996) is consistent with the location of the red part of the disk but not with the red wing of the outflow. However, in the total integrated map we do observe emission elongated towards the direction of the red portion of the outflow. Figure 36 shows the integrated velocity map of the red and blue emission in ^{12}CO in the same ranges used by Bontemps et al. (1996) to identify the outflow (Figure 32). Notice that the colors in this map are inverted with respect to the usual convention. The red contours corresponds to the blue emission and vice versa.

Another alternative is that the ^{12}CO emission is coming from two different sources. However, we do not see evidence for a second source in the other lines.

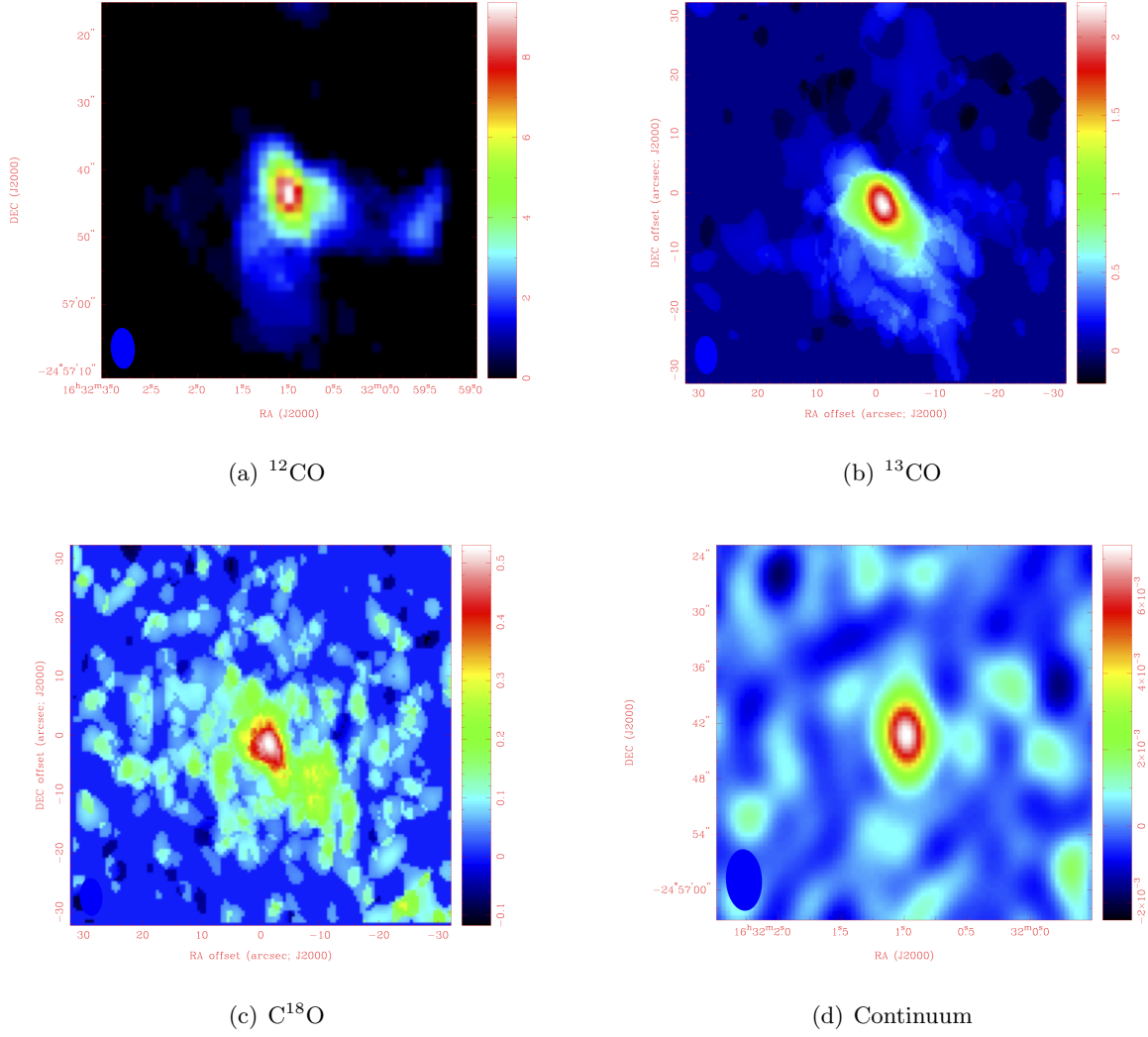


Fig. 33.— Integrated Intensity Maps of the Molecules

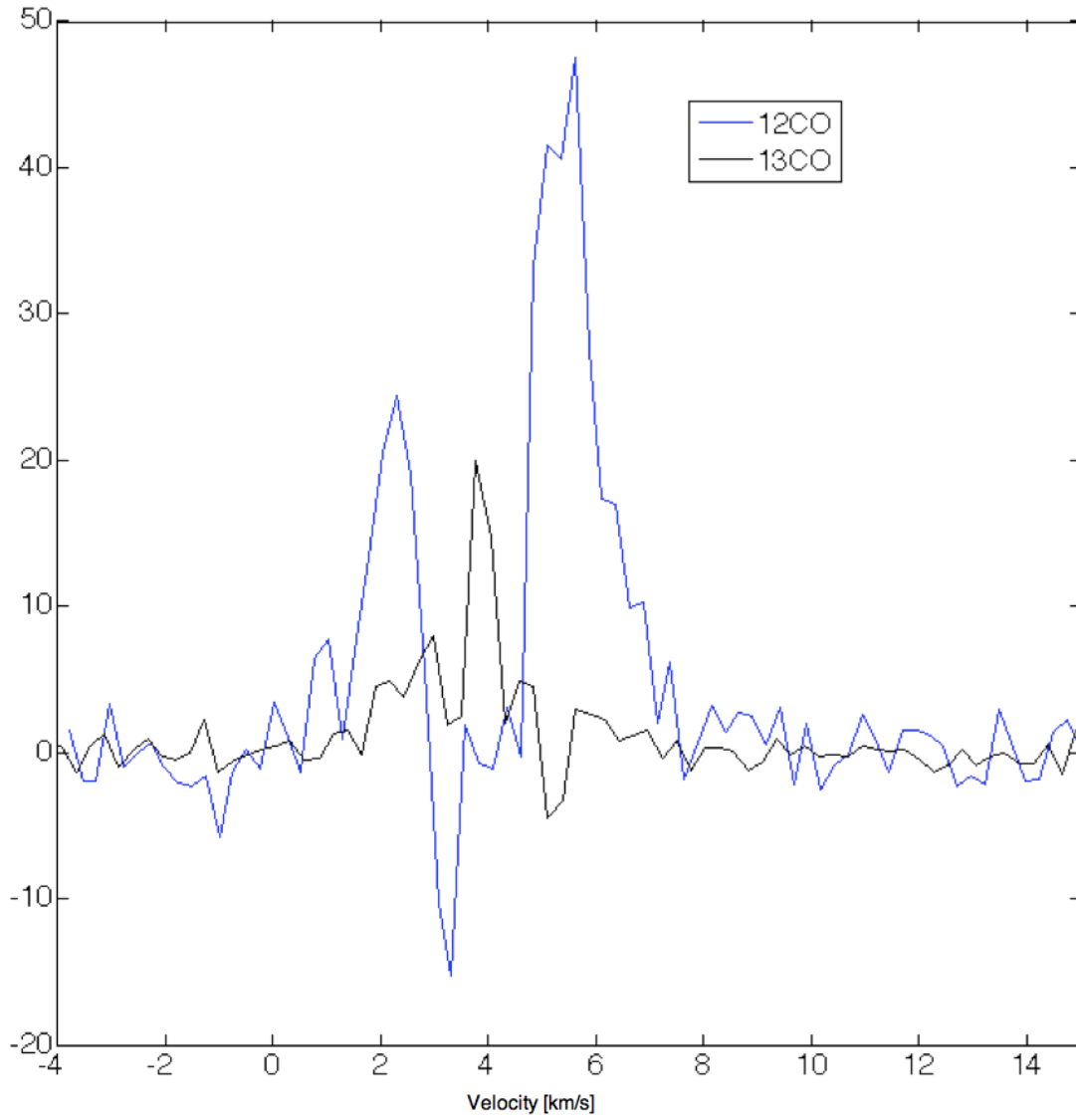


Fig. 34.— Spectra of ^{12}CO (blue) and ^{13}CO (black).

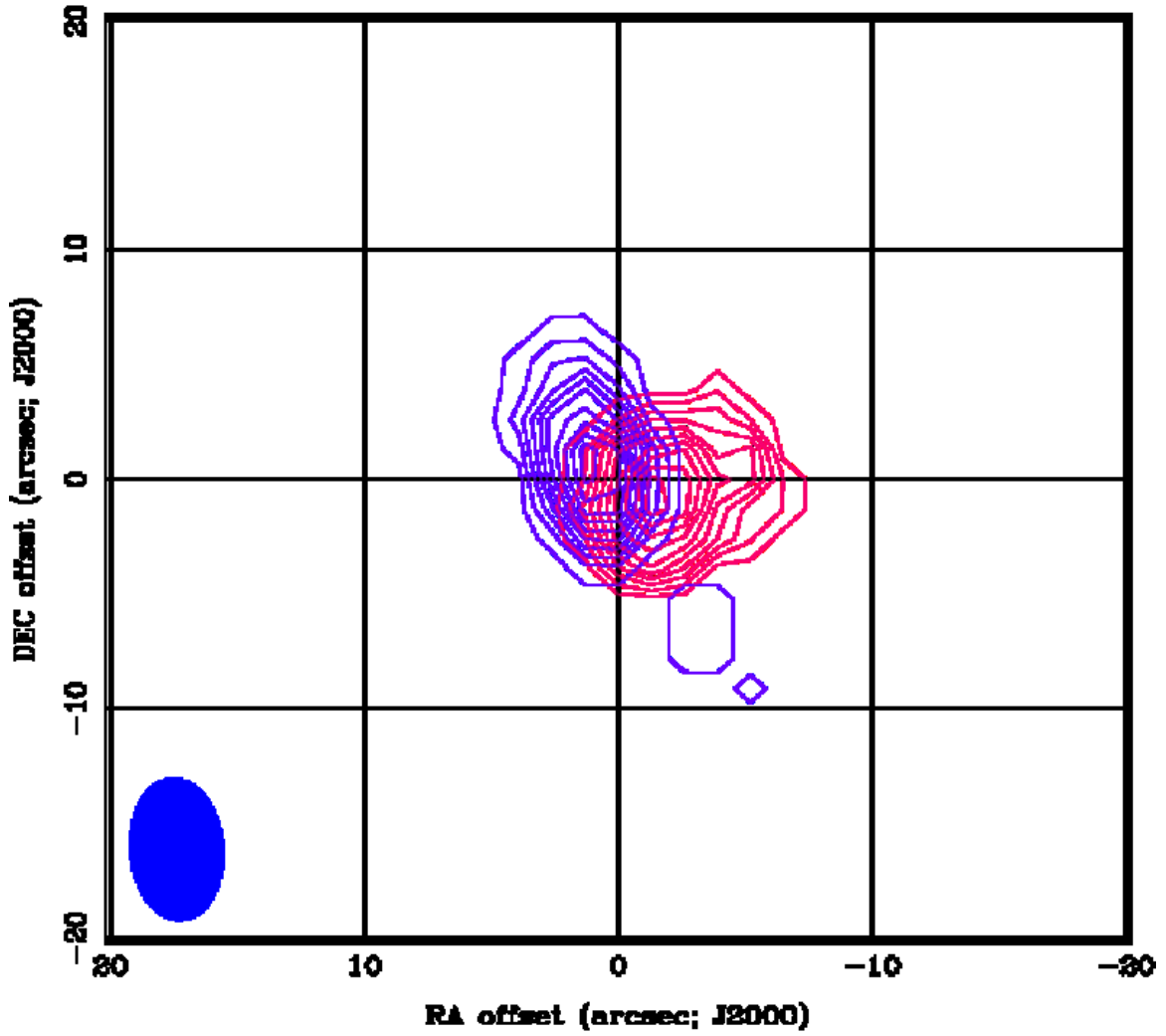


Fig. 35.— ^{12}CO blue emission (in red color) and red emission (in blue color). The integration ranges were selected to be the same as in Bontemps et al. (1996). These ranges correspond to the outflow identification.

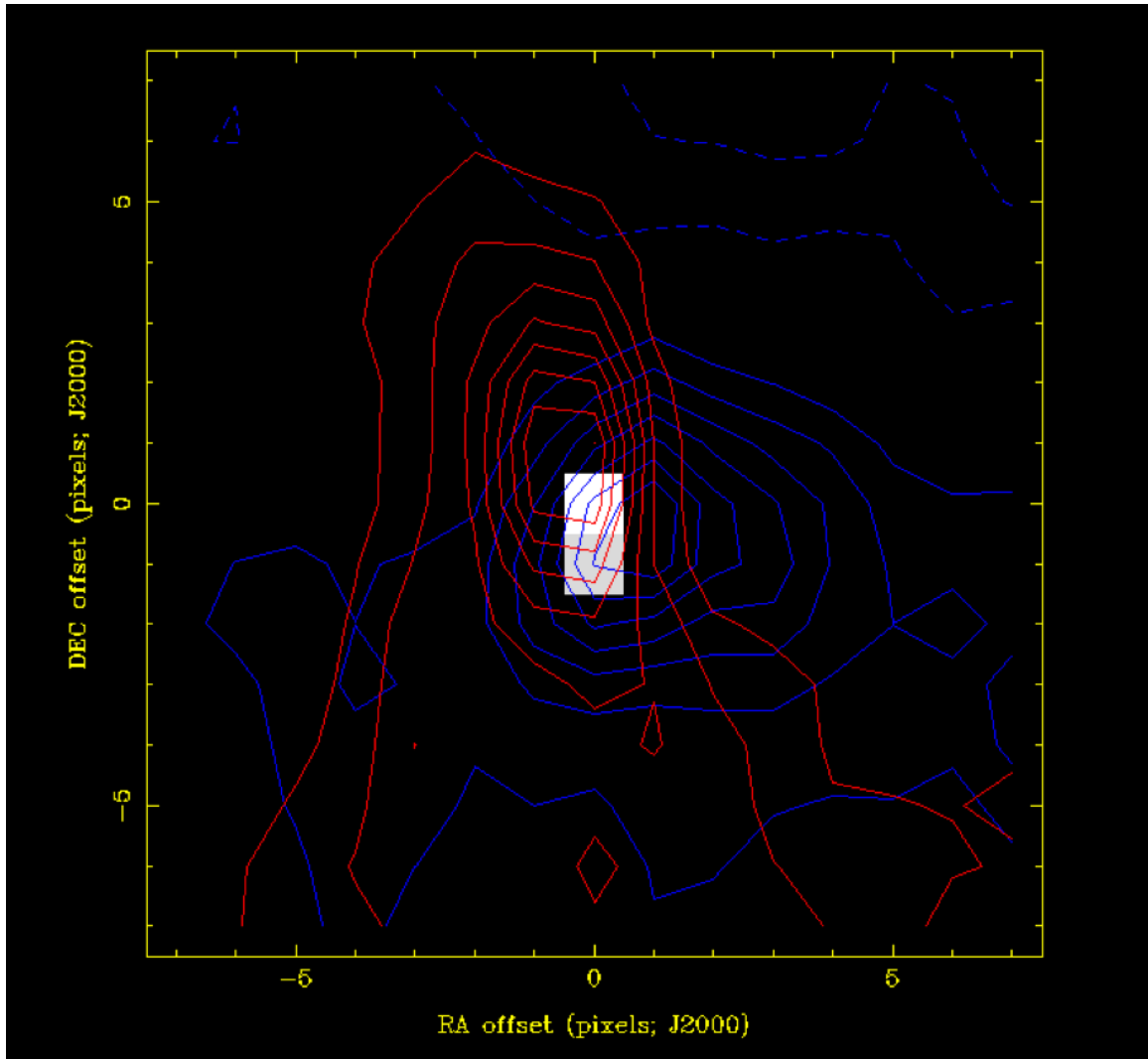


Fig. 36.— Intensity contours for the red and blue wings seen in Figure 34. In red is the emission at larger velocity than the source and the blue is the emission at less velocity than the source. In white is the position of the 3mm continuum.

10.4. Conclusions

The three molecules show a detection of the source. It is not clearly distinguished the disk as we expected. However, the geometry shows a slightly elongation consistent with the orientation of the disk previously identified in HCO^+ .

By examining the spectrum of the emission, we see no emission and an absorption feature in ^{12}CO spectrum near the LSR velocity of the source. This is likely due to the large optical depth at the rest frame velocity. The dense gas in the center absorbs the CO emission blocking the light from reaching us. In ^{13}CO and C^{18}O , we see a strong emission line in place of the absorption feature. Radiation from these molecules is emitted at higher densities, therefore the optical depth is less of an issue. As such, with these lines we are likely seeing more of the compact disk.

We do not see any clear visual disk or outflow in our maps. However, it is likely that we are tracing both, the disk and the base (since we only used a single pointing) of the outflow. This is more clearly seeing in the blue emission. More observations using a mosaic configuration are needed to identify better these two components.

We thank to the professors for all the help during this project. All the comments and directions were very constructive to understand our observations.

11. Detection of CO emission lines on a Submillimeter Galaxy at $z=5.2$

Jorge González

At high redshift, $z \sim 1 - 3$, dusty luminous infrared galaxies are thought to dominate the history of cosmic star formation. These massive starbursts might correspond to the formation phase of the luminous ellipticals seen in high-density regions today. They are therefore essential for understanding the main processes of galaxy formation and evolution.

When these galaxies are discovered with a high flux in submillimeter wavelengths they are called submillimeter galaxies (SMG). In the last years, two alternatives have arrived to explain the properties of these galaxies. The first option is that these galaxies are high-redshift versions of the Ultra-Luminous Infrared Galaxies (ULIRGS) found in the local universe. In this picture they are thus galaxies of moderate stellar mass ($< 10^{11} M_{\odot}$) involved in major mergers which produce a compact, short-lived starburst with a correspondingly extreme specific star-formation rate. The second explanation is that these galaxies simply represent the top end of the normal star-forming galaxy population at $z = 2 - 3$. In this scenario they are galaxies of high stellar mass ($> 10^{11} M_{\odot}$), which still have sufficiently large reserves or supplies of cool gas to produce very high levels of star formation, but in which this star formation is spatially-extended and is of a magnitude which is as expected given their large stellar masses.

11.1. Observations and Results

During the Herschel Lensing Survey (HLS) of massive galaxy clusters, an exceptionally bright source behind the $z = 0.22$ cluster Abell 773 was discovered, HLSJ091828.6+514223. The source appears to be a strongly lensed submillimeter galaxy (SMG) at $z = 5.2429$. This source is unusual compared to most other lensed sources discovered by Herschel so far, because of its higher submm flux (200 mJy at $500 \mu\text{m}$) and its high redshift. The dominant lens is a foreground $z = 0.63$ galaxy, not the cluster itself and the total magnification is estimated to be likely ~ 11 (Combes, F., et al., 2012).

Observations of the SMG were carried out with CARMA in the D configuration on June 2012. The correlator was setup to detect the CO(6-5) emission line at $z=5.2429$ at an observed frequency of 110.7615 GHz and the CO(5-4) emission line at an observed frequency of 92.3077 GHz. The correlation windows bands were setup to 500 MHz. The MIRIAD software package was used to calibrate and image the visibility data.

The observations presented here were made with 3.3 hours on source for the CO(6-5) emission line and 4.1 hours for CO(5-4). The measured spectra for the two lines are plotted in the Figures 37 and 38. A clear two peaks line emission is measured, a strong signal that this SMG is a result of a major merger of two galaxies. The parameter derived from the gaussian fits for the emission lines are in well agreement with the results from Combes et al. 2012. The integrated fluxes measured

for the lines are different of those presented in the literature due by the fact that we are measuring a continuum emission.

For the CO(6-5) line, the line with the higher noise level, a continuum level is measured of 3.3 ± 0.4 mJy/Beam, higher than the upper limit found in the previous observation of < 2 mJy/Beam. This high value for the continuum could be a result of the small number of channels around the lines used to measure the continuum and the high noise level. Using this continuum level, the integrated fluxes for the two peaks lines are 4.5 ± 0.9 and 0.7 ± 0.5 [Jy km/s] (Red and Blue respectively), lower than the results previously measured of 8.3 ± 0.6 and 1.9 ± 0.4 [Jy km/s].

For the CO(5-4) line, a continuum level is measured of 1.3 ± 0.2 mJy/Beam, in perfect agreement with the upper limit found in the previous observation (< 2 mJy/Beam). The better estimation of the continuum level at this frequency can be explained by the fact that the integration time was longer and the amount of channels used to measure it was higher. Using this continuum level, the integrated fluxes for the two peaks lines are 6.6 ± 0.9 and 2.0 ± 0.6 [Jy km/s] (Red and Blue respectively), lower than the results previously measured of 7.7 ± 0.5 and 1.0 ± 0.2 [Jy km/s] but almost within the error estimations.

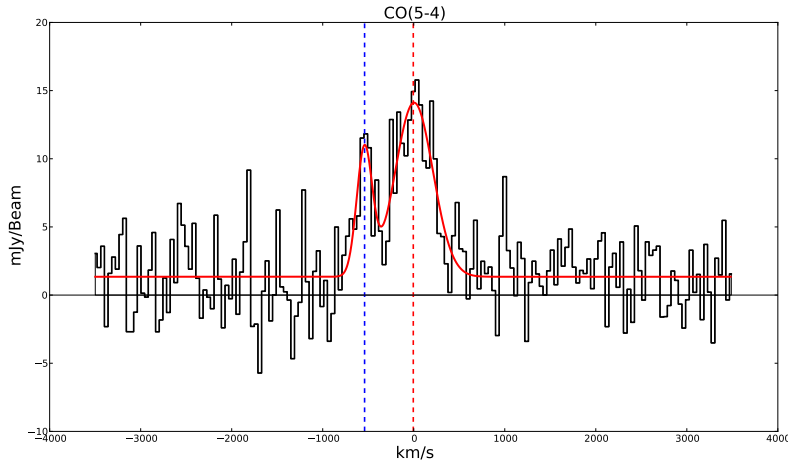


Fig. 37.— Extracted spectra of the submillimeter galaxy. The two peaks are seen in the emission line. The vertical dashed lines (red and blue), are the position measured for the peaks in (Combes et al., 2012). The velocity is with respect to the $z=5.2429$ measured in the red peak of the CO(6-5) line. The velocity resolution is of 40.1 [km/s]

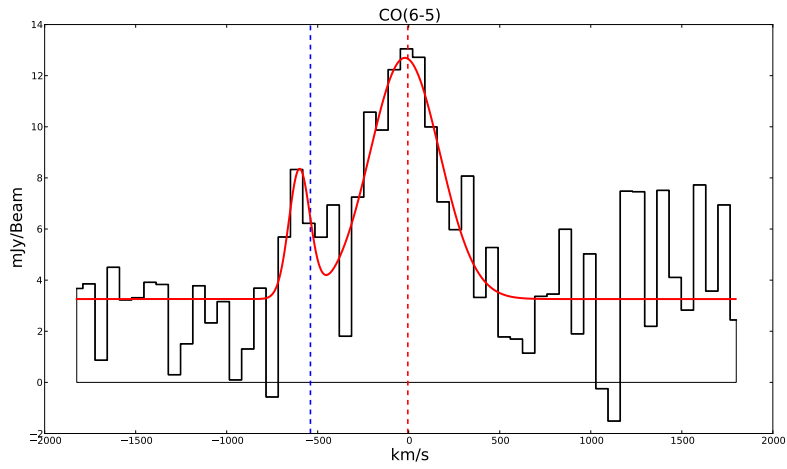


Fig. 38.— Extracted spectra of the submillimeter galaxy. The two peaks are seen in the emission line. The vertical dashed lines (red and blue), are the position measured for the peaks in (Combes et al., 2012). The velocity is with respect to the $z=5.2429$ measured in the red peak of the CO(6-5) line. The velocity resolution is of 60.3 [km/s]

12. Sunyaev-Zel’dovich Effect Observations Towards Four Massive Galaxy Clusters

Carmen Rodriguez Gonzalvez (California Institute of Technology),
Ashley Lindley (University of Alabama in Huntsville),
Yiran Wang (University of Illinois)

12.1. Introduction to Galaxy Clusters

Galaxy clusters are the largest gravitationally bound structures known in our Universe, and as such are powerful probes of the evolution of the universe. Clusters can contain up to thousands of galaxies within a diameter of a few megaparsecs, an intracluster medium of hot ionized gas and dark matter, and have a total mass on the order of $10^{14} - 10^{15} M_{\odot}$.

A powerful method for investigating our current cosmology is to observe the evolution of clusters over time, accomplished through analysis of cluster properties over a range of redshifts. One important property to examine is the cluster mass function, the number density of clusters of a given mass at a given redshift range (Vikhlinin et al., 2009). Studies of the cluster mass function are currently a popular method for obtaining cosmological constraints (Borgani et al. 2001, Vikhlinin et al. 2009, Mantz et al. 2010) such as the normalization of the power spectrum, σ_8 , the equation of the state of dark energy, $w(z)$, and the cosmological density of matter, Ω_M .

Another advantage of researching clusters of galaxies is that they are detectable over a wide range of wavelengths. They were originally detected via optical observations of stellar matter, but have also been analyzed utilizing X-ray and microwave (radio) instruments due to the substantial amounts of hot ionized gas within the cluster (see Figure 39). Mostly of interest to us as students at the CARMA summer school is the fact that the hot gas within clusters is observable in microwave wavelengths through its effects on the Cosmic Microwave Background (CMB) radiation. These CMB distortions, known as the Sunyaev-Zel’dovich (SZ) effect (see Section 12.2 for further details), were predicted in the early 1970s (Sunyaev & Zel’dovich 1970, 1972). Within the past couple of decades the SZ effect has been successfully detected for hundreds of known clusters (Birkinshaw et al. 1999; Carlstrom et al. 2002) and currently several surveys, such as SPT, ACT, and Planck are discovering new clusters via SZ effect observations (SPT - Williamson et al. 2011, ACT - Marriage et al. 2010, Planck Collaboration et al. 2011) . Excitingly, the SZ effect has been used to calculate cluster masses, and thus can be used together with cluster redshift information to determine the cluster mass function to place constraints on cosmology in the future. The potential of these surveys to determine cosmology relies on precise characterization of how the observable, the SZ signal, translates into a physical quantity, the cluster mass. For example, determining the dark energy equation of state within 5% requires systematic biases on the cluster mass estimators to be controlled to better than the 10% level (Mohr et al. 2003).

12.2. The Sunyaev-Zel’dovich Effect and Radio Observations

12.2.1. The Sunyaev-Zel’dovich Effect

The Sunyaev-Zel’dovich (SZ) effect is a shift in the spectrum of the cosmic microwave background (CMB) radiation (see Figure 40), caused by inverse Compton scattering of CMB photons by energetic electrons in galaxy clusters (Sunyaev and Zel’dovich 1970, 1972). The observable associated with the SZ effect is called the Compton y -parameter and is proportional to the pressure of the intra-cluster medium integrated along the line of sight (Sunyaev & Zel’dovich 1970, 1972).

The integral of the Compton y -parameter over the solid angle subtended by the cluster, Y , is a direct measure of the internal thermal energy of the gas in the cluster, and, as such, it is expected to be a good proxy for cluster total mass (Bonamente et al. 2008; Birkinshaw and Lancaster 2008).

12.2.2. Radio Interferometry

Galaxy clusters are typically on the order of a megaparsec in size. For the cosmology being assumed for this project, a megaparsec cluster will subtend an area of at least an arcminute for any given redshift, with lower redshift clusters projecting over a larger area. Radio interferometry is well suited to observe clusters over these large angular scales due an interferometer’s ability to simultaneously collect measurements from a cluster over a range of spatial frequencies (Carlstrom et al., 2002).

As we have learned this week, an interferometer measures the time averaged correlation of signals received by a pair of telescopes (see Figure reff-config), incorporating a time offset between the first and second antennas detecting the signal, with the output of the interferometer, referred to as visibilities, being the complex Fourier transform of the radio signal received. The sensitivity in terms of the angular resolution (θ) of an interferometric array is directly related to the wavelength of the observation (λ) and the physical distance between any two antennas in the array, called a baseline (B)

$$\theta = 1.22 \times \frac{\lambda}{B}. \tag{1}$$

This equation is known as the Rayleigh Criterion and defines the minimum resolvable detail of the interferometer. This equation can also be used to determine the field of view of a single antenna, by replacing B with D , the diameter of the antenna. These two properties of radio interferometry, angular resolution and field of view, dictate the size of objects that can be observed for desired angular resolutions.

The Combined Array for Research in Millimeter-wave Astronomy (CARMA) is a radio telescopic array that specializes in studying the cold universe through radio imaging of molecules, dust, and emissions from the CMB (www.mmarray.org), exactly what is needed for detecting the SZ effect in

galaxy clusters.

The Sunyaev-Zel’dovich Array (SZA), an interferometric radio subarray of CARMA consisting of eight 3.5-meter antennas equipped with centimeter- (26-36 GHz) and millimeter-wavelength (80-115 GHz) receivers, has been designed for accurate measurement of the SZ effect in clusters of galaxies at 30 GHz (Muchovej et al. 2007; Mroczkowski 2009; Culverhouse 2010). Six of the SZA antennas are arranged in close proximity to each other, creating short baselines, with separations between any two antennas ranging from 4.5 to 11.5 meters allowing for imaging the SZ decrement in a cluster at an angular resolution of $\sim 2'$. The remaining two antennas are positioned outside the inner cluster of antennas with distances between any two telescopes being up to 65 meters. These outlying antennas, which create long baselines, allow for simultaneous detection of potential contaminating radio sources with an angular resolution of $\sim 0.3'$ (Muchovej et al, 2007) (see Figure 41).

13. Motivation for Project

Since we initially had the SZA all to ourselves for observing, as we were the only group to express interest in observing at only the 1 cm wavelength, we began by observing a cluster that was expected to be one of the most massive clusters known at a high redshift, and then moved on to utilize the SZA antennas as much as possible, ultimately observing and analyzing four known massive clusters that had previously been unobserved by CARMA. Cluster details, motivation and goals for each cluster selected for analysis are as follows:

Cluster	RA	Dec	Redshift
MACSJ1115.2+5320	11:15:15.6	53:20:03.3	0.44
Abell 2142	15:58:20.9	27:13:44.2	0.09
MACSJ0717.5+3745	07:17:31.7	37:45:18.2	0.55
MACSJ0011.7-1523	00:11:43.0	-15:23:20.8	0.36

Table 3: Cluster details from the *Chandra* ACCEPT database (Cavagnolo et al. 2009).

MACSJ1115.2+5320

MACS J1115.2+5320 was the first cluster we observed primarily because it is possibly one of the most massive galaxy clusters known. This highly disturbed cluster exhibits a relatively small separation feature between the two brightest cluster galaxies, adding to its observational interest especially at higher resolutions. With more observing time allowed for our project, we observed MACS J1115.2+5320 at 90GHz hoping for a strong enough detection that would allow for investigation of the cluster substructure (Mann & Ebeling, 2012).

Abell 2142

Abell 2142 was the second cluster we decided to observe. We selected this cluster for observation because it is another disturbed, merging cluster that we expected to show an interesting shape in the radio mapping. This cluster differed from the other clusters in our project in that it was the lowest redshift cluster we observed.

MACSJ0717.5+3745

MACS J0717.5+3745, the next cluster we observed, is excitingly the most disturbed massive cluster known at redshift greater than 0.5. It has been described as being a possible triple cluster merger (Ma & Ebeling, 2011). We were interested in revealing the radio morphology of this cluster.

MACSJ0011.7-1523

MACS J0011.7-1523, the final cluster we observed, is in complete contrast to the previous three clusters providing us with an example of a relaxed cluster. A relaxed cluster is thought to be a morphological opposite to a disturbed cluster.

14. Reduction of SZE Observations

All clusters were observed using the SZA subarray using the 30 GHz (1 cm) receivers, with MACSJ1115 being also observed using the 90 GHz (3mm) receivers. Each cluster was observed for ~ 3.5 to ~ 10 hours, usually through transit. These tracks alternated between observing calibration sources and observing the science target at intervals of 3 minutes and 15 minutes respectively.

The SZA data for these clusters were reduced by all three of us, using the Miriad reduction software. During this reduction process we converted raw data from the antenna’s correlators to a calibrated set of visibilities in the Fourier u-v plane which were then mapped to form an image of the source. This process allowed us to interactively flag erroneous data points that are typically caused by mechanical antenna issues, shadowing of an antenna by another, bad weather conditions and occasionally by other origins.

Once the raw data had been satisfactorily reduced into acceptable visibilities, the data was then analyzed using *Difmap*, a program that has been specifically developed for imaging data from radio interferometers (<ftp://ftp.astro.caltech.edu/pub/difmap/difmap.html>). *Difmap* has preset commands that allow for viewing several aspects of the visibility data. For a typical analysis, we first looked at the *radplot* for each cluster to view the amplitude versus the u-v radius to make sure the signal-to-noise level is appropriate for further analysis without additional data flagging, then we analyzed the long baseline data to identify possible point sources contamination in the observation

area, and then finally we viewed the short baseline data to analyze the cluster decrement caused by the SZ effect. The spatial differentiation of the short and long baselines in interferometry allows the emission from radio point sources to be separated from the SZE emission, usually allowing for successful decontamination of the decrement detection within *Difmap* (Carlstrom et al., 2002).

14.0.3. Results

Here we report our results from observing and analyzing the data for each of the four clusters. Observation details are presented in Table 4 and a brief explanation of analysis follows.

Cluster	Integration Time (hr)	Noise Level (mJy/beam)	Peak Decrement (mJy)	Signal to Noise
MACSJ1115.2+5320	3.5	0.543	-5.77	$\sim 10.6 \sigma$
Abell 2142	10	0.493	-3.28	$\sim 6.7 \sigma$
MACSJ0717.5+3745	10	0.36	-7.32	$\sim 20 \sigma$
MACSJ0011.7-1523	5	0.535	-3.77	$\sim 7 \sigma$

Table 4: Observation results for the four clusters analyzed at 30 GHz.

MACSJ1115.2+5320

Observations of MACSJ1115.2+5320 at 30 GHz resulted in a very strong SZ effect detection, which can be seen in the right panel of Figure 43 as a blue blob in the center of the radio mapping, indicating a negative radio intensity at the location of the galaxy cluster. This map of the SZ decrement was produced after inspecting the long baseline data (seen in the left panel of Figure 43) which show that there are no radio bright point sources in the field of view. We observed this cluster at 90 GHz as well with the hopes of resolving substructure, but with no obvious detection of the cluster at all after a ~ 4 hour observation we realized that the likelihood of having enough observation time to gain a high enough signal to noise ratio was low, thus we prioritized our time to observe other clusters of interest.

Abell 2142

Observations of Abell 2142 at 30 GHz produced a resolved, high SNR SZ detection. The extensions of the decrement in several directions are indicative of the complex dynamical state of Abell 2142 (See Figure 44c). The field of view observed for this cluster did contain one point source which was detected (see Figure 44a), located in the long baseline data and then removed from the short baseline data set using a CLEAN algorithm within *Difmap* (see Figure f-Abell2142b).

MACSJ0717.5+3745

Observations of MACSJ0717.5+3745 at 30 GHz resulted in a very strong SZ effect detection. The shape of the SZ decrement is more regular than we had expected since this cluster is expected to be one of the most disturbed clusters at a higher redshift. Upon mapping the long baseline data a weak radio point source was detected in the upper left side of the image (see Figure 45a). We experimented with not removing the point source and then removing the point source and mapping the short baseline data in both cases in order to show the importance of point source subtraction for accurate decrement mapping (see Figure 45b and 45c, respectively).

MACSJ0011.7-1523

Observations of MACSJ0011.7-1523 at 30 GHz resulted in a sufficient SZ effect detection with no point source contamination. This detection was expected to reveal a circular decrement mapping typical of relaxed clusters, but instead exhibited properties more expected with a slightly disturbed cluster with a visible elongation in the positive relative declination direction.

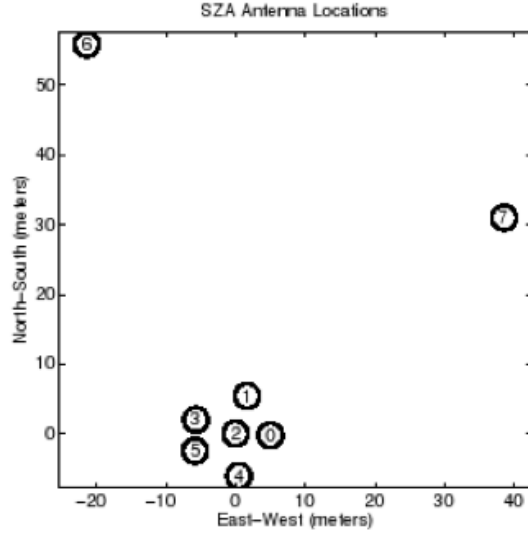


Fig. 41.— An example of a Sunyaev-Zel’dovich Array configuration, with antennas 0-5 packed closely together and antennas 6 & 7 located at outlying positions (Muchovej et al, 2007).

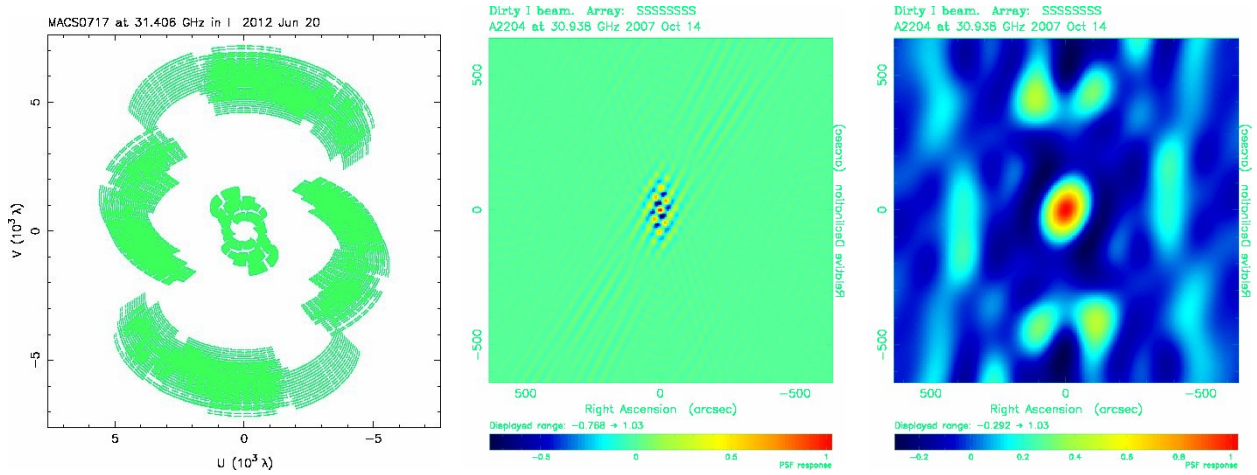


Fig. 42.— Plots of a) the tracks taken for MACSJ0717.5+3745 on the u - v plane, b) an example of the synthesized beam pattern for long baseline data indicating a point source signature, and c) an example of the synthesized beam pattern for short baseline data indicating a cluster decrement signature, or a point-spread function.

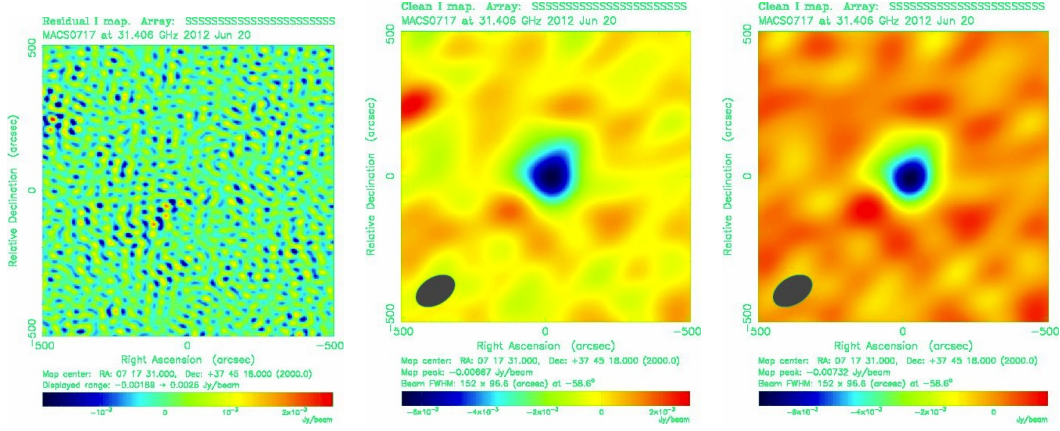


Fig. 45.— *Difmap*-generated images of MACSJ0717.5+3745: a) long baseline mapping with one identified off-center point source near the top left, further investigation will be required to assess whether there are further sources in the field, b) short baseline mapping prior to point source ‘cleaning,’ showing how the SZ decrement can be affected by a point source contamination, c) SZ cluster decrement from the short baseline mapping once the brightest point source has been cleaned using the long baseline mapping. The synthesized beams are shown in the bottom left corners.

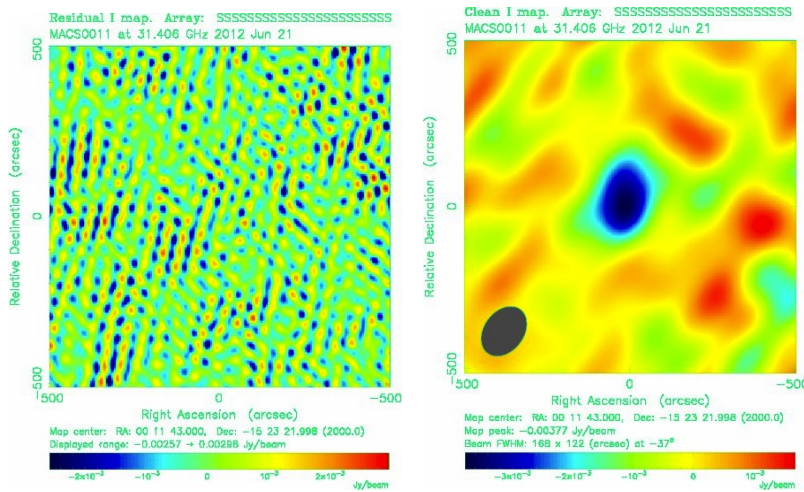


Fig. 46.— *Difmap*-generated images of MACSJ0011.7-1523: a) long baseline mapping with no point source detection resulting in a noisy map, b) SZ cluster decrement from the short baseline mapping. The synthesized beam is shown in the bottom left corner.

15. Spectral Line Observations of NGC 1068

Matthew Rickert (Northwestern University)

NGC 1068 (also known as Messier 77) is a type 2 Seyfert barred spiral galaxy, located at RA: 2h 42' 40" Dec: 0° 0' 48" approximately 14.4 Mpc away (Rand & Wallin 2004) with a redshift of 0.013 and a radio velocity of the local standard of rest (VLSR) of 1137 ± 3 km/s (Paturel et al. 2003). It is known to have an active galactic nucleus (AGN) (likely a black hole) with 2 radio jets (one red shifted and one blue shifted, see Figure 48) (Cecil et al. 2002).

During this project, NGC 1068 was observed for 6 hours with 7 pointings, with spectral windows about: 110.2 GHz, with a bandwidth of 250 MHz to measure CH₃CN, 108.9 GHz with a bandwidth of 125 MHz to measure 13CO, 97.9 GHz with a bandwidth of 125 MHz to measure CS, and 96.7 GHz with a bandwidth of 62 MHz to measure CH₃OH, as well as four 500 MHz wide windows that were used to measure the continuum (a contour map of the continuum is shown in Figure 49). Uranus was observed as a flux calibrator, with 3C84 as a bandpass calibrator and 0224+069 as a gain calibrator. Methanol is known to be a tracer of shocks in the Galaxy. CS is a well known dense gas tracer, and 13CO is also known to be a gas tracer and involved in starburst activity. While there have previously been observations of 13CO (Helfer & Blitz 1995), CH₃OH (García-Burillo et al. 2010), CS (Wang et al. 2011), and CH₃CN from NGC 1068, the CH₃CN detection does not appear to have been extensively studied, and it is therefore worth following up the previous detection with CARMA observations (Aladro et al. 2012). Following the observations, the data was analyzed using the CARMA MIRIAD version 4.3.4 software package. At the time that this memo was submitted, only continuum maps (Figures 49 & 50), and maps and spectral lines of 13CO (Figures 51- 53) and CS (Figures 54 & 55). Analysis is still ongoing, particularly for CH₃CN and CH₃OH.



Fig. 47.— An optical image taken by the Jacobus Kaptevn Telescope in which the spiral and bar structures are clearly visible. (Credit:ING Archive and Nik Szymanek)



Fig. 48.— An artist's rendition of NGC 1068 indicating the AGN at the center, and the corresponding blue/red shifted jets. (Credit: Gemini Observatory)

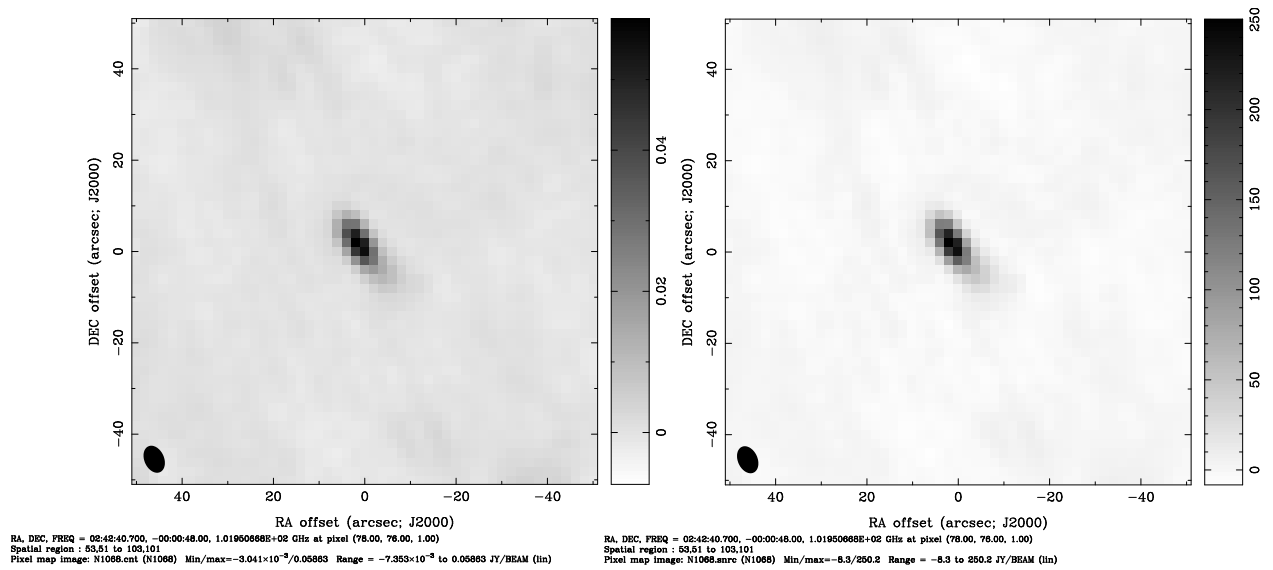


Fig. 49.— Left: Map of the continuum of NGC 1068. Right Map of the noise of the continuum of NGC 1068.

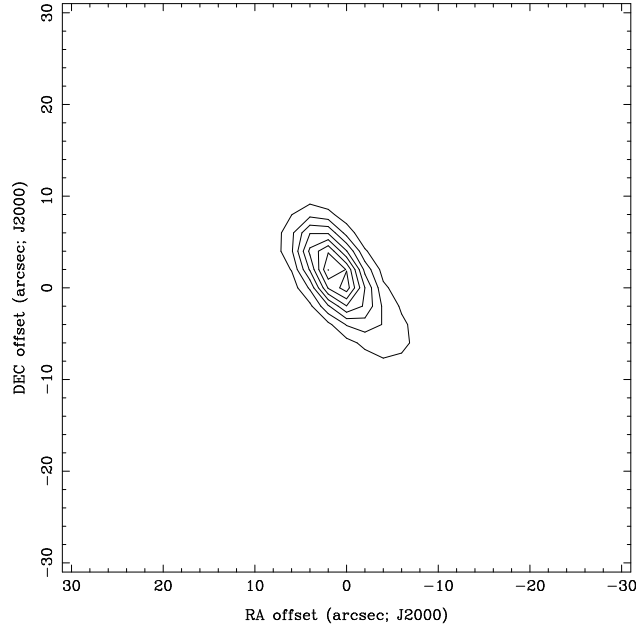


Fig. 50.— A continuum contour map of NGC 1068.

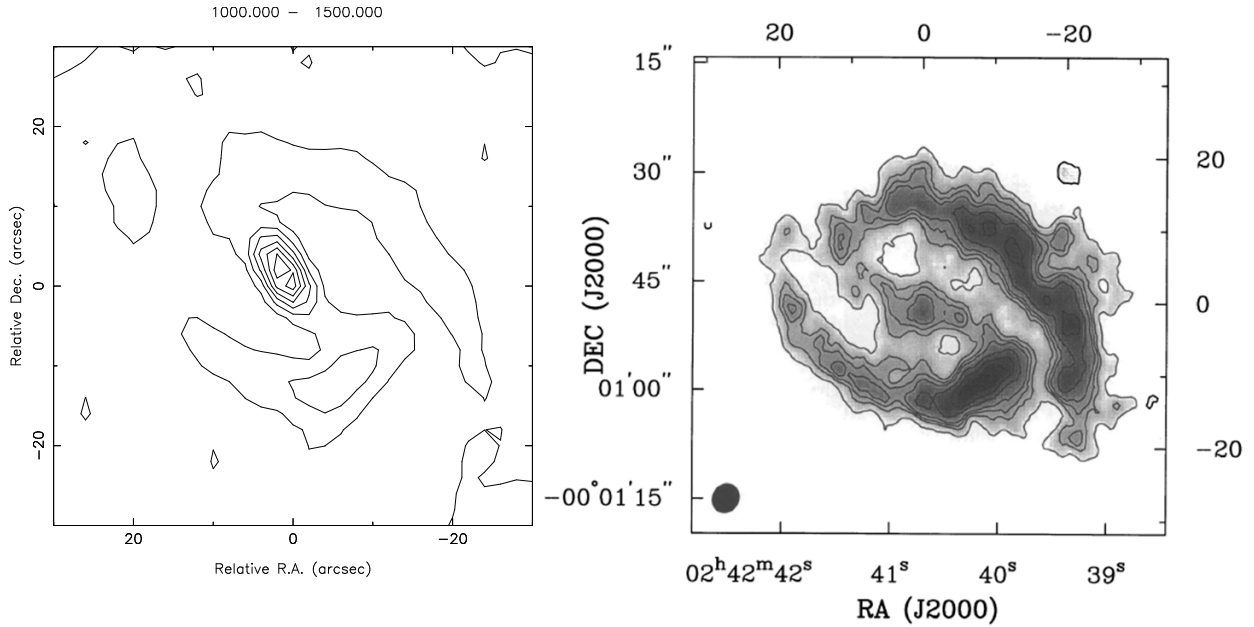


Fig. 51.— Left: Moment0 Map (which is a map of the total integrated intensity) for 1000-1500 km/s which corresponds to ^{13}CO (noting that NGC 1068 has a VLSR of 1137 km/s). The contours correspond to: 8.3, 16, 25, 33, 41, 50 mJy, with a maximum of 55 mJy, a minimum of 1 mJy, and an RMS of 8 mJy. Right: A ^{13}CO integrated intensity map previously observed by Berkeley-Illinois-Maryland Association (BIMA) (Helfer & Blitz 1995). As expected, both maps agree with each other.

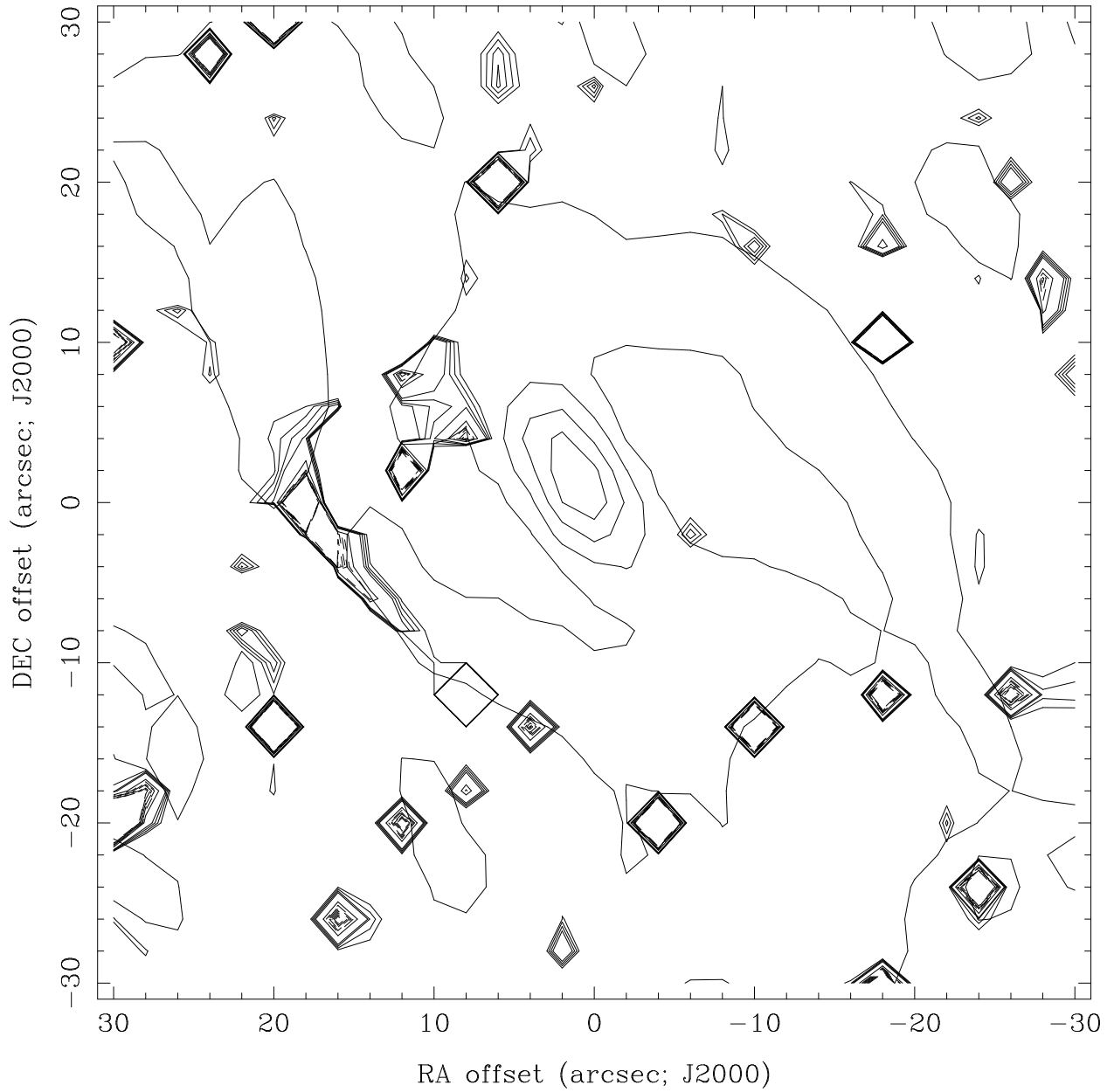


Fig. 52.— Moment0 Map of ^{13}CO , with a Moment1 map overlaid on top of it. The Moment1 Map shows the integrated velocities. There does not appear to be any correlation between the two maps. The contour levels for the Moment0 map are -0.07% to 0.09% in increments of 0.01 . Very few contours would appear for values higher than these. Thus, the lack of correlation between the two maps, as well as the small values for the Moment1 maps, appears to indicate that the ^{13}CO emission at the center of NGC 1068 has no appreciable velocity along our line of sight, and is therefore moving almost exclusively perpendicular to our line of sight.

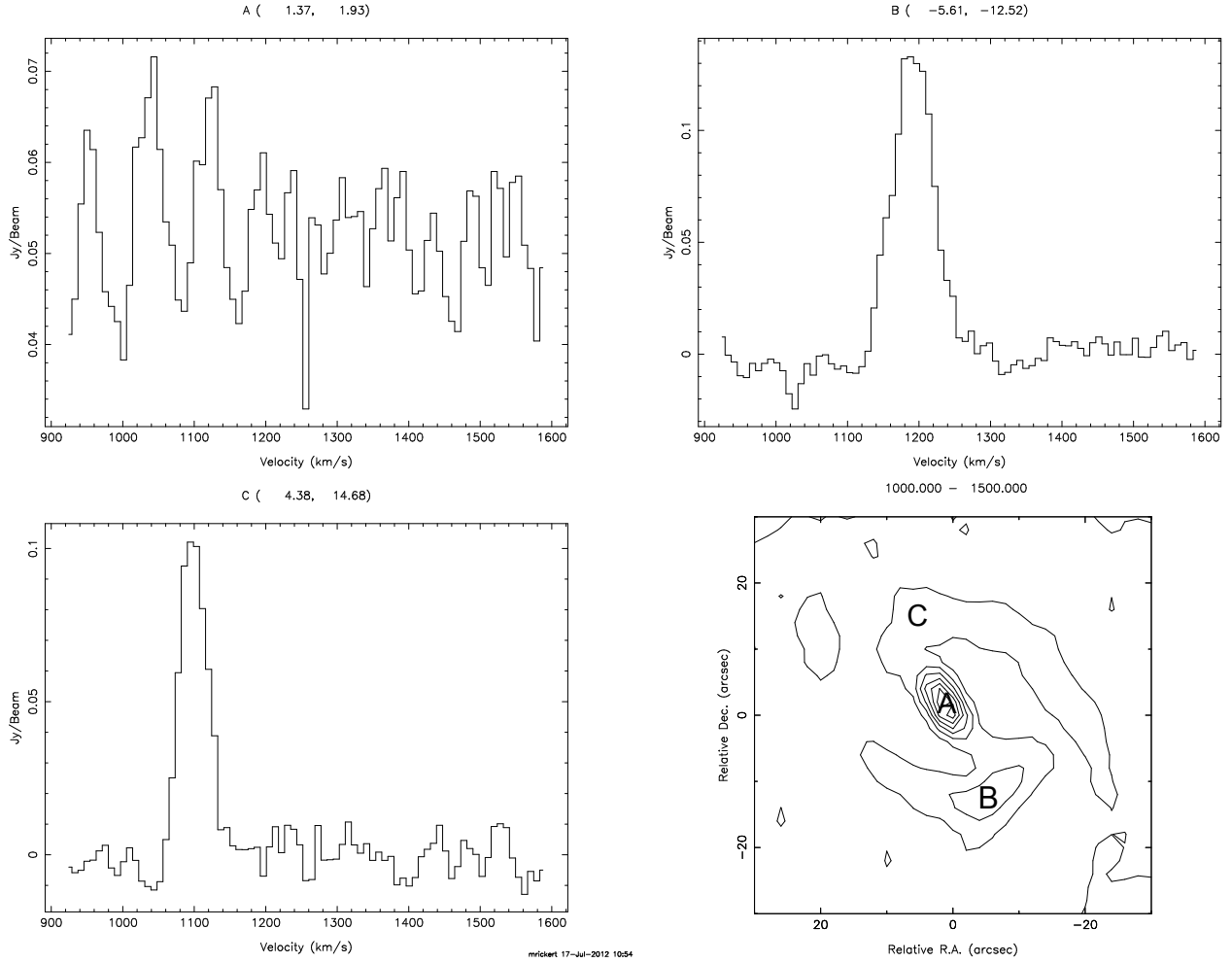


Fig. 53.— Upper left: Spectrum corresponding to point A in the lower right contour map. This part appears to be dominated by continuum by how there is no apparent emission peak, and how the contours in the center of the lower right map match with the continuum contours in Figure 50. Upper right and lower left: Spectra corresponding to 13CO located at points B and C respectively in the lower right map. Note that there is a velocity shift between the two spectra, and that the spectral line at point B is broader than at point A. Lower right: Contour map of 13CO depicting the locations of where the different spectra were taken.

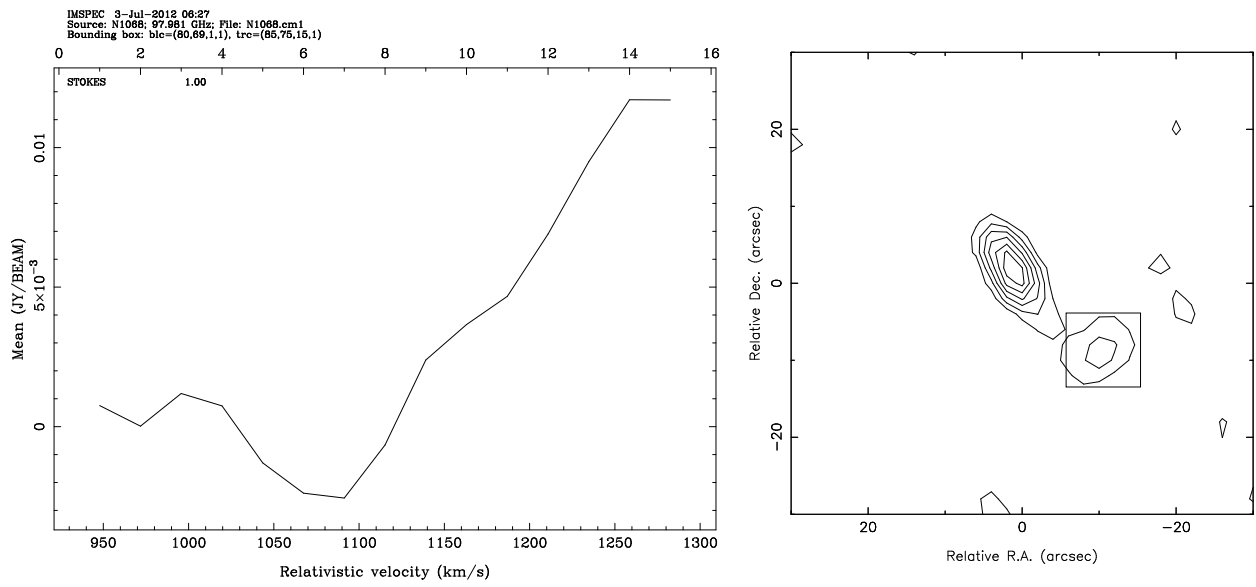


Fig. 54.— Left: Spectra of CS averaged over the area inside the rectangle in the Contour map. Note that part of the spectra was cut off due to the bandwidth. Right: Moment0 Map averaged over 1200-1400 km/s, which includes the CS transition. The contour levels are 9.4, 19, 28, 38, 47, and 56 mJy, with a maximum of 63 mJy, a minimum of 0, and an rms of 7 mJy. Note that there is still continuum in this map, with the central feature matching up to that found in Figure 50, yet there is still a very clear CS detection to the lower right of the continuum source.

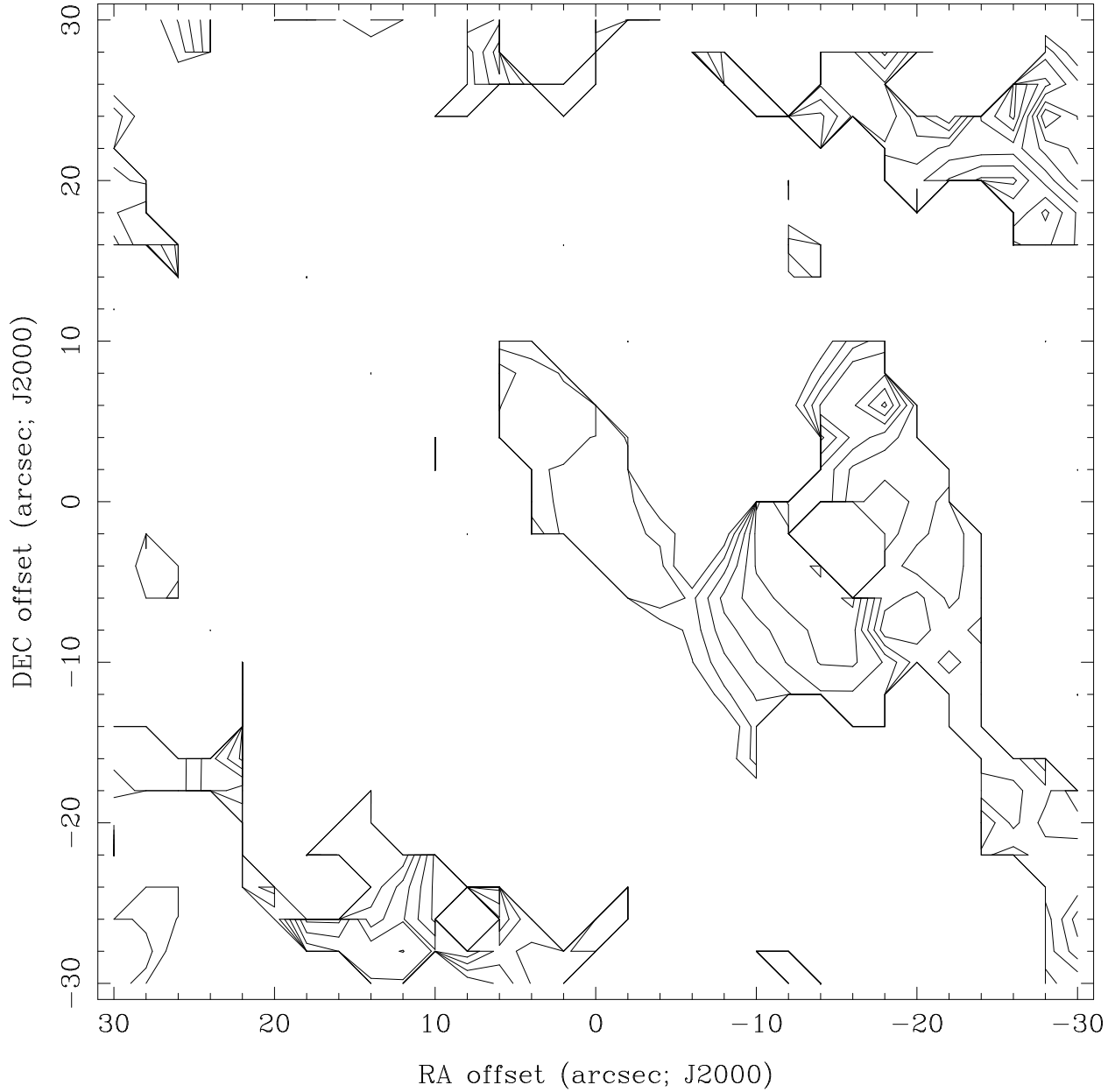


Fig. 55.— Moment1 Map averaged over 1200 to 1400 km/s which includes the CS transition. By comparing to Figure 54 it can be seen that the continuum aspect located at the center of the figure, is moving with a distinctly different velocity than the CS detection in the lower right section, possible indicating that the two components are not linked and are moving separately.

16. The Winds of IK Tau

Kyle B. Westfall

Kapteyn Astronomical Institute
University of Groningen, NL

16.1. Motivation

Stars on the asymptotic giant branch (AGB) are in the “death throws” of their life cycle, shoving off tenuous outer layers that are later illuminated by the white-hot cinder of the remnant core to produce the brilliance of planetary nebulae. Although one may write such a colorful description of this process rather easily, a detailed description of the physical processes involved, and indeed the observed variety in the results of these processes, is understandably challenging. Even so, not only will research into these processes prove edifying in terms of our detailed understanding of *stellar* evolution, but the degree to which AGB stars affect the luminosity evolution of *galaxies* is also of fundamental relevance.

It is commonly assumed that the near-infrared emission of galaxies provides a reasonable view of the stellar mass distribution. Although reasonable for the old stellar populations present in “red and dead” elliptical galaxies, this assumption has been challenged in recent years for late-type (spiral and irregular) galaxies having had recent (< 2 Gyr) star-formation activity because of the complicated influence of AGB stars on the integrated luminosity (see, e.g., Zibetti et al. 2012). Of particular relevance to this problem are the so-called thermally pulsing AGB (TP-AGB) stars. Owing to their peak luminosities (> 2 magnitudes above the tip of the red giant branch), intermediate-age stars with masses between $2-10 M_{\odot}$ can greatly affect total stellar-mass estimates of galaxies based on stellar-population-synthesis (SPS) modeling (Maraston 2005). This is despite their marginal contribution to the actual mass and the brevity of this phase of stellar evolution ($1-2$ Myr). Indeed, depending on the physics applied to these phases in SPS models, age and stellar-mass estimates can vary by factors of two or more (Conroy et al. 2009).

Among the many complicating factors in tracing the temperature and luminosity evolution of TP-AGB stars is a basic understanding of the mass-loss process (rate and driving mechanism) and chemical composition of the circumstellar envelopes (CSEs). The stellar wind is thought to be radiatively driven where dust formed in the upper layers of the stellar atmosphere provides the source of opacity (e.g., Höfner 2008). Thus, measurements of both the dynamical and chemical properties of CSEs can yield important constraints on the facility of this mechanism in producing the wind, thereby constraining the physical processes at work near the stellar photosphere. With this in mind, I chose to use CARMA to observe a single AGB star in as many molecular lines as possible given the allotted time (Section 16.2), yielding both a measure of the chemical composition and a probe of the dynamical structure of the star.

I chose to observe the well-studied M-type (oxygen-rich) Mira variable IK Tau, which lies at a distance of 250 pc and has a local-standard-of-rest velocity of $V_{\text{LSR}} \sim 35 \text{ km s}^{-1}$. This AGB star has a pulsation period of 500 days (González Delgado et al. 2003) and a measured mass-loss rate of $10^{-5} M_{\odot} \text{ yr}^{-1}$ (Ramstedt et al. 2008). Along with a known aspherical outflow, it is known to have a strong SiO maser. Observations of the ^{12}CO ($J = 1 \rightarrow 0$) and ^{12}CO ($J = 2 \rightarrow 1$) transitions were obtained by Castro-Carrizo et al. (2010) using the Plateau de Bure Interferometer and the IRAM 30m as part of the COSAS program. For reference, the synthesized beam of these observations was $4''$ with velocity channels of $\sim 1 \text{ km s}^{-1}$.

16.2. Observations and Reduction

I observed IK Tau, at $(\alpha, \beta) = (03:53:28.87, +11:24:21.7)$ J2000, using two different frequency tunings. The total observing time, including overheads, for the first and second tracks were ~ 3.5 hours and ~ 2.6 hours, respectively. The weather conditions were excellent throughout the observations. For both tunings, two 500 MHz windows were used for continuum measurements and the other six windows were set to 31 MHz width for spectral-line observations. All windows were set to 2-bit mode to provide high spectral resolution; however, in the end, this resolution was unnecessary. For the first setup, I aimed to observe lines *not* observed by the COSAS program, and chose lines near the HCN line at 88.6 GHz. For the second setup, I aimed to re-observe the ^{12}CO observations from the COSAS program, but at slightly better spectral and spatial resolution. In all, I placed spectral windows at frequencies appropriate for observing SiO (86.2 GHz), HCN, HCO+ (89.2 GHz), HCCCCCN (95.9 GHz), H₂O (96.3 GHz), and CS (98.0 GHz) in the first setup; windows were set to observe HCCCN (109.2 GHz), SO (109.3 GHz), C¹⁸O (109.8 GHz), ¹³CO (110.2 GHz), CN (113.5 GHz), and ^{12}CO (115.3 GHz) in the second setup. The primary beam size at these frequencies for the 10m dishes was sufficient to observe the entire CSE in one pointing; however, the data indicate that the full extent of the ^{12}CO emission in the envelope may have been resolved out by the interferometer.

Standard *MIRIAD* routines were used to perform the reduction; a script provided by John Carpenter proved invaluable. Because the star is expected to be rather bright, 3C84 was chosen as the passband calibrator to ensure a robust calibration. The planet Uranus was used to perform flux calibration, and the source 0339-017 was used as the gain calibrator. Standard fluxes from the *MIRIAD* flux catalog were used for these sources during the data reduction. The strength of the SiO maser would provide for a robust self calibration of the data; however, the standard reduction techniques were sufficient for this contribution.

The observations of the spectral lines were taken with very high spectral resolution ($\sim 0.2 \text{ km s}^{-1}$) by selecting 2-bit mode for each 31 MHz window. This was done because the lines were expected to be very strong, and such a high resolution may have revealed interesting detail in the structure of the CSE of IK Tau. However, in creating data cubes based on the observations, I found that this high resolution was unnecessary. Thus, when producing images based on the visibility data,

all lines were resampled to have velocity channels of 1.6 km s^{-1} . The major axis of the synthesized beam size ranges from $3''.4 - 3''.9$ with minor-to-major axis ratios from $0.6 - 0.9$.

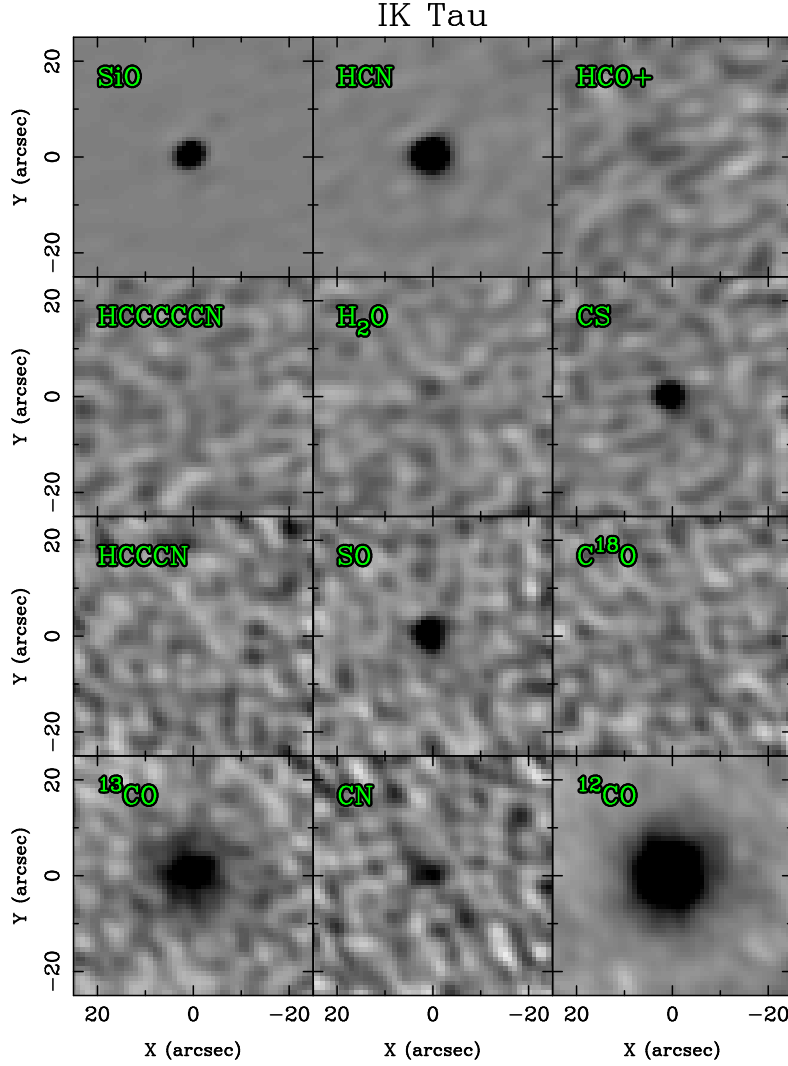


Fig. 56.— Detection maps for the twelve targeted line observations of IK Tau; the targeted molecular compound is provided in the upper left corner of each panel. Each image is $50'' \times 50''$ and is the sum of all flux within $15 \text{ km s}^{-1} \leq V_{\text{LSR}} \leq 55 \text{ km s}^{-1}$.

Figure 56 shows the reconstructed images for each line observed. The signal in the detection of each line includes the sum of all flux within the velocity range $15 \text{ km s}^{-1} \leq V_{\text{LSR}} \leq 55 \text{ km s}^{-1}$; the limits of this integration were based on the line profiles provided by Castro-Carrizo et al. (2010) and my own preliminary assessments of the CARMA data. Figure 56 demonstrates that seven of the twelve observed lines (SiO, HCN, CS, SO, ^{13}CO , CN, and ^{12}CO) are clearly detected.

Figure 57 shows the line profiles for each observed window. The lines are the result of summing

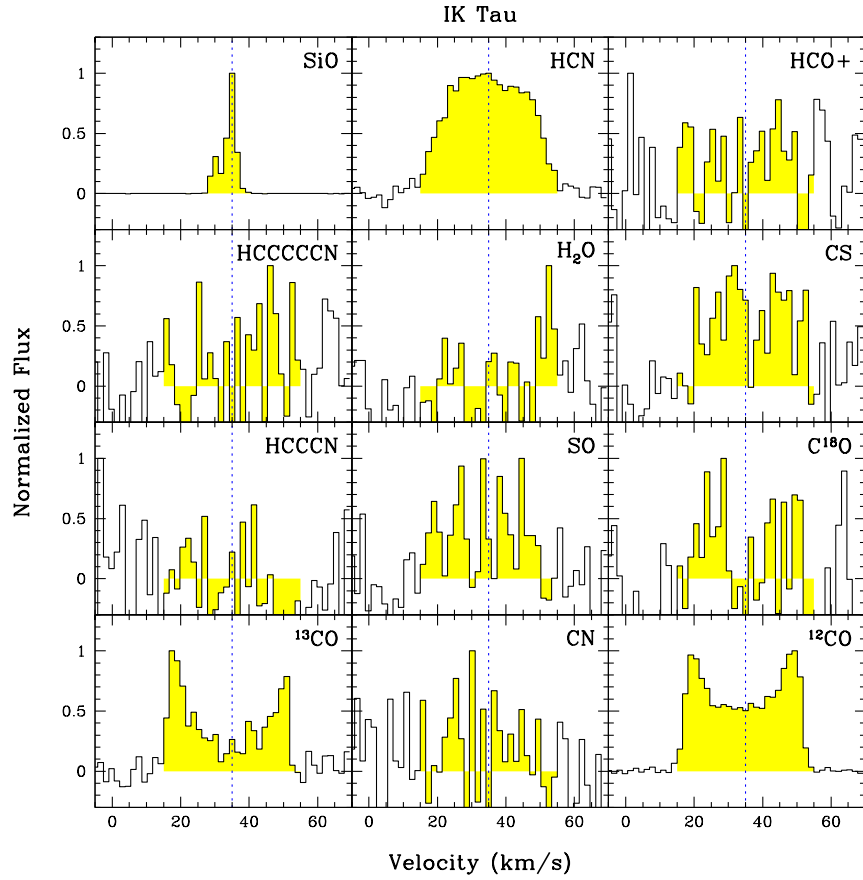


Fig. 57.— Line profiles for the twelve targeted lines of IK Tau produced by summing all flux within a $20''$ aperture surrounding the star. All lines have been normalized to the peak flux within the velocity window. Spectral regions summed to produce the maps in Figure 56 are highlighted in yellow.

all flux within a $20''$ aperture centered on the star. So as to give an impression of the relative line widths, I have normalized all line profiles to the peak flux within the window. For reference, the SiO line is two orders of magnitude more luminous than the ^{12}CO line, which is the second strongest line observed. Figure 57 reinforces the impression from Figure 56, demonstrating that seven of the twelve observed lines have been detected with high signal-to-noise. Interestingly, even if at low significance, Figure 57 shows some signs of an H_2O line at $V_{\text{LSR}} \sim 52 \text{ km s}^{-1}$. If associated with IK Tau, the H_2O emission must be spatially located near the fastest moving portions of the wind. Given that winds are expected to accelerate as they get farther from the star and that the emission is asymmetric, this may mean that H_2O is being formed at the largest distances from the star probed by the wind on the far side of the star relative to our line of sight. More observations would be needed to confirm this detection of H_2O .

16.3. Wind Velocity

A detailed chemical analysis of the many lines detected in the CSE of IK Tau is beyond the scope of this contribution, and indeed beyond the skill set of this author. However, I have performed a rough kinematic analysis to estimate the expansion velocity of the wind as follows.

Given the different environments present within the CSE, one might expect the variety of lines observed to probe different regions. If there is, e.g., a strong velocity gradient from small to large radii, these different chemical probes could provide a measurement of this velocity structure by considering the spatial and spectral width of each line. Therefore, I have produced growth curves for each line (not shown) in terms of both area on the sky and as a function of V_{LSR} . In the spatial dimensions, I produce the growth curves by performing aperture photometry on the images in Figure 56 with apertures of increasing size from 1 – 15 times the synthesized beam size (approximately $4'' - 60''$) with the proper ellipticity and orientation. In the spectral dimension, the growth curves are produced by integrating the line profiles in Figure 57 folded about $V_{\text{LSR}} = 35 \text{ km s}^{-1}$.

Ideally, the growth curves should asymptote to a constant flux as no more flux is added at large distances and velocity offsets from the stars location. In practice, however, the accuracy of the growth curves is limited by the handling of flux present in the images that is unassociated with the source. In an attempt to minimize these effects, I subtract the mean flux in a spatial region that should only contain background emission (or emission resulting from errors in the calibration). For the strong SiO, ^{12}CO , ^{13}CO , and HCN lines, the background structure is not a strong source of error for the assessment of the growth curves. However, measurements based on the growth curves for the CS, SO, and CN lines are more problematic.

Figure 58 gives the measurements of radius versus expansion velocity based on, respectively, the 90% growth of the spatial and spectral distributions of flux. For the well measured lines, the errors on these measurements should be $< 1''$ and $< 1 \text{ km s}^{-1}$; errors on the CS, CN, and SO lines will

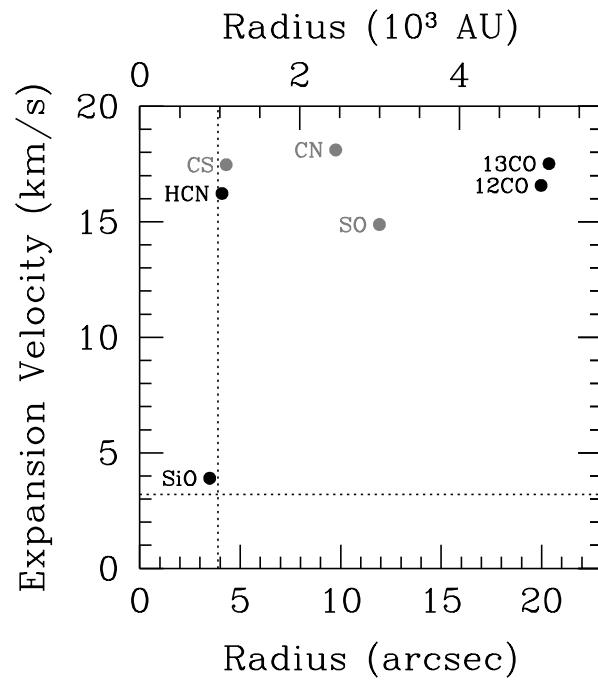


Fig. 58.— Measurements of the extent and maximum expansion velocity of the observed lines. The dotted lines give the approximate resolution limits of the data. The observed lines plotted in gray will have significant error, particularly in the calculation of the spatial extent.

be much larger. We note that the SiO flux is from the maser, not from SiO-emitting gas that follows the general expansion of the wind; Figure 58 shows that the SiO measurements are near the resolution limit of the observations. Based on these data, it is difficult to say if the wind of IK Tau accelerates beyond 10^3 AU; that is, the expansion velocity seems rather similar for all tracers regardless of their spatial extent. Not surprisingly, these data suggest that the primary acceleration of the wind occurs much closer to the stellar photosphere. Sub-arcsecond resolution would be required to probe regions below 100 AU, which might be more relevant to investigating the acceleration of the wind; such observations may be possible with ALMA.

16.4. Conclusions

AGB stars are interesting objects for study with millimeter interferometers like CARMA. Chemical and dynamical studies of their CSEs not only lead to a deeper understanding of intermediate-mass stellar evolution but also to the evolution of galaxies. AGB stars can produce substantial chemical yields into the local interstellar medium and, for an albeit brief period, be among the brightest objects in the galaxy at near-infrared wavelengths. These periods of intense emission can have significant implications for estimating the stellar mass of intermediate-age populations, which is particularly relevant to intermediate- and high-redshift objects where dynamical mass measurements are currently impractical.

In this study, I have used CARMA to observe the M-type Mira variable IK Tau. In twelve spectral windows, I observed SiO, HCN, HCO+, HCCCCCN, H₂O, CS, HCCCN, SO, C¹⁸O, ¹³CO, CN, and ¹²CO. Seven of these twelve lines were detected and used to assess the wind velocity of the CSE. The average expansion velocity traced by each line is ~ 17 km s⁻¹; however, I was unable to find any convincing evidence of a change in the wind velocity with radius. A detailed chemical analysis of the emission lines may provide insights into the composition of the CSE and its host star; however, such an analysis was not performed. Further observations with ALMA would be better suited to probing regions much closer to the stellar photosphere, which may be more relevant to investigating the wind generation mechanism(s).

E-mail addresses

Carmen Rodriguez Gonzalvez, California Institute of Technology, carmenrg@ipac.caltech.edu
Erin Grand, University of Maryland, eringrand@gmail.com
Che-Yu Chen, University of Maryland, cychen@astro.umd.edu
Dyas Utomo, UC Berkeley, dyas@berkeley.edu
Mai Truong, UC Berkeley, mai.truong@berkeley.edu
Isaac Shivvers, UC Berkeley, ishivvers@berkeley.edu
Dominique Segura-Cox, University of Illinois, segurac2@illinois.edu
Yiran Wang, University of Illinois, wang60@illinois.edu
Ashley Lindley, University of Alabama in Huntsville, campbea1@uah.edu
Aaron Juarez, Vanderbilt-Fisk, ajuarez88@gmail.com
Xing Lu (Walker), Smithsonian Astrophysical Observatory, xlu@cfa.harvard.edu
Chihomi Hara, Tokyo University, c.hara@nao.ac.jp
Maria Jose Maureira, Yale University, mm2445@pantheon.yale.edu
Matthew Rickert, Northwestern University, matthewrickert2017@u.northwestern.edu
Kyle Westfall, Kapteyn Astronomical Institute, Groningen, the Netherlands, westfall@astro.rug.nl
Jorge Gonzalez, Pontificia Universidad Catolica de Chile, jgonzal@astro.puc.cl
Pedro Salas, Pontificia Universidad Catolica de Chile, pnsalas@uc.cl

REFERENCES

- Aladro, R., Viti, S., Riquelme, D., Martin, S., Mauersberger, R., Martin-Pintado, J., & Bayet, E. 2012, ArXiv e-prints
- Alatalo, K. e. a. 2012, MNRAS
- Arce, H. G., & Sargent, A. I. 2006, ApJ, 646, 1070
- Baldry, I. K., & et al. 2004, ApJ, 600
- Beuther, H., Schilke, P., Menten, K. M., Motte, F., Sridharan, T. K., & Wyrowski, F. 2002, ApJ, 566, 945
- . 2005, ApJ, 633, 535
- Bower, R. G., Lucey, J. J., & Ellis, R. S. 1991, MNRAS, 254
- Brooke, T. Y., et al. 2007, ApJ, 655, 364
- Castro-Carrizo, A., et al. 2010, A&A, 523, A59

- Cecil, G., Dopita, M. A., Groves, B., Wilson, A. S., Ferruit, P., Pécontal, E., & Binette, L. 2002, *ApJ*, 568, 627
- Chen, H., Myers, P. C., Ladd, E. F., & Wood, D. O. S. 1995, *ApJ*, 445, 377
- Chiang, H.-F., Looney, L. W., Tobin, J. J., & Hartmann, L. 2010, *ApJ*, 709, 470
- Combes, F., Young, L. M., & Bureau, M. 2007, *MNRAS*, 377
- Conroy, C., Gunn, J. E., & White, M. 2009, *ApJ*, 699, 486
- Deguchi, S., Nakashima, J.-I., & Takano, S. 2004, *PASJ*, 56, 1083
- García-Burillo, S., et al. 2010, *A&A*, 519, A2
- González Delgado, D., Olofsson, H., Kerschbaum, F., Schöier, F. L., Lindqvist, M., & Groenewegen, M. A. T. 2003, *A&A*, 411, 123
- Hawarden, T. G. e. a. 1981, *MNRAS*, 196
- Helfer, T. T., & Blitz, L. 1995, *ApJ*, 450, 90
- Helfer, T. T., Thornley, M. D., Regan, M. W., Wong, T., Sheth, K., Vogel, S. N., Blitz, L., & Bock, D. C. 2003, *ApJS*, 145, 259
- Höfner, S. 2008, *A&A*, 491, L1
- Jura, M. 1986, *ApJ*, 306
- Knapp, G. R., Guhathukarta, P., Kim, D.-W., & Jura, M. 1989, *ApJS*, 70
- Knapp, G. R., Turner, E. L., & Cunniffe, P. E. 1985, *AJ*, 90
- Lees, J. F., Knapp, G. R., Rupen, M. P., & Phillips, T. G. 1991, *ApJ*, 379
- Lefloch, B., et al. 2010, *A&A*, 518, L113
- Lombardi, M., Alves, J., & Lada, C. J. 2006, *A&A*, 454, 781
- Looney, L. W., Tobin, J. J., & Kwon, W. 2007, *ApJL*, 670, L131
- Maraston, C. 2005, *MNRAS*, 362, 799
- Nakashima, J.-i., & Deguchi, S. 2000, *PASJ*, 52, L43
- . 2005, *ApJ*, 633, 282
- Nowak, N., Thomas, J., Erwin, P., Saglia, R. P., Bender, R., & Davies, R. I. 2010, *MNRAS*, 403, 646

- Oosterloo, T. e. a. 2010, MNRAS, 409
- Paturel, G., Theureau, G., Bottinelli, L., Gouguenheim, L., Coudreau-Durand, N., Hallet, N., & Petit, C. 2003, A&A, 412, 57
- Ramstedt, S., Schöier, F. L., Olofsson, H., & Lundgren, A. A. 2008, A&A, 487, 645
- Rand, R. J., & Wallin, J. F. 2004, ApJ, 614, 142
- Sage, L. J., & Welch, G. A. 2006, ApJ, 644
- Sage, L. J., & Wrobel, J. M. 1989, ApJ, 344
- Skokos, C., Patsis, P. A., & Athanassoula, E. 2002, MNRAS, 333, 847
- Smith, R. J., Shetty, R., Stutz, A. M., & Klessen, R. S. 2012, ApJ, 750, 64
- Sridharan, T. K., Beuther, H., Schilke, P., Menten, K. M., & Wyrowski, F. 2002, ApJ, 566, 931
- Tobin, J. J., Hartmann, L., Calvet, N., & D’Alessio, P. 2008, ApJ, 679, 1364
- Tobin, J. J., Hartmann, L., & Loinard, L. 2010, ApJL, 722, L12
- Tobin, J. J., et al. 2011, ApJ, 740, 45
- Visvanathan, N., & Sandage, A. 1977, ApJ, 216
- Wang, J., Zhang, Z., & Shi, Y. 2011, MNRAS, 416, L21
- Welch, G. A., & Sage, L. J. 2003, ApJ, 584
- Zibetti, S., Gallazzi, A., Charlot, S., Pierini, D., & Pasquali, A. 2012, ArXiv e-prints